

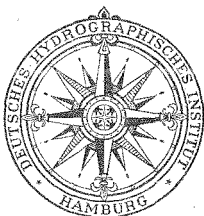
Measurements of Wind-Wave  
Growth and Swell Decay during  
the Joint North Sea Wave Project  
(JONSWAP)

UDC 551.466.31; ANE German Bight

By

K. Hasselmann, T. P. Barnett, E. Bouws, H. Carlson,  
D. E. Cartwright, K. Enke, J. A. Ewing, H. Gienapp,  
D. E. Hasselmann, P. Kruseman, A. Meerburg, P. Müller,  
D. J. Olbers, K. Richter, W. Sell, H. Walden

Ergänzungsheft zur Deutschen Hydrographischen Zeitschrift  
Reihe A (80), Nr. 12



1973

DEUTSCHES HYDROGRAPHISCHES INSTITUT · HAMBURG

**Ergänzungsheft**  
**zur**  
**Deutschen Hydrographischen Zeitschrift**

Herausgegeben vom Deutschen Hydrographischen Institut

Reihe A (8<sup>o</sup>), Nr. 12

**Measurements of Wind-Wave Growth and Swell Decay  
during the Joint North Sea Wave Project (JONSWAP)**

UDC 551.466.31; ANE German Bight

By  
**K. Hasselmann et al.**



1973

# Measurements of Wind-Wave Growth and Swell Decay during the Joint North Sea Wave Project (JONSWAP)

UDC 551.466.31; ANE German Bight

By

K. Hasselmann, T. P. Barnett, E. Bouws, H. Carlson,  
D. E. Cartwright, K. Enke, J. A. Ewing, H. Gienapp,  
D. E. Hasselmann, P. Kruseman, A. Meerburg, P. Müller,  
D. J. Olbers, K. Richter, W. Sell, H. Walden



1973

### Anschriften der Verfasser

- K. Hasselmann, Institut für Geophysik, Hamburg, Germany; 1970-72 also Doherty Professor at Woods Hole Oceanographic Institution, Woods Hole, Mass., U.S.A.
- T. P. Barnett, Westinghouse Ocean Research Laboratory, San Diego, Calif., U.S.A.; now at Scripps Institution of Oceanography, La Jolla, Calif., U.S.A.
- E. Bouws, Koninklijk Nederlands Meteorologisch Instituut, De Bilt, The Netherlands
- H. Carlson, Deutsches Hydrographisches Institut, Hamburg, Germany
- D. E. Cartwright, National Institute of Oceanography, Wormley, Great Britain
- K. Enke, Institut für Geophysik, Hamburg, Germany
- J. A. Ewing, National Institute of Oceanography, Wormley, Great Britain
- H. Gienapp, Deutsches Hydrographisches Institut, Hamburg, Germany
- D. E. Hasselmann, Institut für Geophysik, Hamburg, Germany
- P. Kruseman, Koninklijk Nederlands Meteorologisch Instituut, De Bilt, The Netherlands
- A. Meerburg, Koninklijk Nederlands Meteorologisch Instituut, De Bilt, The Netherlands; now at Dutch Ministry of Foreign Affairs, The Netherlands
- P. Müller, Institut für Geophysik, Hamburg, Germany
- D. J. Olbers, Institut für Geophysik, Hamburg, Germany
- K. Richter, Deutsches Hydrographisches Institut, Hamburg, Germany
- W. Sell, Institut für Geophysik, Hamburg, Germany
- H. Walden, Deutsches Hydrographisches Institut, Hamburg, Germany

© Deutsches Hydrographisches Institut, Hamburg · 1973

Schriftleitung: Dr. Helmut Mädler, 205 Hamburg 80, Sichter 4

und Walter Horn, 2 Hamburg 6, Felix-Dahn-Straße 2

Druck: J. J. Augustin, Glückstadt/Elbe



## CONTENTS

Summary - Zusammenfassung - Résumé . . . . .	7
<b>Part 1. The experiment . . . . .</b>	<b>10</b>
1.1. Introduction . . . . .	10
1.2. The wave profile . . . . .	15
1.3. Other field measurements . . . . .	16
1.4. Intercomparison of frequency wave spectra . . . . .	19
1.5. Directional measurements . . . . .	19
1.6. Cases studied . . . . .	22
1.7. Logistics . . . . .	25
Acknowledgments . . . . .	26
<b>Part 2. Wave growth . . . . .</b>	<b>27</b>
2.1. Generation cases . . . . .	27
2.2. Kitaigorodskii's similarity law . . . . .	28
2.3. Wind stress and turbulence measurements . . . . .	28
2.4. Fetch dependence of one-dimensional spectra . . . . .	32
2.5. The directional distribution. . . . .	38
2.6. The mean source function . . . . .	39
2.7. Analysis of individual generation cases . . . . .	42
2.8. Origin of the spectral peak . . . . .	48
2.9. The energy and momentum balance of the spectrum . . . . .	49
2.10. Variability of the spectrum . . . . .	52
2.11. Conclusions . . . . .	57
<b>Part 3. Swell Attenuation . . . . .</b>	<b>71</b>
3.1. Conservation of action and energy flux . . . . .	71
3.2. Attenuation due to bottom friction . . . . .	73
3.3. Energy flux analysis of swell data . . . . .	74
3.4. Lateral variations of bottom topography . . . . .	81
3.5. Dispersion characteristics. . . . .	87
3.6. Conclusions . . . . .	89
Appendix: Statistical analysis of the attenuation parameter $\Gamma$ . . . . .	90
<b>Notation. . . . .</b>	<b>92</b>
<b>References . . . . .</b>	<b>94</b>

**Summary:** Wave spectra were measured along a profile extending 160 kilometers into the North Sea westward from Sylt for a period of ten weeks in 1968 and 1969. During the main experiment in July 1969, thirteen wave stations were in operation, of which six stations continued measurements into the first two weeks of August. A smaller pilot experiment was carried out in September 1968. Currents, tides, air-sea temperature differences and turbulence in the atmospheric boundary layer were also measured. The goal of the experiment (described in Part 1) was to determine the structure of the source function governing the energy balance of the wave spectrum, with particular emphasis on wave growth under stationary offshore wind conditions (Part 2) and the attenuation of swell in water of finite depth (Part 3).

The source functions of wave spectra generated by offshore winds exhibit a characteristic plus-minus signature associated with the shift of the sharp spectral peak towards lower frequencies. The two-lobed distribution of the source function can be explained quantitatively by the nonlinear transfer due to resonant wave-wave interactions (second order Bragg scattering). The evolution of a pronounced peak and its shift towards lower frequencies can also be understood as a self-stabilizing feature of this process. For small fetches, the principal energy balance is between the input by wind in the central region of the spectrum and the nonlinear transfer of energy away from this region to short waves, where it is dissipated, and to longer waves. Most of the wave growth on the forward face of the spectrum can be attributed to the nonlinear transfer to longer waves. For short fetches, approximately  $(80 \pm 20)\%$  of the momentum transferred across the air-sea interface enters the wave field, in agreement with Dobson's direct measurements of the work done on the waves by surface pressures. About 80-90% of the wave-induced momentum flux passes into currents via the nonlinear transfer to short waves and subsequent dissipation; the rest remains in the wave field and is advected away. At larger fetches the interpretation of the energy balance becomes more ambiguous on account of the unknown dissipation in the low-frequency part of the spectrum. Zero dissipation in this frequency range yields a minimal atmospheric momentum flux into the wave field of the order of  $(20 \pm 20)_{-10}^{+20}\%$  of the total momentum transfer across the air-sea interface – but ratios up to 100% are conceivable if dissipation is important. In general, the ratios (as inferred from the nonlinear energy transfer) lie within these limits over a wide (five-decade) range of fetches encompassing both wave-tank and the present field data, suggesting that the scales of the spectrum continually adjust such that the wave-wave interactions just balance the energy input from the wind. This may explain, among other features, the observed decrease of Phillips' "constant" with fetch.

The decay rates determined for incoming swell varied considerably, but energy attenuation factors of two along the length of the profile were typical. This is in order of magnitude agreement with expected damping rates due to bottom friction. However, the strong tidal modulation predicted by theory for the case of a quadratic bottom friction law was not observed. Adverse winds did not affect the decay rate. Computations also rule out wave-wave interactions or dissipation due to turbulence outside the bottom boundary layer as effective mechanisms of swell attenuation. We conclude that either the generally accepted friction law needs to be significantly modified or that some other mechanism, such as scattering by bottom irregularities, is the cause of the attenuation.

The dispersion characteristics of the swells indicated rather nearby origins, for which the classical  $\delta$ -event model was generally inapplicable. A strong Doppler modulation by tidal currents was also observed.

**Messungen des Wind-Wellen-Wachstums und des Dünungszerfalls während des Joint North Sea Wave Project (JONSWAP) (Zusammenfassung).** Während einer Zeitspanne von insgesamt zehn Wochen in den Jahren 1968 und 1969 wurden längs eines Profils, das sich 160 km weit seewärts westlich Sylt in die Nordsee hinaus erstreckte, Seegangsspektren gemessen. Während des Haupt-experiments im Juli 1969 arbeiteten dreizehn Wellenmeßstationen, an sechs Stationen wurden die Messungen auch in den ersten zwei Augustwochen weitergeführt. Ein kleineres Vorexperiment wurde im September 1968 ausgeführt. Strömungen, Gezeiten, Wasser-Luft-Temperaturdifferenzen und Turbulenz in der atmosphärischen Grenzschicht wurden zusätzlich gemessen. Das Ziel des Experiments (beschrieben in Teil 1) war es, die Quellfunktion zu ermitteln, die die Energiebilanz des Seegangsspektrums bestimmt, wobei besonders das Wellenwachstum bei stationären ablandigen Winden (Teil 2) und die Dämpfung der Dünung bei endlicher Wassertiefe untersucht wurden (Teil 3).

Die Quellfunktion des von ablandigen Winden erzeugten Seegangsspektrums zeigt eine charakteristische Plus-Minus-Signatur, verbunden mit einer Verschiebung des scharfen spektralen Peaks zu niedrigeren Frequenzen. Diese zweiteilige Struktur der Quellfunktion kann quantitativ

durch nichtlineare Energieübergänge infolge resonanter Wellen-Wellen-Wechselwirkungen (Bragg-Streuung zweiter Ordnung) erklärt werden. Die Entwicklung eines betonten Peaks und seine Verschiebung zu niedrigeren Frequenzen kann auch als Selbststabilisierung dieses Prozesses verstanden werden. Für kurzen Fetch wird die Energiebilanz im wesentlichen ausgeglichen zwischen der Zufuhr durch den Wind im Hauptteil des Spektrums und dem nichtlinearen Transport von Energie aus diesem Bereich zu kürzeren Wellen, wo sie dissipiert wird, und zu längeren Wellen. Der Hauptanteil des Wellenwachstums an der Vorderflanke des Spektrums kann auf nichtlineare Übergänge zu längeren Wellen zurückgeführt werden. Für kurzen Fetch fließen  $(80 \pm 20)\%$  des Impulses, der an der Grenzfläche Luft-Wasser übertragen wird, in das Wellenfeld; das steht in Übereinstimmung mit Dobson's direkten Messungen der Arbeit, die vom Oberflächendruck an den Wellen geleistet wird. Ungefähr 80–90% des welleninduzierten Impulsflusses wird über nichtlinearen Transport zu kurzen Wellen und folgende Dissipation an die Strömung abgegeben, der Rest bleibt im Wellenfeld und wird von diesem fortgeführt. Bei längerem Fetch wird die Interpretation der Energiebilanz wegen der unbekannten Dissipation im niederfrequenten Teil des Spektrums ungewisser. Keine Dissipation in diesem Frequenzbereich liefert eine untere Grenze des atmosphärischen Impulsflusses in das Wellenfeld von etwa  $(20 \pm 20)\%$  des gesamten Impuls-

flusses durch die Grenzfläche Luft-Wasser – aber Werte bis 100% sind vorstellbar, wenn die Dissipation wesentlich ist. Im allgemeinen liegen die Werte (bestimmt aus den nichtlinearen Energieübergängen) innerhalb dieser Grenzen, und zwar für einen weiten Bereich (fünf Dekaden) des Fetch, wobei sowohl Daten aus Wellentanks als auch von den hier dargestellten Feldmessungen eingeschlossen sind. Dadurch wird nahegelegt, daß sich die Skalen des Spektrums kontinuierlich derart einstellen, daß die Wellen-Wellen-Wechselwirkungen gerade die Energiezufuhr durch den Wind ausgleichen. Dies kann unter anderem die beobachtete Abnahme der Phillipsschen „Konstante“ erklären.

Die Zerfallsraten, die für einlaufende Dünung bestimmt wurden, variierten beträchtlich, aber Energiedämpfungsfaktoren von 2 längs der gesamten Länge des Profils waren typisch. Dies stimmt größenordnungsmäßig überein mit Dämpfungsraten, wie sie infolge von Bodenreibung erwartet werden. Jedoch wurde die starke Gezeitenmodulation, die von der Theorie für ein quadratisches Bodenreibungsgesetz vorhergesagt wird, nicht beobachtet. Gegenwinde hatten keinen Einfluß auf die Zerfallsrate. Durch Berechnungen lassen sich auch Wellen-Wellen-Wechselwirkungen oder turbulente Dissipation außerhalb der Bodengrenzschicht als wirksame Mechanismen der Dünungsdämpfung ausschließen. Wir folgern daraus, daß entweder das allgemein akzeptierte Reibungsgesetz wesentlich geändert werden muß oder daß ein anderer Mechanismus, wie z.B. Streuung durch Bodenunregelmäßigkeiten, die Ursache der Dämpfung ist.

Die Dispersionscharakteristiken der Dünungen deuteten auf recht nahe gelegene Ursprungsgebiete hin, für die das klassische  $\delta$ -Ereignis-Modell im allgemeinen nicht anwendbar war. Eine starke Doppler-Modulation durch Gezeitenströme wurde beobachtet.

**Mesures de la croissance des vagues dues au vent et du comblement de la houle dans le Projet commun relatif aux vagues de la mer du Nord (Joint North Sea Wave Project – JONSWAP) (Résumé).** On a mesuré les spectres des vagues, le long d'une coupe s'étendant sur 160 kilomètres, dans la mer du Nord à l'Ouest de Sylt, pendant une période de dix semaines en 1968 et 1969. Au cours de l'expérience principale, en juillet 1969, treize stations d'observation des vagues furent mises en service, dont six continuèrent les mesures pendant les deux premières semaines d'août. On a fait une expérience pilote plus réduite en septembre 1968. On a également mesuré les courants, les marées, les différences de température entre l'air et la mer ainsi que la turbulence dans la couche atmosphérique voisine de la surface. Le but de l'expérience (indiqué dans la première partie) était de déterminer la structure de la fonction-origine déterminant l'équilibre de l'énergie du spectre de la vague, en insistant particulièrement sur la croissance de la vague quand le vent souffle de terre de façon constante (deuxième partie) et sur l'atténuation de la houle par fonds de profondeur limitée (troisième partie).

Les fonctions-origines du spectre de la vague soulevée par des vents de terre ont une allure plus ou moins caractéristique, en rapport avec le décalage du sommet escarpé du spectre vers les fréquences plus basses. La distribution de la fonction-origine selon deux lobes peut s'expliquer quantitativement par le transfert non linéaire du aux actions réciproques vague-vague, en résonance (Dispersion de Bragg du second ordre). L'évolution d'un sommet accentué et son décalage vers les fréquences plus basses peuvent aussi être interprétés comme une caractéristique de stabilisation de ce processus. Pour les petits déplacements, l'équilibre de l'énergie se réalise principalement entre celle qu'apporte le vent dans la région centrale du spectre et le transfert non linéaire d'énergie loin de cette région: – Vers les vagues courtes, où elle se dissipe, – et vers les vagues plus longues. La plus grande partie de la croissance de la vague, sur la face avant du spectre, peut être attribuée au transfert non linéaire vers les vagues plus longues. Pour les déplacements courts, environ  $(80 \pm 20)\%$  de la force vive transférée à travers l'interface air-mer entre dans le champ de la vague, d'après les mesures directes de Dobson, relatives au travail que les pressions extérieures effectuent sur les vagues. Environ 80 à 90% du flux de force crée par la vague passe dans les courants par la voie d'un transfert non linéaire dans les vagues courtes et d'une dissipation ultérieure, le reste demeure dans le champ de la vague et se trouve emporté au loin. Pour les déplacements plus

amples, l'interprétation de l'équilibre de l'énergie devient plus incertaine car on ne sait rien de la dissipation dans la région des basses fréquences du spectre. Une dissipation nulle dans cette gamme de fréquences donne un flux minimal de force vive atmosphérique dans le champ de la vague, de l'ordre de  $\left(20 \pm 20\right)\%$  du transfert total de force vive à travers l'interface air-mer, mais des rapports allant jusqu'à 100 % sont concevables si la dissipation est importante. En général, les rapports (découlant du transfert non linéaire d'énergie) restent en dedans de ces limites dans une large gamme (cinq décades) de déplacements cernant l'environnement de la vague et, aussi, les données présentes du champ. Cela laisse penser que les échelles du spectre s'ajustent d'une façon continue, de sorte que les actions réciproques des vagues équilibrent exactement l'énergie apportée par le vent. On peut expliquer ainsi, entre autre particularités, la décroissance observée de la «constante» de Phillips avec le déplacement.

Les taux de comblement déterminés pour la houle arrivant sur des fonds limités variaient énormément mais les facteurs d'atténuation des deux énergies sur la longueur de la coupe étaient caractéristiques. Leur ordre de grandeur correspond aux taux d'amortissement escomptés pour le frottement sur le fond. Toutefois, on n'a pas observé la forte modulation due à la marée, théoriquement prévue dans le cas d'une loi quadratique du frottement sur le fond. Les vents contraires n'ont pas affecté le taux de comblement. Les calculs éliminent aussi, comme mécanismes réels de l'atténuation de la houle: — Les actions réciproques vagues-vagues, — ou la déperdition due à la turbulence hors de la couche voisine du fond. Nous concluons, ou bien qu'il faut modifier profondément la loi généralement admise pour le frottement, ou que quelqu'autre mécanisme, telle la dispersion causée par les irrégularités du fond, est la cause de l'atténuation.

Les caractéristiques de dispersion des houles indiquent plutôt des origines voisines, pour lesquelles le modèle classique du cas  $\delta$  était généralement inapplicable. On a également observé une forte modulation Doppler due aux courants de marée.

## 1. The Experiment

### 1.1. Introduction

The last fifteen years have seen considerable progress in the theory of wind-generated ocean waves. These advances have been paralleled by the development of improved mathematical techniques and computer facilities for numerical wave forecasting. However, critical tests of theoretical concepts and numerical forecasting methods have been severely limited in the past by the lack of detailed field studies of wave growth and decay. Thus considerable effort has been devoted to the theoretical analysis of many of the processes which could affect the spectral energy balance of the wave field – the generation of waves by wind (by a variety of mechanisms), the nonlinear energy transfer due to resonant wave-wave interactions, the energy loss due to white capping, interactions between very short waves and longer waves, and the dissipation of waves in shallow water by bottom friction, to list some of the more important contributions – but only very few have been subjected to quantitative field tests. Even where field experiments have been specifically designed to study these questions, limitations in available instrumentation have often led to incomplete coverage of the wave field, thus handicapping the interpretation of the data. Consequently, present wave prediction methods have necessarily been based on rather subjective conjectures as to the form of the source function governing the fundamental energy balance equation.

The Joint North Sea Wave Project (JONSWAP) was conceived as a cooperative venture by a number of scientists in England, Holland, the United States and Germany to obtain wave spectral data of sufficient extent and density to determine the structure of the source function empirically. It was decided that an array of sensors operating quasi-continuously for a period of several weeks was the most straightforward method of obtaining adequate sampling density of the wave field with respect to frequency, propagation direction, space and time, under the desired wide variety of external geophysical conditions. The array that was eventually used consisted of thirteen wave stations spaced along a 160 km profile extending westward from the Island of Sylt (North Germany) into the North Sea. All instruments provided the usual frequency power spectra, while six of the stations (5 pitch-roll buoys and 1 six-element array) yielded directional information in addition. The complete profile was in operation for four weeks during July 1969; another six weeks of data were obtained from a smaller number of stations during the two weeks immediately following the main experiment and in a pilot experiment in September 1968.

The entire set of time series was spectral analyzed, but the interpretation of the data is restricted in the present papers to selected cases falling into either of two particularly simple categories: the evolution of the spectrum under stationary, offshore wind conditions (Part 2), and the attenuation of incoming swell (Part 3). Over 2000 wave spectra were measured; about 300 of these represented reasonably well-defined quasi-stationary generation cases, of which 121 corresponded to "ideal" stationary and homogeneous wind conditions; 654 spectra contained well-developed peaks suitable for the swell attenuation study.

### Wave Growth

The present wave generation study may be regarded as a natural extension of the pioneering work of R. L. Snyder and C. S. Cox [1966] and T. P. Barnett and J. C. Wilkerson [1967]. Both of these experiments utilized a single mobile wave station to determine the evolution of the wave spectrum in space and time.

Snyder and Cox measured the growth rate of a single frequency component (0.3 Hz) by towing an array of wave recorders downwind at the group velocity of the component. They found exponential growth in accordance with the linear instability mechanisms proposed by J. Jeffreys [1924] and J. W. Miles [1957], but at a rate almost an order of magnitude greater than predicted by either theory – or by the later instability theories which took more detailed account of the turbulent response characteristics of the atmospheric boundary layer (e.g. O. M. Phillips [1966], K. Hasselmann [1967, 1968], R. E. Davis [1969, 1970], R. Long [1971], D. E. Hasselmann [1971]). Moreover, assuming that the observed growth rates were due entirely to a linear input from the atmosphere, Snyder and Cox inferred a momentum transfer from the atmosphere to the wave field which was several times greater than the known total momentum loss from the atmosphere to the ocean. As shown below, it appears that this paradox can be largely resolved by taking account of the nonlinear wave interactions, which we found to be responsible for the major part of the observed wave growth on the forward face of the spectrum.

The evolution of the complete (one-dimensional) wavenumber spectrum under fetch-limited conditions was first measured by T. P. Barnett and J. C. Wilkerson [1967] using an airborne radar altimeter\*. Only two wave profiles were flown, but again exponential growth rates were found in general agreement with Snyder and Cox's results. In addition, the measurement of the complete spectrum revealed a significant overshoot effect; the energy at the peak of the spectrum was found to be consistently higher by factors between 1.2 and 2 than the asymptotic equilibrium level approached by the same frequency at large fetches. A similar effect was observed by A. J. Sutherland [1968] and by H. Mitsuyasu [1968a, 1969] in a wind-wave tank (see also T. P. Barnett and A. J. Sutherland [1968]). All authors speculated that the effect may be due to nonlinear processes. This interpretation found further support through H. Mitsuyasu's [1968b] wave tank measurements of the decay of a random wave field, which could be explained quite well by T. P. Barnett's [1968] parametrical estimates of the nonlinear energy transfer due to resonant wave interactions (K. Hasselmann [1962, 1963a, b]). (In their Pacific swell study, F. E. Snodgrass, G. W. Groves, K. F. Hasselmann et al. [1966] had similarly concluded that the decay of "new" swell close to a generation area was in accordance with this process.)

Useful information on wave growth can also be obtained indirectly from measurements at a single fixed location under different wind conditions. Using dimensional arguments, S. A. Kitaigorodskii [1962] has suggested that for a stationary, homogeneous wind field blowing orthogonally off a straight shore, the appropriately nondimensionalized wave spectrum should be a universal function of the nondimensional fetch  $\hat{x} = gx/u_*^2$  only, where  $x$  is the (dimensional) fetch,  $g$  is the acceleration of gravity and  $u_*$  is the friction velocity. Thus wave measurements obtained at a fixed location for different wind speeds can be translated into an equivalent dependence on fetch at a fixed wind speed.

H. Mitsuyasu [1968a, 1969], H. Mitsuyasu, R. Nakayama and T. Komori [1971], P. C. Liu [1971] and others have applied Kitaigorodskii's scaling law successfully to relate wave tank and field measurements and characterize the basic properties of fetch-limited spectra. The JONSWAP data is in general consistent with Kitaigorodskii's scaling hypothesis and confirms many of the spectral features summarized by these authors: pronounced overshoot factors, narrow peaks (considerably sharper than the fully-developed Pierson-Moskowitz [1964] spectrum), very steep forward faces (with associated rapid growth rates of wave components on the face), and an  $f^{-5}$  high frequency range with a fetch-dependent O. M. Phillips' [1958] "constant".

A principal conclusion of our wave growth study is that most of these properties can be explained quantitatively or qualitatively by the nonlinear energy transfer due to resonant wave-wave interactions (second order Bragg scattering). Thus the evolution of a sharp spectral

\* Similar experiments using a laser altimeter have been repeated recently by D. B. Ross, V. J. Cardone and J. W. Conaway [1970] and J. R. Schule, L. S. Simpson and P. S. DeLeonibus [1971].

peak is found to be a self-stabilizing feature of this process. The continual shift of the peak towards lower frequencies is also caused by the nonlinear energy transfer, and explains the large growth rates observed for waves on the forward face of the spectrum.

For small fetches, the energy balance in the main part of the spectrum is governed by the energy input from the atmosphere, the nonlinear transfer to lower and higher frequencies, and advection, dissipative processes apparently playing only a minor role. This balance determines the energy level of the spectrum, i.e. the value of Phillips' constant, and the rate at which the peak shifts towards lower frequencies. Assuming a friction coefficient  $c_{10}$  of the order of  $1.0 \times 10^{-3}$ , this picture implies that nearly all of the momentum lost from the atmosphere must be entering the wave field – in agreement with F. W. Dobson's [1971] correlation measurements of wave height and surface pressure. About 10% of the momentum flux from the atmosphere to the wave field is transferred to lower-frequency waves, where it is advected away. The rest is transferred to short waves, where it is converted to current momentum by dissipative processes.

With increasing fetch, the wave-wave momentum transfer to high wavenumbers decreases, representing only 13% of the total momentum flux across the air-sea interface in the limit of a fully-developed Pierson-Moskowitz spectrum. The net momentum flux  $\tau_w$  from the atmosphere to the wave field at large fetches depends on the unknown dissipation in the main part of the spectrum. Zero dissipation in this range implies a lower limit for  $\tau_w$  of about 20% of the total air-sea momentum flux – but this value could also lie closer to 100%, as in the small-fetch case, if dissipation is an important factor in the energy balance of the principal wind-sea components.

Although the present study has helped to clarify the general structure of the energy balance of fetch-limited wave spectra, a number of questions remain. The mechanism by which energy and momentum is transferred from the wind to the waves could not be investigated. Measurements with hot-wire instruments, wind vanes and cup anemometers yielded atmospheric turbulence spectra and the net momentum flux from the atmosphere to the ocean, but the instruments were too far above the surface to resolve the interactions between the atmospheric boundary layer and the wave field. A second open problem concerns the dissipative processes balancing the nonlinear energy flux to short waves. This question is of considerable interest not only with regard to the wind-wave energy balance, but also for the application of microwave techniques to the measurement of sea state from satellites (cf. K. Hasselmann [1972]). Finally, the transition from fetch-limited spectra to a fully developed equilibrium spectrum poses a number of questions which could not be investigated within the finite range of fetches available in this study.

## Swell Attenuation

For the generation studies, the water depth along the entire profile was sufficiently deep to be regarded effectively as infinite. However, much longer incoming swell components normally "felt bottom" along most of the profile, thus affording a good opportunity to investigate the effects of bottom topography on swell propagation.

It is well known that bottom effects play a significant role in the energy balance of waves in relatively shoal areas such as the North Sea or other parts of the continental margins. Most investigators have attributed the observed modifications in the form of the fully developed spectrum (e.g. J. Darbyshire [1963]) and the enhanced damping of the swell to bottom friction. Assuming a quadratic friction law, C. L. Bretschneider and R. O. Reid [1954] estimate a friction coefficient  $c_b$  of the order  $10^{-2}$ . Similar values were found by K. Hasselmann and J. I. Collins [1968], who applied a more detailed spectral formulation of the bottom friction theory to hurricane swell data in the Gulf of Mexico. The considerably larger decay rates found by H. Walden and H. J. Rubach [1967] in the North Sea are also consistent with the Hasselmann and Collins theory if the tidal currents are taken into account.

However, the extensive swell data available through this experiment, while in order of magnitude agreement with previous observations of swell attenuation rates, contradict a

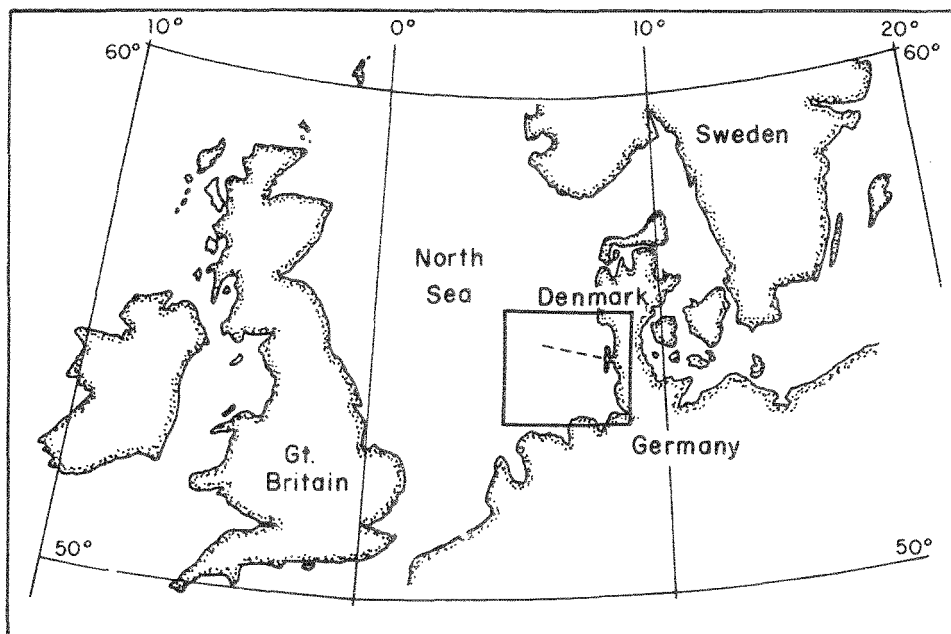


Fig. 1.1. Site of the wave experiment. The area in the square is shown enlarged in Fig. 1.2

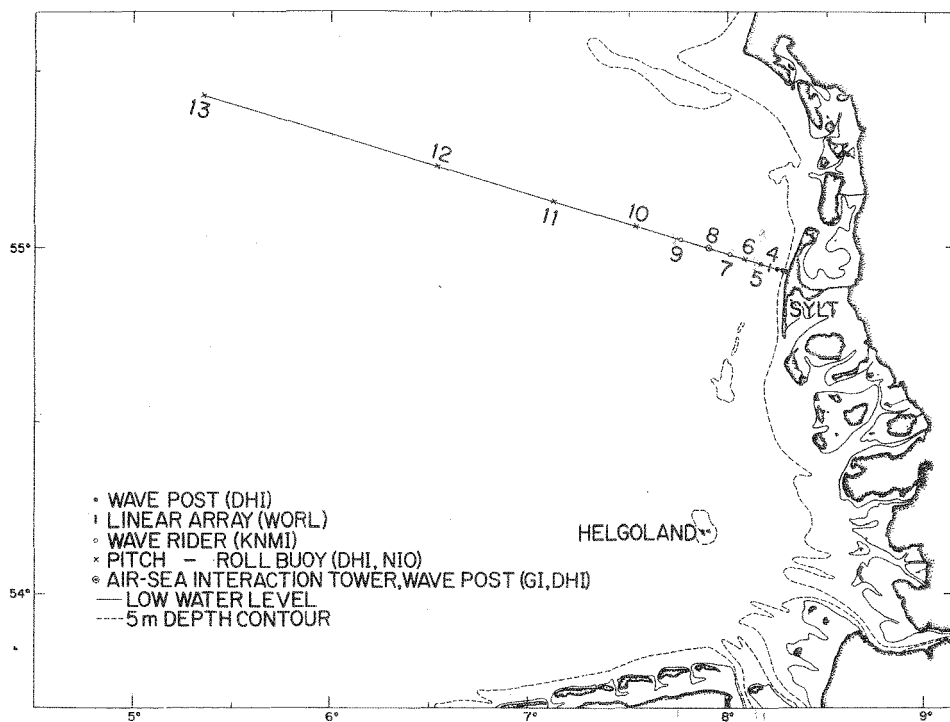


Fig. 1.2. The wave profile off Sylt



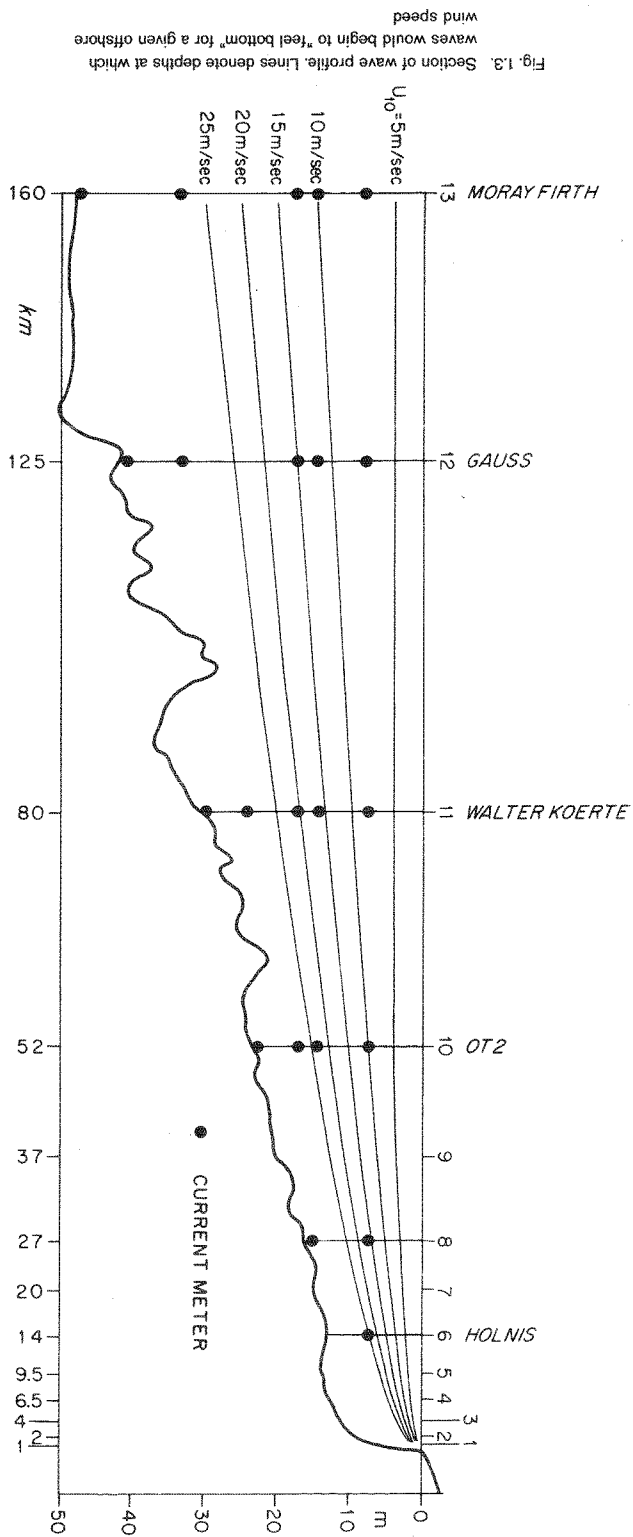


Fig. 1.3. Section of wave profile. Lines denote depths at which waves would begin to "feel bottom" for a given offshore wind speed

significant prediction of the theory. A quadratic (or any nonlinear) friction law should lead to a strong modulation of the swell decay rates by tidal currents. Experimentally, no such variation is found.

We suggest two possible explanations – neither of which we have been able to test in the present experiment. It is conceivable that the quadratic friction law, although shown to be an acceptable first-order approximation for sinusoidal waves in a wave tank (J. A. Putnam and J. W. Johnson [1949], R. P. Savage [1953], K. Kajiura [1964], Y. Iwagaki, Y. Tsuchiya and M. Sakai [1965], I. G. Jonsson [1965]), is not valid for the time-dependent boundary layer generated by the superposition of a random wave field on a tidal current in the real ocean. An objection to this explanation is that a complete independence of the swell attenuation on the tidal currents implies a linear friction law, which seems improbable for a turbulent boundary layer.

Alternatively, the observed swell decay may be due to processes other than bottom friction. Estimates of the damping due to interactions with turbulence distributed throughout the water column (K. Hasselmann [1968]) indicate that this process is too small by several orders of magnitude. A more promising possibility is the backscattering caused by irregularities of the bottom topography at scales comparable with the wavelength of the swell. Recent computations by R. Long [1972] show that this interaction could account for the observed attenuation rates assuming r.m.s. bottom irregularities in the appropriate wavelength range of the order of 20 cm. Experimentally, this process should be identifiable by the presence of offshore-propagating swell components whose energy increases with distance from shore (in contrast to the decreasing energy of swell which may be reflected from the shore). Unfortunately, the directional resolution in the present experiment was insufficient to resolve secondary swell components propagating in a direction opposite to the main swell.

## 1.2. The Wave Profile

The site of the wave study and the 160 km long measuring profile are shown in Figures 1.1 and 1.2. The area was chosen on account of its relatively smooth bottom topography, moderate tidal currents and convenient logistics.

The main experiment ran from July 1 until July 31, 1969, but measurements continued from August 1 to August 15, 1969 along a reduced profile (Stations 1–5 and 8). During these six weeks, 30-minute wave recordings were obtained continuously at 2 or 4 hourly intervals. Further measurements were also made along a 10-station profile during a pilot experiment from September 1 to September 30, 1968. In this earlier experiment measurements were limited to “interesting” cases of wave generation or incoming swell, and the times of recording at different stations were staggered to allow for the propagation time of the expected principal wave components. This mode of operation proved to be too demanding on the reliability of weather forecasts and communications, so that in the main experiment the following year a more rigid, predetermined schedule of recordings was introduced, in which the only on-spot decisions involved changes from standard four-hourly recording to two-hourly measurements during east-wind generation conditions.

The depth distribution along the profile lay in a convenient range enabling the study of both the generation of waves during offshore winds and the attenuation of long swells running inshore. For short, fetch-limited waves generated by local east winds, the depth could be regarded as essentially infinite along most of the profile, cf. Figure 1.3. The curves indicate the depth  $H = \frac{\lambda_m}{4}$  at which the principal wind-sea components would begin to be influenced appreciably by the bottom; the wavelength  $\lambda_m = \frac{g}{2\pi f_m^2}$  for a given wind speed

and fetch was evaluated from the appropriate empirical fetch dependence of the frequency  $f_m$  of the spectral peak, Fig. 2.6. The bottom influence is seen to be negligible for all wind speeds relevant for this study (the maximum east winds occurring during the experiment were of the order of 15 meter per second). On the other hand, a typical swell component of

10 seconds period, corresponding to a deep water wavelength of about 150 m, is appreciably influenced by the bottom along the entire profile, so that bottom friction or bottom scattering effects should be easily observable.

A variety of wave instruments were used in the experiment (Fig. 1.2). At Stations 1, 2, 3, 5 and 8 (we refer here and in the following to the July 1969 profile) the wave motion was measured by a small float moving within a perforated pipe mounted on a post. At Station 4 a linear directional array of six wave recorders was installed at variable separations along a line orthogonal to the profile (cf. Section 1.5). The wave sensors consisted of subsurface pressure transducers mounted on posts, with the exception of a closely spaced pair of resistance wave staffs used to resolve the short wave components. Tethered "waverider" buoys, which converted measurements of vertical acceleration internally to wave height, were used at Stations 7, 9 and 10. All of these nearshore instruments were unattended and/or remotely controlled and generated FM output signals which were telemetered to a shore station at the base of the profile. This technique was not readily applicable to the more distant Stations 11-13 and Station 6, which lay within a shipping lane. These stations were occupied by pitch-roll buoys deployed from ships. The pitch-roll buoy measures the vertical acceleration and both components of wave slope, thus giving a directional resolution of the wave field roughly comparable to the array at Station 4 (cf. M. S. Longuet-Higgins, D. E. Cartwright and N. D. Smith [1963]).

All instruments had high-frequency cut-offs between 0.7 and 1 Hz, corresponding to wavelengths between 3 and 1.5 m. Digitizing rates were normally 2 per second, equivalent to 1 Hz Nyquist frequency.

For intercalibration purposes Station 10 was occupied during the first half of the 1969 experiment by two instruments, a waverider and a pitch-roll buoy. This also provided a redundancy safeguard, and was useful in occasionally freeing the ship at station 10 to assist in servicing the unattended stations. In the second half of the experiment the pitch-roll buoy of Station 10 was moved to Station 7 and the waverider of that station was switched to Station 5 for comparison with the wave float instrument. In addition, a number of inter-comparison runs between various combinations of instruments were made during the 1968 experiment. A continual check on calibration consistency was furthermore provided by the intermeshed distribution of different types of instruments along the profile (cf. Section 1.4).

### 1.3. Other Field Measurements

To define the environmental parameters relevant for the energy balance of the wave field, winds, atmospheric momentum fluxes, currents, tidal heights and air-sea temperatures were monitored at various stations along the profile.

Wind speeds and directions and tidal heights were recorded continuously at Stations 2 and 8. Winds were also measured concurrently with air-sea temperatures every two hours on the ships.

At Station 8, atmospheric turbulence was measured at two levels, 5 and 8 m above mean sea level. The system at each level consisted of a combination of standard hot-wire instruments, together with cup anemometers and vanes intended for calibration purposes (K. Enke [1973]). All turbulence data were telemetered to shore together with the concurrently taken wave data (cf. Section 2.3).

Continuous current recordings were made throughout the 1968 and 1969 experiments at a number of depths and stations (Fig. 1.3). Emphasis on current measurements was based on the theoretical anticipation (K. Hasselmann and J. I. Collins [1968]) that currents near the bottom would have a strong influence on the attenuation of long swell by bottom friction. It was also conceivable that vertical current shear would influence wave generation. However, no detectable current influence was found in either the generation or the swell attenuation study. Since in most cases the observed currents did not deviate appreciably from the tabulated tidal currents (particularly the near-bottom currents) it proved adequate

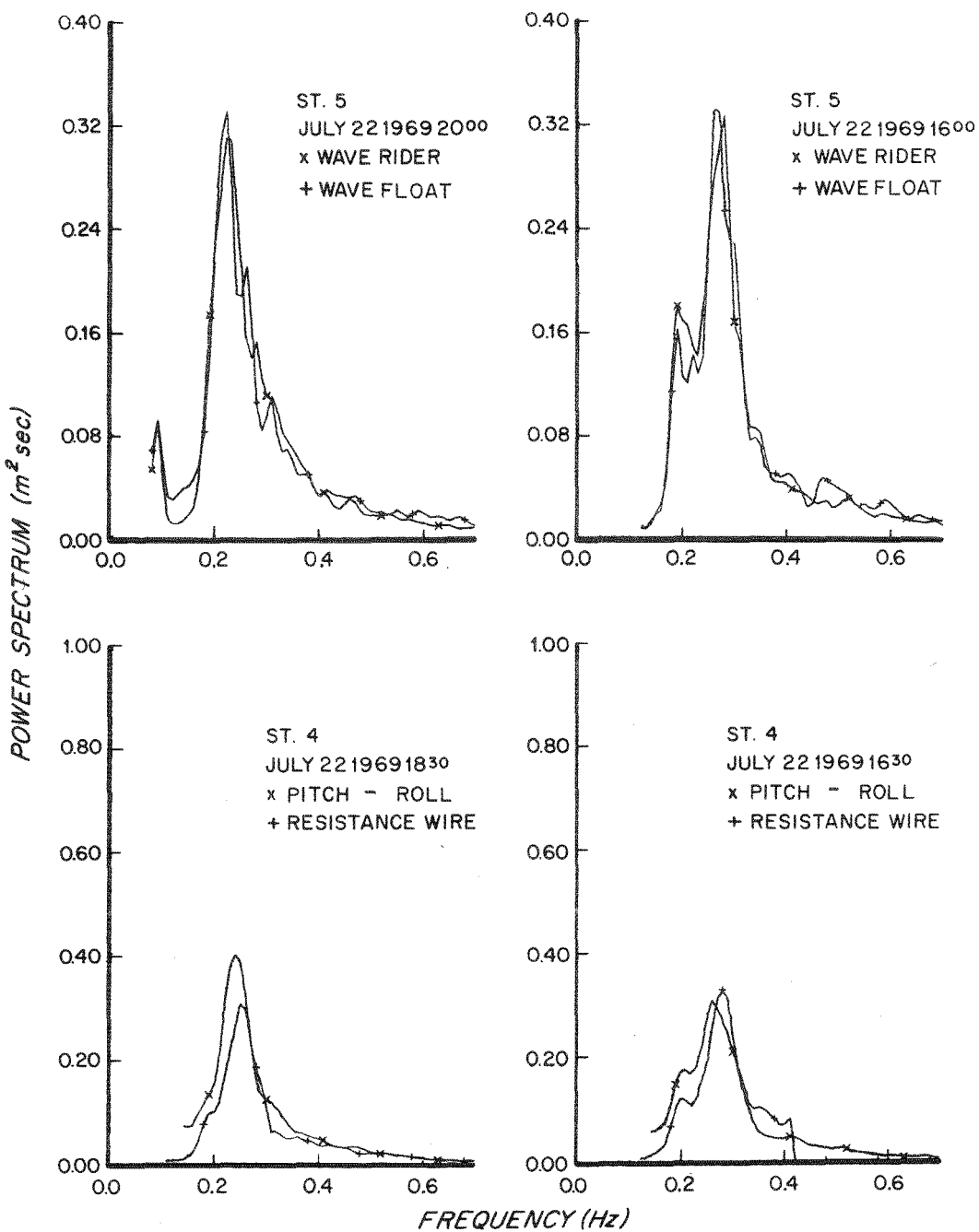


Fig. 1.4 a-d. Intercomparison measurements of frequency wave spectra

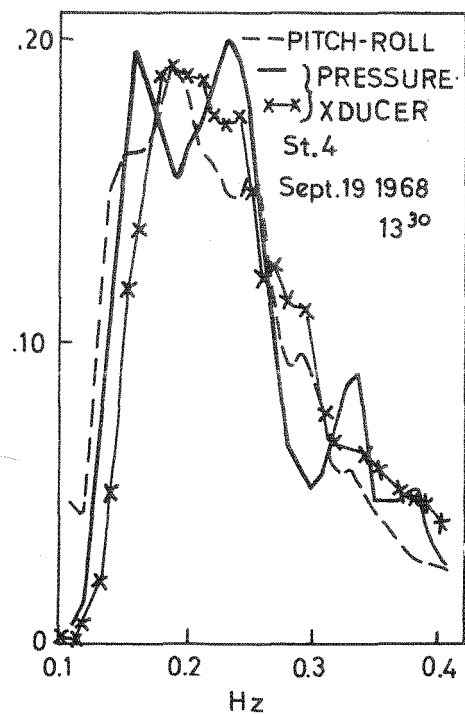
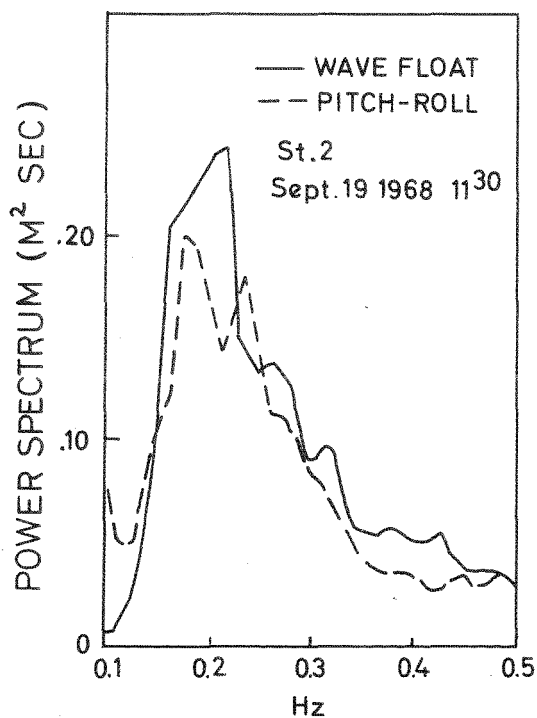
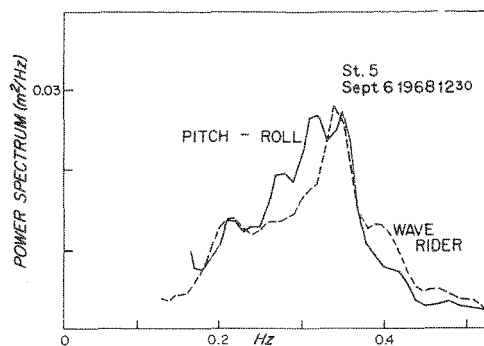
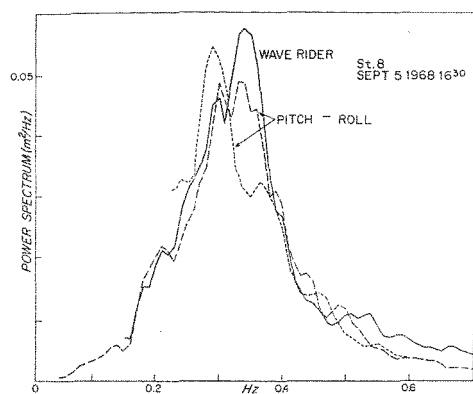


Fig. 1.4 e-h. Same as Fig. 1.4 a-d

for the negative outcome of the correlation analysis described in Parts 2 and 3 to work with the tabulated rather than the observed currents.

Independent of the wave project, however, the measurement of currents was also motivated by interest in the baroclinic response of the sea to a variable wind field. For this purpose a continuous hydro-station program was carried through from the ships at the outermost stations 11, 12, and 13. This work will be reported elsewhere (G. Becker, K. P. Koltermann, G. Prahm et al. [in prep.]).

#### 1.4. Intercomparison of Frequency Wave Spectra

The choice of a variety of wave measuring techniques was necessitated by the limitations of VHF and UHF telemetry ranges, the depths at which wave posts could be economically installed, and in part by the prior experience of participating groups. A prime concern of the experiment was therefore to establish the compatibility of the different techniques used. Figs. 1.4a–h show a series of one-dimensional frequency spectra measured at the same location and time by pairs of different instruments. In general, the agreement is excellent. Not all combinations of different instrument pairs were compared, but an independent continual check on the intercalibration consistency of all instruments was provided by the dovetailed distribution of different instrument types along the profile: at least one instrument of each group was flanked at some point in the profile by instruments of another type. In all cases studied, the spectral distributions showed a smooth variation with station number, without discernible discontinuities at the instrument transition points (with the exception of one generation case on September 11, 1968, in which three of the runs indicated an – unresolved – systematic error in the pitch-roll buoy measurements at Station 6, which were then discarded).

Although contrary to standard experimental practice, the simultaneous use of a number of independent measurement techniques proved to be an asset in establishing a broad calibration base and providing continual calibration monitoring throughout the experiment. The restriction to a single type of instrument has advantages in linear problems involving the comparison of energy levels at the same frequency. In this case the common instrumental transfer function can be eliminated. However, in the present experiment the evolution of the wave spectrum was found to be strongly dependent on nonlinear processes for which the determination of absolute energy levels in different frequency bands was essential.

It appears that with very few exceptions the one-dimensional wave spectra measured by all instruments were accurate to within the attainable statistical resolution. In a few cases the records were contaminated by noise, most frequently due to radio interference in the telemetry links. The noise spectrum was generally white, and if sufficiently low was simply subtracted. For noise levels greater than 20 or 30 % of the total energy, the measurement was discarded. About 90 % of the data yielded useable spectra in this sense. In the case of the swell study (Part 3), the figure was somewhat reduced by the inherent low-frequency noise of the pitch-roll buoys, which sometimes masked low-energy swell peaks of long period.

#### 1.5. Directional Measurements

The directional distribution of the wave field was determined from the pitch-roll buoys (Stations 6, 10, 11, 12 and 13) and the linear array at Station 4. Both instruments yielded only a limited number of moments of the energy distribution  $F(f, \theta)$  with respect to propagation direction  $\theta$  for a fixed frequency  $f$ . The moments obtained from the two types of instrument differ, so that an intercomparison is, in general, possible only in terms of a given parametrical model of the angular distribution function.

The directional characteristics of the pitch-roll buoy (in its earliest instrumental form) are described by M. S. Longuet-Higgins et al. [1963] and by D. E. Cartwright and N. D. Smith [1964]. Essentially, the instrument records three channels, two components (1) and (2) of the wave slope, and the vertical acceleration (3). A fourth (compass) channel enables (1) and (2) to be re-oriented to geographical axes. The auto-spectrum of (3),  $C_{33}$ , is

easily translated into the total energy spectrum of vertical displacement,  $E(f)$ , and the autospectra of (1) and (2) combine to give a direct measure of total wavenumber  $k$ , through the relation

$$C_{11} + C_{22} = C_{33} \cdot k^2 (2\pi f)^{-4}.$$

Three of the cross-spectral elements  $C_{ij}$ ,  $Q_{ij}$ , have zero expectancy, while the remaining three, together with  $C_{11} - C_{22}$ , provide four explicit and independent angular moments of the directional spectrum, of the form

$$\int_{-\pi}^{+\pi} F(f, \theta) (k e^{i\theta})^n d\theta, \quad n = 1, 2.$$

For reasons given below we in fact found use only for moments of order  $n = 1$ , and these may be expressed as moments of the normalised angular distribution  $s(f, \theta)$ , where  $F(f, \theta) = s(f, \theta) E(f)$ , with  $\int_{-\pi}^{+\pi} s(f, \theta) d\theta = 1$ ; thus

$$\frac{\bar{k}_1}{k}, \frac{\bar{k}_2}{k} = \frac{Q_{13}, Q_{23}}{C_{33}^{1/2} (C_{11} + C_{22})^{1/2}},$$

where  $(k_1, k_2) = (k \cos \theta, k \sin \theta)$ , and  $\bar{k}_i = \int_{-\pi}^{+\pi} k_i s d\theta$ .

In the case of the linear array, the wave heights  $\zeta_i$  and  $\zeta_j$  measured at any two locations spaced at a distance  $r_{ij}$  normal to the profile yield directional moments

$$\left\{ \begin{matrix} C_{ij} \\ Q_{ij} \end{matrix} \right\} = \int_{-\pi}^{+\pi} F(f, \theta) \left\{ \begin{matrix} \cos \\ \sin \end{matrix} \right\} (kr_{ij} \sin \theta) d\theta$$

where the angle of wave propagation  $\theta$  is measured relative to the profile direction.

The array consisted of a superposition of two 4-element arrays differing by a factor of 4 in scale (Fig. 1.5). The coordinates of each 4-element array were chosen as  $x_j = 0, D,$

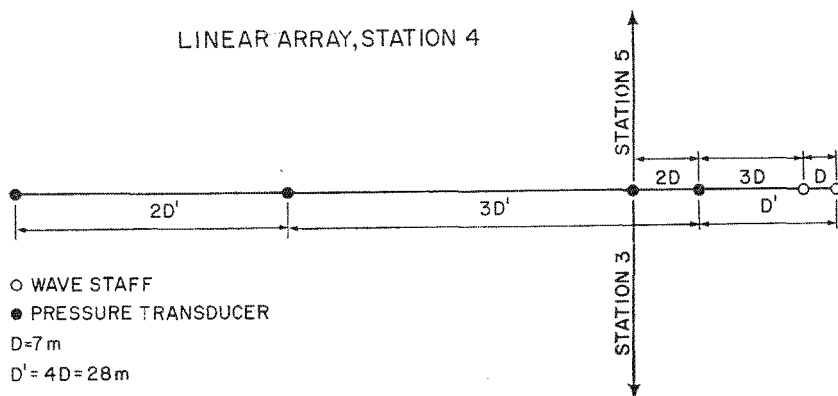


Fig. 1.5. The linear array at Station 4

$4D, 6D$  ( $D = 7\text{ m}$  and  $28\text{ m}$ ) yielding the 6 lags  $r_{ij} = D, 2D, \dots 6D$ . Each subarray provided directional information (depending somewhat on the distribution assumed) in wavelength bands between about 10 m and 150 m, and 40 m and 600 m, respectively.

On account of their mirror symmetry linear arrays are unable to distinguish between waves approaching the array at the same angle but from opposite sides of the array, i.e. at

angles  $\theta$  and  $\pi - \theta$ . This ambiguity was not regarded as a serious limitation in the present experiment. The smaller-scale array was designed to resolve the directional distribution of short, locally generated waves under east-wind conditions, whereas the larger-scale array was used to determine the propagation direction of incoming swell. In both cases only one of the two wavenumber half-planes contained significant energy.

A number of techniques have been developed for the directional analysis of multisensor arrays. In our case, the details of the directional distributions turned out to be uncritical for the interpretation of the data. Thus in the wave-growth study, values of the mean propagation direction and mean square directional spread proved adequate to compute and interpret the source function to within the error limits imposed by other factors of the experiment. The same parameters were also sufficient to characterize an incoming swell beam. (Spectra containing two swell components with the same frequency but different propagation directions were very seldom.)

Consequently, the directional data were analyzed and compared primarily with respect to the two simplest directional parameters, defined (in terms of the pitch-roll data) as

$$\theta_m = \arctan \frac{\bar{k}_2}{\bar{k}_1} \approx \int_{-\pi}^{+\pi} s(\theta) \theta d\theta,$$

$$\theta_s = \left( 1 - \frac{\bar{k}_1^2 + \bar{k}_2^2}{\bar{k}^2} \right)^{1/2} \approx \left[ \int_{-\pi}^{+\pi} s(\theta) (\theta - \theta_m)^2 d\theta \right]^{1/2}.$$

In the limit of a narrow beam, these are identical with the mean direction and r.m.s. directional spread, as defined by the integrals on the right hand side\*.

Although this made only partial use of the available directional resolution, no attempt was made at a systematic, high-resolution analysis, except for occasional spot checks of the consistency of the remaining directional moments with respect to the two-parameter directional models used.

Apart from the insensitivity of our conclusions to the details of the directional distribution, this approach was also motivated by experimental difficulties. Although extensively tested in individual measurements, the compass units of the pitch-roll buoys were apparently unable to withstand the continual mode of operation required for this experiment, and only one of the five instruments yielded reliable directional data throughout the entire period. Also, an early failure of the digital data logging system for the linear array meant that much of this data had to be recovered from analog traces by painstaking semiautomatic digitalization. The restriction to two directional parameters had the advantage in this case that they could be derived from only two sensors of the array.

Analogous variables to  $\theta_m$  and  $\theta_s$  for two wave sensors separated by a distance  $r$  orthogonal to the profile may be defined as

$$\theta'_m = \arcsin \left( \frac{\arctan Q/C}{kr} \right)$$

$$\theta'_s = \frac{1 - R^2}{(kr \cos \theta'_m)^2}, \quad \text{where the coherence } R = \left( \frac{C^2 + Q^2}{E^2} \right)^{1/2}$$

and we have dropped the subscripts  $ij$  on  $C$ ,  $Q$  and  $r$ . For a narrow beam  $\theta'_m, \theta'_s \rightarrow \theta_m, \theta_s$ .

\* In contrast to the definitions in terms of  $k_j$ , the latter integrals represent meaningful quantities only in the narrow beam limit. On account of the non-periodicity of the integrand, they are not invariant with respect to redefinition of the  $\theta$  interval, say from  $(-\pi, \pi)$  to  $(0, 2\pi)$ , for arbitrary distributions  $s(\theta)$ .



To compare the directional estimates from the pitch-roll and linear array measurements, a standard spreading function model was assumed,

$$s(f, \theta) = \begin{cases} \Delta^{-1} \cos^{2p}(\theta - \theta_m), & |\theta - \theta_m| \leq \pi/2 \\ 0, & \pi/2 \leq |\theta - \theta_m| \leq \pi \end{cases}$$

where  $\Delta$  is a normalising parameter, making

$$\int_{-\pi}^{+\pi} s \, d\theta = 1.$$

Fig. 1.6a shows the relation between  $\theta_m$  and  $\theta'_m$  for  $kr = 1$  and different beam widths  $\theta_s$ , as characterized by the parameter  $p$ . The corresponding relation between  $\theta_s$  and  $\theta'_s$  as a function of the propagation direction  $\theta_m$  is shown in Fig. 1.6b.

Similar curves were computed for other models of the spreading function, some including a skewness factor. The transformation was found to be rather insensitive to the choice of model.

With the aid of Figs. 1.6a and b, the linear-array directional data could be converted to equivalent pitch-roll directional parameters. A typical intercomparison run at Station 4, showing satisfactory agreement of the directional parameters after conversion, is presented in Fig. 1.7.

## 1.6. Cases Studied

Fig. 1.8 shows the general wind history for the three periods of the experiment. Wind directions are defined relative to the profile, arrows pointing vertically upwards representing offshore winds parallel to the profile. The arrows represent averages of the winds measured at given time along the profile.

Wave growth was investigated for the periods marked G; the symbols IG refer to "ideal generation" conditions of high stationarity and homogeneity, which were selected for more detailed study. A more complete time history of the wind fields during these periods and weather maps are presented in Part 2.

Periods marked S were selected for the swell attenuation study. The term swell is normally applied to waves no longer being actively generated by the wind, i.e. in the present case, waves travelling inshore at phase speeds exceeding the onshore component of the local wind velocity. Usually, these conditions apply only after the waves have travelled a sufficient distance from the wave source for dispersion to have converted the swell spectrum into the classical form of a narrow low frequency peak. However, in the present experiment several cases also occurred where the local wind field died down rather rapidly, leaving a locally generated, broad-band swell spectrum. We have investigated here only "classical" swell cases in which the width of the swell peak was narrow compared with the swell frequency. This was because our main interest concerned the bottom interactions, which we wished to separate as far as possible from other dynamical processes. Computations (K. Hasselmann [1963b]) and experiments (F. E. Snodgrass et al. [1966], H. Mitsuyasu [1968b]) indicate that nonlinear wave-wave interactions are important for the energy balance of a broad-band, newly created swell spectrum, whereas they can be neglected for a well dispersed swell train\* (provided the frequency lies below the frequencies of the local background wind sea).

The generation and swell cases studied in this paper have been chosen from a much larger ensemble of measured spectra. They represent the simplest situations for investigating the basic processes that presumably also control the evolution of the wave spectrum in the general case of an arbitrary wind field and boundary condition. The interpretation of the

\* The essential condition is that the swell energy is small relative to a newly created swell. In some of the quasi-stationary swell cases considered in Part 2, this was caused by angular dispersion alone, rather than the usual combination of angular and frequency dispersion.

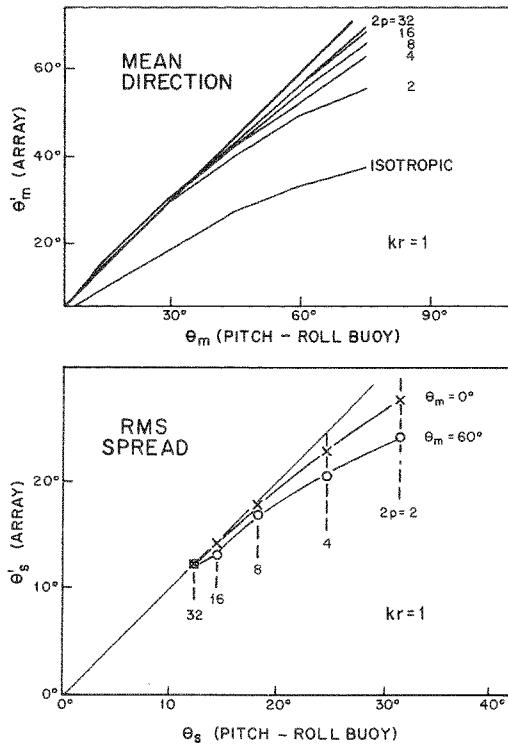


Fig. 1.6. a,b. Relation between parameters characterizing the mean direction (a) and directional spread (b) for the pitch-roll buoys and the linear array. A  $\cos^2 \theta$  spreading factor is assumed

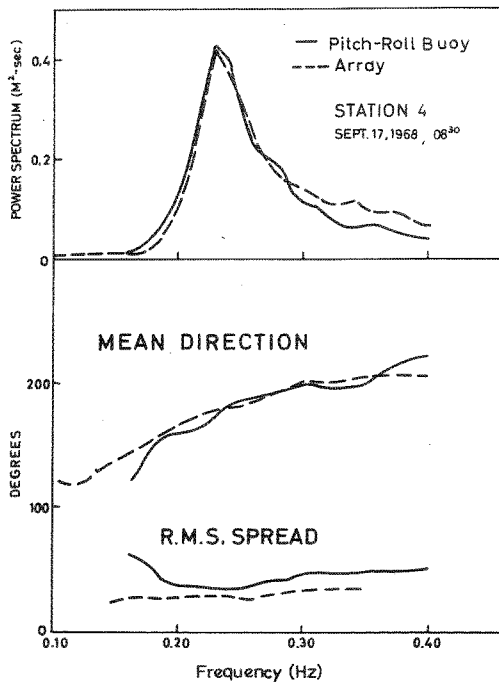


Fig. 1.7. Intercomparison of frequency spectrum and directional parameters for a pitch-roll buoy and the linear array



remaining data would require more sophisticated analysis techniques than used here, including the numerical integration of the energy balance equation for time and space dependent wind fields.

Edited data tapes of the complete set of wave spectra are available on request from the National Oceanographic Data Center, U.S.A., the Institut für Geophysik, University of Hamburg, or the Deutsches Hydrographisches Institut, Hamburg. Wind and other environmental data are available from the latter two institutions.

### 1.7. Logistics

Overall logistic coordination of the experiment was carried out by the Deutsches Hydrographische Institut (HW)\*, Hamburg, with assistance from the Institut für Geophysik, University of Hamburg (KH). Site preparation and technical coordination of field operations were handled by A. Hedrich through the Deutsches Hydrographisches Institut. Scientific communication during the experiment was maintained from the shore-based telemetry and radio station (1968: KH; 1969: HW, KH) for which accommodation was kindly provided by U. Jessel, Institut für Bioklimatologie und Meeresheilkunde. Within this general logistic framework, each participating group carried individual responsibility for its contribution to the experiment, as follows (see also T. P. Barnett [1970]):

**Deutsches Hydrographisches Institut. 1968:** Wave posts at Stations 2 and 8 (Carstens).

3 pitch-roll buoys operated from "Walter Körte" (KR), "OT2" (HC, H. Frentz), and "Gauss" (H. J. Rubach, P. Lindner). Tide gauges at Stations 2 and 8. Current meters.

**1969:** Wave posts at Stations 1, 2, 3, 5 and 8 (U. Carstens, Rossfeld, HG); 4 pitch-roll buoys operated from "Walter Körte" (KR), "OT2" (HC, H. Frentz), "Gauss" (H. J. Rubach, P. Lindner), and "Holnis" (R. Fuhrmann); (one of the pitch-roll buoys was loaned from the National Institute of Oceanography). The telemetry and data acquisition system for the wave posts and turbulence instrumentation were built by U. Carstens. Wave posts for the DHI wave instruments were built and installed (by jetting into the sandy bottom) by Harms & Co. (S. Knabe). Tide gauges at Stations 2 and 8.

**Institut für Geophysik, Hamburg. 1969:** Turbulence measurements, Station 8 (O. Kertelhein, KE, DO). The turbulence instrumentation was built by O. Kertelhein.

**Koninklijk Nederlands Meteorologisch Instituut. 1968:** Three waverider buoys (AM).

**1969:** Waverider buoys at Stations 7, 9 and 10 (EB). The waverider system, complete with telemetry and data acquisition system, was built by Datawell NV.

**National Institute of Oceanography. 1968:** Two pitch-roll buoys, operated from HMS

"Enterprise" (JE, D. Bishop) and HMS "Bulldog" (N. Smith, P. Collins). **1969:** Pitch-roll buoy at Station 13, operated from "Moray Firth" (DC, JE, P. Collins, C. Clayson). A second pitch-roll buoy was loaned to the Deutsches Hydrographisches Institut.

**Westinghouse Research Laboratories. 1968:** Six-instrument array at Station 4, pressure transducers at Stations 1 and 3 (R. Bower, H. Martin, TB). **1969:** Six-instrument array at Station 4 (R. Bower, H. Martin, G. Bowman, TB). The wave instrumentation and telemetry were built by H. Martin, Ocean Applied Research Corp., San Diego.

During the experiment the telemetering Stations 1-5, 7-10 were serviced by the tugs "Föhr" (1968) and "Friedrich Voge" (1969), with support from air-sea rescue launches based in the Bundesmarine Station in List and occasionally the life vessel "Hindenburg".

The preliminary editing and spectral analysis of the data was carried out by each group individually. A general system for assembling and processing the complete set of spectra

\* Initials refer to authors.

was developed by WS. The analysis and interpretation of the data was then carried out during two workshops at the Woods Hole Oceanographic Institution from February to April, 1971 (WS, KH, JE, DH, PM, TB, EB, HC) and May–August, 1971 (WS, KH, EB, HC, DO, PM). Computations of the nonlinear energy transfer rates were made on the CDC 6600 and 7600 computers at the National Center of Atmospheric Research in Boulder (WS, KH). Woods Hole Oceanographic Institution provided assistance during the preparation of a first draft of this paper (KH)\*.

### Acknowledgments

The work was supported by the Ministerium für Bildung und Wissenschaft, the Verteidigungsministerium, and the Verkehrsministerium (FRG); the Office of Naval Research, the National Science Foundation [NCAR], and the Woods Hole Oceanographic Institution [Doherty Fund] (USA); the Natural Environment Research Council and the British Ministry of Defence (UK); and the NATO Science Committee. Ships were made available through the Verteidigungsministerium, Bundesmarine ("OT2", "Holnis", "Föhr", "Friedrich Voge", air sea rescue boats); the UK Hydrographic Dept., M.O.D. (HMS "Enterprise" and "Bulldog"); the UK Natural Environment Research Council (charter for "Moray Firth"); the Wasser- und Schifffahrtsdirektion Hamburg ("Walter Korte"); the Deutsches Hydrographisches Institut ("Gauss"); and the Deutsche Gesellschaft zur Rettung Schiffbrüchiger ("Hindenburg").

We are grateful to these agencies and the individuals mentioned in the previous section, and numerous others not listed explicitly whose generous assistance and support made this project possible.

---

\* This paper also appears in the Collected Reprints of the Woods Hole Oceanographic Institution as contribution no. 2911.

## 2. Wave Growth

### 2.1. Generation Cases

The primary purpose of the wave generation measurements was to determine the source function  $S'$  in the spectral energy balance (radiative transfer) equation\*

$$\frac{\partial F}{\partial t} + v_i \frac{\partial F}{\partial x_i} = S' \quad (2.1.1)$$

for the two-dimensional wave spectrum  $F(f, \theta; x, t)$ , where  $v_i = \frac{d\omega}{dk_i} = \frac{g}{4\pi f} \cdot \frac{k_i}{k}$  is the group velocity.

Much of the discussion will, in fact, center on the contracted form of this equation obtained by integrating over the propagation direction  $\theta$ ,

$$\frac{\partial E}{\partial t} + \bar{v}_i \frac{\partial E}{\partial x_i} = S \quad (2.1.2)$$

where  $E = E(f; x, t)$  and  $S$  are the one-dimensional frequency spectrum and source function, respectively, and  $\bar{v}_i = \int v_i F d\theta / E$ .

In either equation the source function can be determined from wave data taken along the profile only if the gradient of the wave spectrum transverse to the profile is small compared with the derivative parallel to the profile. For an ideal geometry consisting of a profile perpendicular to an infinite straight shore, this will be the case if the wind field is homogeneous with respect to the parallel-to-shore coordinate  $x_2 = y$ . The direction of the wind and the wind-field variations with respect to the coordinate  $x_1 = x$  parallel to the profile or time  $t$  may be arbitrary. However, in practice, the length of straight shoreline perpendicular to the profile was finite (cf. Figs. 1.1 and 1.2) and we felt reasonably confident that transverse gradients could be neglected in Eqs. (2.1.1) or (2.1.2) only for offshore winds blowing within about  $\pm 30^\circ$  of the profile direction. Although no restrictions were necessary with respect to the fetch or time variability of the wind field, the conditions on the wind directions were then normally satisfied only for wind fields which were also fairly homogeneous with respect to  $x$  and  $t$ .

S. A. Kitaigorodskii [1962] has suggested that under these conditions the wave data for different wind speeds and fetches should be expressible in terms of a single nondimensional fetch parameter  $\hat{x} = gx/u_*^2$ , where  $u_* = (\tau/\rho_a)^{1/2}$  is the friction velocity and  $\tau$  is the momentum transfer across the air-sea interface ( $\rho_a$  = density of air). We found Kitaigorodskii's relation to be fairly well satisfied, and the source functions computed for individual cases agreed reasonably well with the mean source function inferred from the  $\hat{x}$ -dependence of the wave spectra after averaging over all "ideal" cases of stationary, homogeneous wind fields. Many of our general conclusions have accordingly been derived from the mean spectral distributions after scaling with respect to nondimensional fetch (Sections 2.3–2.6).

However, a number of individual generation cases were also analyzed (Section 2.7) to indicate the variability of the data and the representativeness of the mean results, including possible limitations of Kitaigorodskii's scaling law. It appeared that most of the observed variability of our data was associated with the small scale gustiness of the wind field rather than systematic deviations from Kitaigorodskii's law. Nevertheless, there is some indication that further parameters not included in Kitaigorodskii's analysis, such as boundary-layer scales, must be taken into account in comparing laboratory and field data.

\* We ignore refractive effects in this section, but will consider the full equation in Part 3.

## 2.2. Kitaigorodskii's Similarity Law

Kitaigorodskii has pointed out that if the geometry of the wind field and the laws of wave generation are sufficiently simple that the wave spectrum can be uniquely specified by a single fetch parameter  $x$ , the local friction velocity  $u_*$  and the gravitational acceleration  $g$ , then by dimensional arguments the spectrum must be of the general form

$$F(f, \theta) = g^2 f^{-5} \hat{F}(\hat{f}, \theta; \hat{x}) \quad (2.2.1)$$

where the parameters  $\hat{f} = fu_*/g$ ,  $\hat{x} = gx/u_*^2$  and the function  $\hat{F}$  are non-dimensional quantities.

Clearly the general three-dimensional space-time dependence of the wave field will reduce to a single fetch parameter  $x$  if the wind field and boundary conditions are stationary and homogeneous with respect to the direction  $y$  perpendicular to  $x$ , e.g. for a constant offshore wind blowing perpendicular to an infinite straight shore.

However, it is less obvious that the spectrum should depend in addition only on the local friction velocity  $u_*$  (besides  $g$ ). Although it appears reasonable to assume that the friction velocity  $u_*$  can adequately characterise the local interaction between the atmosphere and the wave field – at least to first order – this is relevant only for the local rate of change of the spectrum. The spectrum itself must be determined by integrating the radiative transfer equation and thus represents a net response to the entire upwind wind field. To avoid this difficulty, one could assume that  $u_*$  is constant, i.e. independent of fetch. Although this finds some observational support, it is difficult to find a convincing physical reason why this should be the case a priori, unless it is assumed that the wave field plays a negligible role in the momentum transfer across the air-sea interface – which is not supported by experiment. It appears more consistent to regard  $u_*$  instead as an internal variable of the problem which has to be determined as a function of fetch in the same way as the spectrum.

Adopting this viewpoint, Kitaigorodskii's spectrum (2.2.1) can nevertheless be derived by the following, slightly revised argument. As relevant external parameter we specify the constant wind speed  $U_\infty$  at some height above the sea surface which is no longer significantly affected by the wave field – ideally, outside the planetary boundary layer. The wave spectrum and  $u_*$  are then governed by the coupled radiative transfer and atmospheric boundary-layer equations under appropriate upwind initial conditions. Assuming that the wave spectrum is zero at the upwind shore line  $x=0$  and that at a sufficient distance from the coast the initial properties of the boundary layer at  $x=0$  are no longer important, it follows that the spectrum and friction velocity can be functions of  $x$ ,  $U_\infty$  and  $g$  only. Hence by the same dimensional argument as employed by Kitaigorodskii, the spectrum must be of the general form (2.2.1) with  $\hat{f}$  and  $\hat{x}$  replaced by  $f' = fU_\infty/g$  and  $x' = gx/U_\infty^2$ . Similarly,  $u_*/U_\infty$  must be a universal function  $\mu(x')$  of the nondimensional fetch  $x'$ . However, both scaling laws are equivalent, as is seen by writing  $\hat{F}(\hat{f}, \theta, \hat{x}) = \hat{F}(f'\mu, \theta, x'\mu^{-2}) = \psi(f', \theta, x')$ , say.

Clearly, the same argument would have applied if  $u_*$  had been replaced by some other characteristic boundary-layer velocity, e.g. the velocity  $U_{10}$  at 10 m height above the surface. Since  $U_{10}$  is easier to measure than  $u_*$  and was routinely determined at most stations along the profile, we have scaled all our data in the following with respect to  $U_{10}$  rather than  $u_*$ , denoting the appropriate variables by  $\tilde{x} = gx/U_{10}^2$ ,  $\tilde{f} = fU_{10}/g$ , etc. For comparison with data from other authors, however, we have also included axes for the corresponding variables scaled with respect to  $u_*$  using the relation  $u_*^2 = c_{10} U_{10}^2$  with a constant drag coefficient  $c_{10} = 1.0 \times 10^{-3}$ .

## 2.3. Wind Stress and Turbulence Measurements

During the main 1969 experiment, drag coefficients were determined at Station 8 from turbulent momentum flux measurements using both hot-wire and cup-and-vane anemometers (cf. 1. 3. A more detailed description of the apparatus is given in K. Enke [1973]). For neutral or stable conditions the average value of  $c_{10}$  was found to lie fairly close to the value  $1.0 \times 10^{-3}$

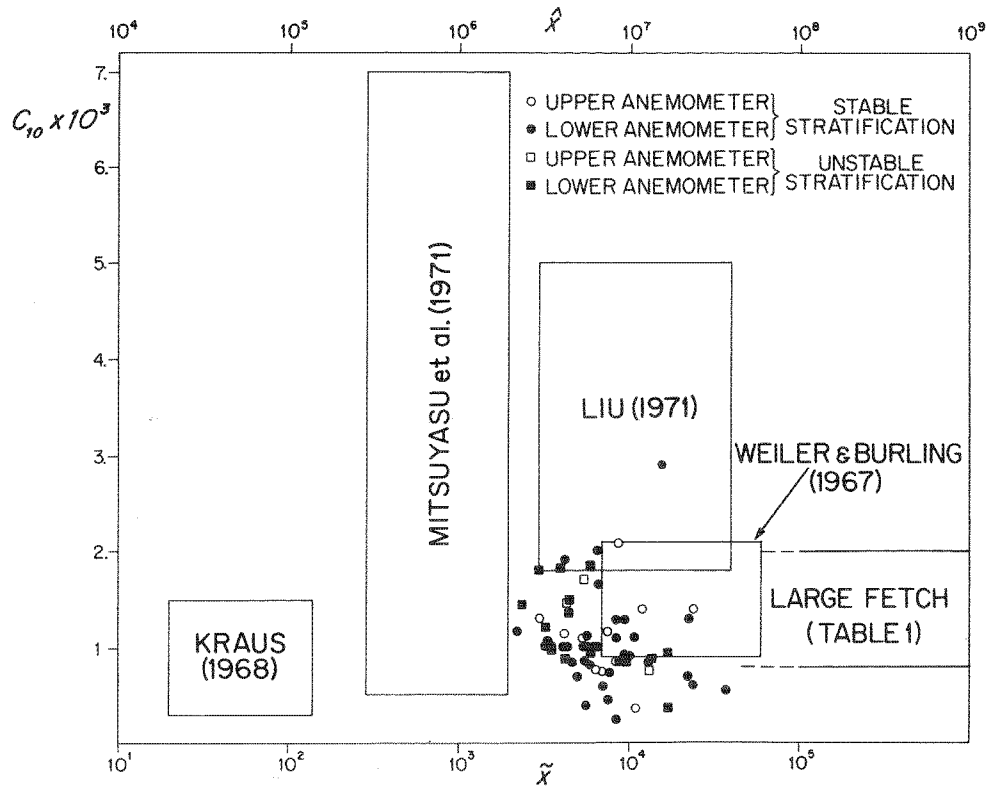


Fig. 2.1. Drag coefficients  $c_{10}$  versus non-dimensional fetch  $\tilde{X} = gx/U_{10}^2$ . Large-fetch measurements are listed in Table 1

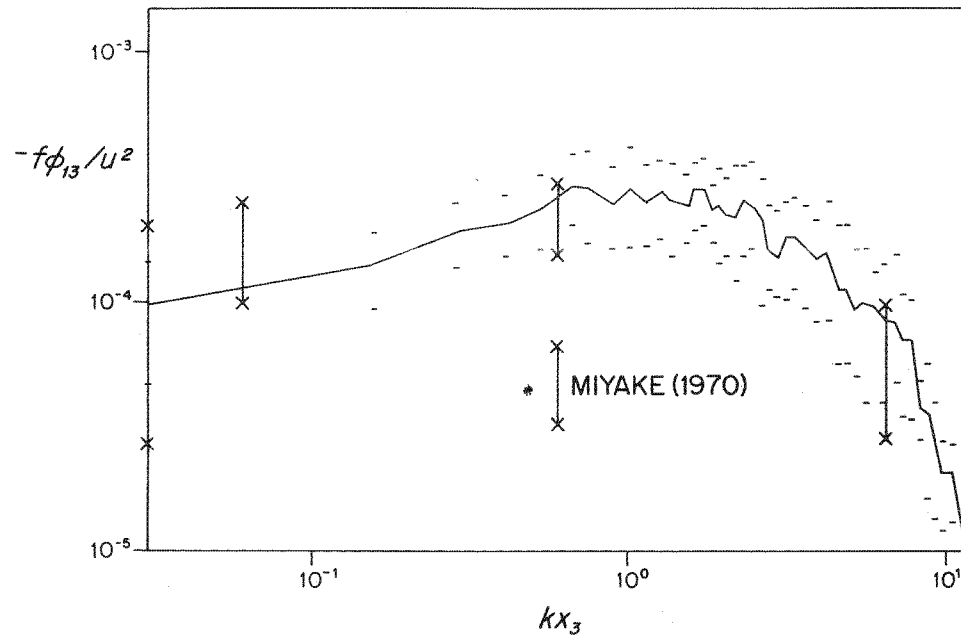


Fig. 2.2. Reynolds stress spectrum ( $k = 2\pi/l$ ,  $x_3$  = anemometer height,  $U \approx U_{10}$ )



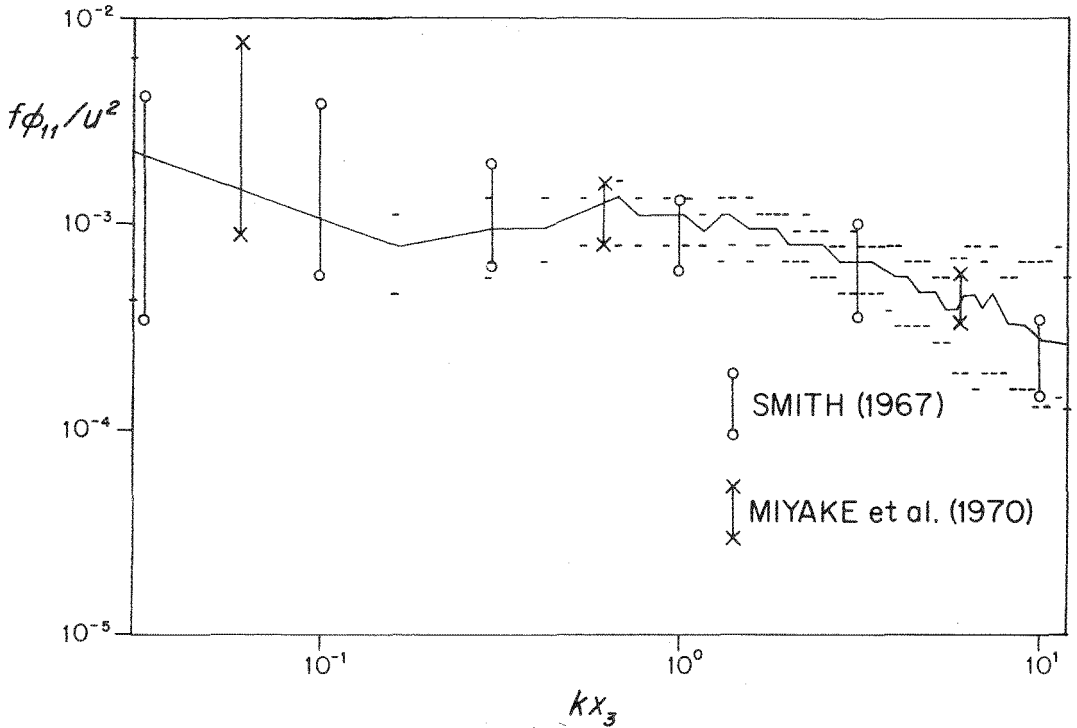


Fig. 2.3. Spectrum of horizontal turbulence parallel to wind ( $k = 2\pi/l/U_{10}$ ,  $x_3$  = anemometer height,  $U \approx U_{10}$ )

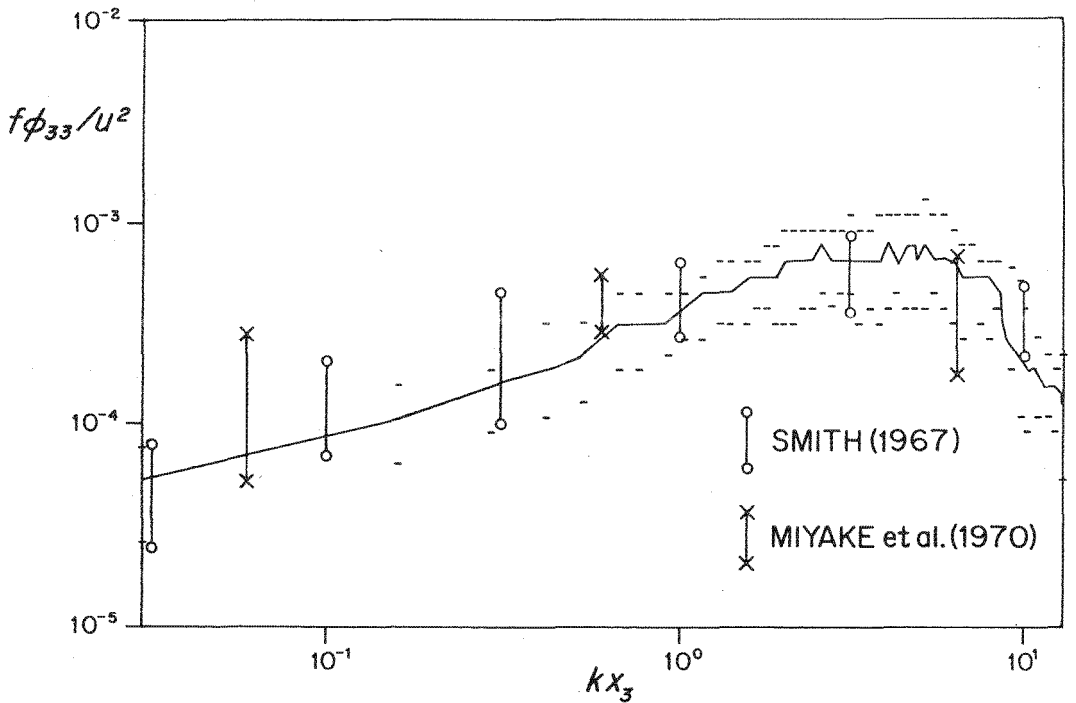


Fig. 2.4. Spectrum of vertical turbulence ( $k = 2\pi/l/U_{10}$ ,  $x_3$  = anemometer height,  $U \approx U_{10}$ )

applied in the previous section. Under these conditions no systematic dependence of the drag coefficient on  $\bar{x}$  was found, cf. Fig. 2.1. Slightly larger drag coefficients were found for unstable air-sea temperature differences, with indication of a decreasing  $c_{10}$  trend with increasing  $\bar{x}$ . Since most of our wave data were obtained under stable conditions, we have ignored the temperature dependence in converting from  $U_{10}$  to  $u_*$ . This procedure is consistent with Kitaigorodskii's scaling law, which also disregards temperature effects.

Figure 2.1 and Table 1 indicate considerable variability in the drag coefficients measured by different groups. This causes difficulties in applying Kitaigorodskii's scaling law, which can be expected to be valid only if  $c_{10}$  is a unique function of the non-dimensional fetch  $\bar{x}$ . In the literature, wave parameters are usually presented in nondimensional form with respect to  $u_*$ . To compare wave data from other sources with our data in Figs. 2.6, 2.7 (Section 2.4) we have simply plotted all parameters with respect to our axes – although the drag coefficient  $c_{10} = 10^{-3}$  used to convert from  $U$  to  $u_*$  may differ from that used in the original source. Slightly different plots would have resulted if all data had been non-dimensionalized with respect to  $U_{10}$ . (In practice, however, variations of  $c_{10}$  by a factor of 2 or 3 are not very noticeable in the log-log plots of Figs. 2.6, 2.7.)

Table 1  
Large Fetch Values of  $c_{10}$

Author	$c_{10} \cdot 10^3$	$U_{10}$	Stratification	Method
Smith [1967]	$0.9 \pm 0.24$	m/s 3–13		correlation
Smith [1970]	$1.35 \pm 0.34$ $1.41 \pm 0.26$ $1.20 \pm 0.48$	6–15	stable	correlation
Hasse [1968]	$1.21 \pm 0.24$	3–11		correlation
Brocks et al. [1970]	$1.30 \pm 0.18$	3–13	neutral	profile
DeLeonibus [1971]	$0.8 \pm 0.4$ $1.2 \pm 0.4$ $1.3 \pm 0.6$	3–15	stable neutral unstable	correlation
Pond et al. [1971]	$1.52 \pm 0.26$	4–7		correlation
JONSWAP	$1.0 \pm 0.4$ $1.2 \pm 0.4$	3–11	stable unstable	correlation

The mean spectrum of the shear stress and its r.m.s. variation over the set of measurements are presented in Fig. 2.2. Figures 2.3 and 2.4 show the corresponding spectra for the horizontal and vertical velocities. The distributions agree quite well with measurements by other workers.

Cross spectra between atmospheric turbulence fluctuations and the surface displacements, which were measured at the same position, were also analyzed, but no significant correlations were detected. The ratio anemometer height to the wavelength of the principal wave component was typically of the order 0.2. J. Elliott [1972] also found no correlation for comparable ratios\*. It appears that turbulence measurements considerably closer to the surface are needed to study wave-induced velocity fluctuations.

\* However, both Elliott and we observed correlations for swell components whose phase velocities exceeded the wind speed – as have a number of other authors. The phases were in accordance with potential theory.

## 2.4. Fetch Dependence of One-Dimensional Spectra

The fetch dependence of the one-dimensional frequency spectra were investigated by parametrizing them with a least-square fitted analytic function. Various functional forms were tried. A uniform good fit to nearly all of the spectra observed during "ideal" generation conditions was finally attained by the function

$$E(f) = \alpha g^2 (2\pi)^{-4} f^{-5} \exp\left(-\frac{5}{4}\left(\frac{f}{f_m}\right)^{-4}\right) \gamma \exp\left(-\frac{(f-f_m)^2}{2\sigma^2 f_m^2}\right) \quad (2.4.1)$$

$$\sigma = \begin{cases} \sigma_a & \text{for } f \leq f_m \\ \sigma_b & \text{for } f > f_m \end{cases}$$

containing five free parameters  $f_m$ ,  $\alpha$ ,  $\gamma$ ,  $\sigma_a$  and  $\sigma_b$ .

Here  $f_m$  represents the frequency at the maximum of the spectrum and the parameter  $\alpha$  corresponds to the usual Phillips constant (the spectrum approaches the usual  $f^{-5}$  power law for large  $f/f_m$ ). The remaining three parameters define the shape of the spectrum:  $\gamma$  is the ratio of the maximal spectral energy to the maximum of the corresponding Pierson-Moskowitz [1964] spectrum\*

$$E_{PM}(f) = \alpha g^2 (2\pi)^{-4} f^{-5} \exp\left[-\frac{5}{4}\left(\frac{f}{f_m}\right)^{-4}\right] \quad (2.4.2)$$

with the same values of  $\alpha$  and  $f_m$ ;  $\sigma_a$  and  $\sigma_b$  define the left and right sided widths, respectively, of the spectral peak. The functional form (2.4.1) was obtained by multiplying a Pierson-Moskowitz spectrum with the "peak enhancement" factor

$$\gamma \exp\left(-\frac{(f-f_m)^2}{2\sigma^2 f_m^2}\right).$$

The purpose of the parametrization was not to contribute a further empirical spectrum, but rather to reduce the 100 frequency points of the measured spectra to a manageable, non-redundant subset of parameters whose dependence on fetch, windspeed and other factors could be systematically investigated. (The parametrization also had advantages in differentiating the spectra to determine the source functions, cf. Sections 2.6, 2.7). Formulae for fetch-limited spectra proposed by other authors, while perhaps adequate to describe certain properties of mean spectra, were found to contain too few parameters to characterize the variations encountered in the individual measured spectra.

Fig. 2.5 shows a typical series of spectra measured under "ideal" generation conditions, together with their parametrical approximations. Plots of the five spectral parameters for the 121 spectra measured under "ideal" generation conditions against nondimensional fetch  $\bar{x} = gx/U_{10}^2$  are shown in Figures 2.6, 2.7 and 2.8. Figures 2.6 and 2.7 also include scale parameters  $f_m$  and  $\alpha$  from other experiments.

The  $f_m$  distribution exhibits the smallest scatter. In part this may be due to the fact that  $f_m$  is the most accurately defined spectral parameter. However, the smaller variability of the  $f_m$  distribution as compared with the  $\alpha$  data or the still more scattered shape parameters can also be understood from the origin of the scatter, which we attribute in Section 2.9 to the gustiness of the wind.

\* The exponent of the Pierson-Moskowitz spectrum is normally written as  $-0.74 (f/f_w)^{-4}$  with reference to the frequency  $f_w = g/2\pi U_{10}$  for which the phase speed of the waves is equal to the wind speed. The two expressions are identical, but in our case  $f_m$  - or equivalently  $f_w$  - is treated as an adjustable parameter.

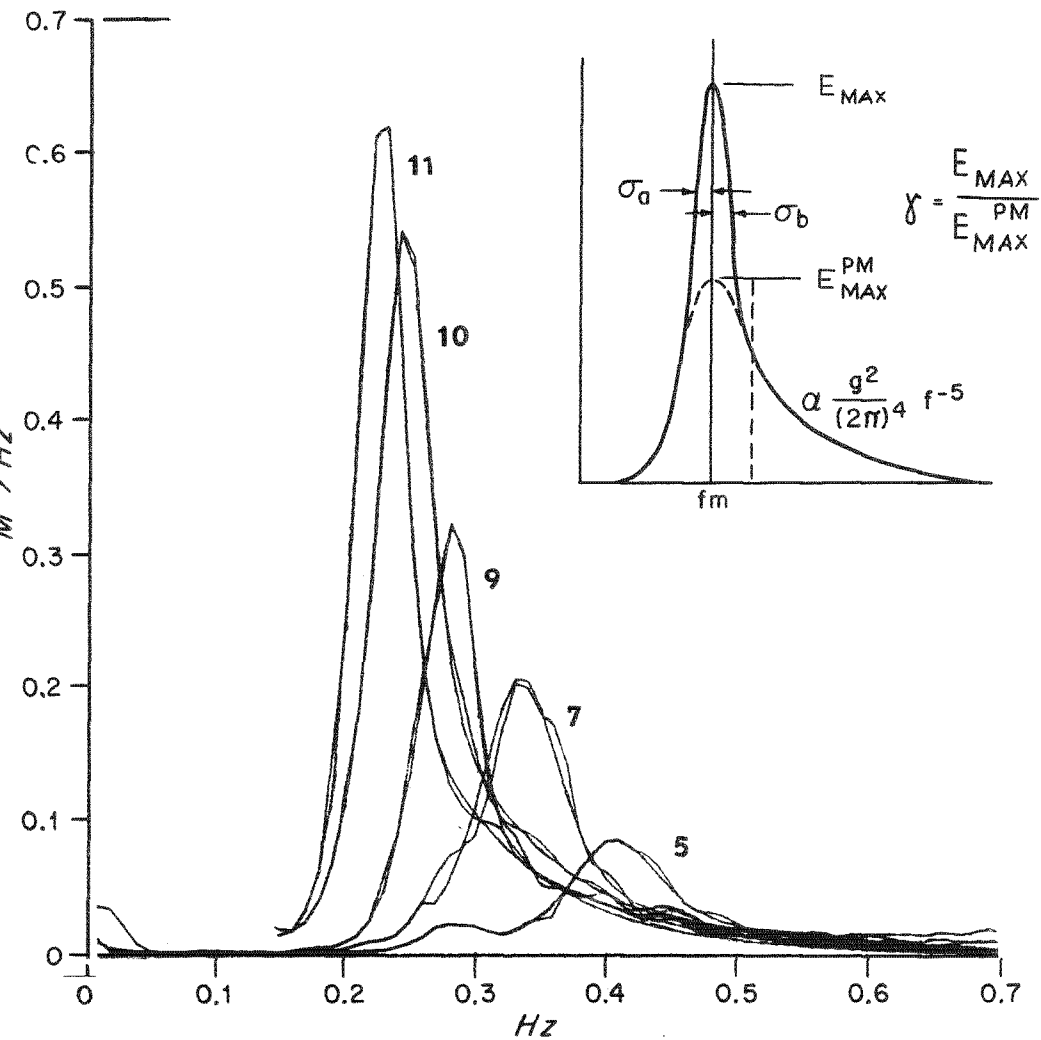


Fig. 2.5. Evolution of wave spectrum with fetch for offshore winds ( $11^{\text{h}} - 12^{\text{h}}$ , Sept. 15, 1968). Numbers refer to stations (cf. Fig. 1.2.).

The best-fit analytical spectra (2.4.1) are also shown. The inset illustrates the definition of the five free parameters in form (2.4.1)

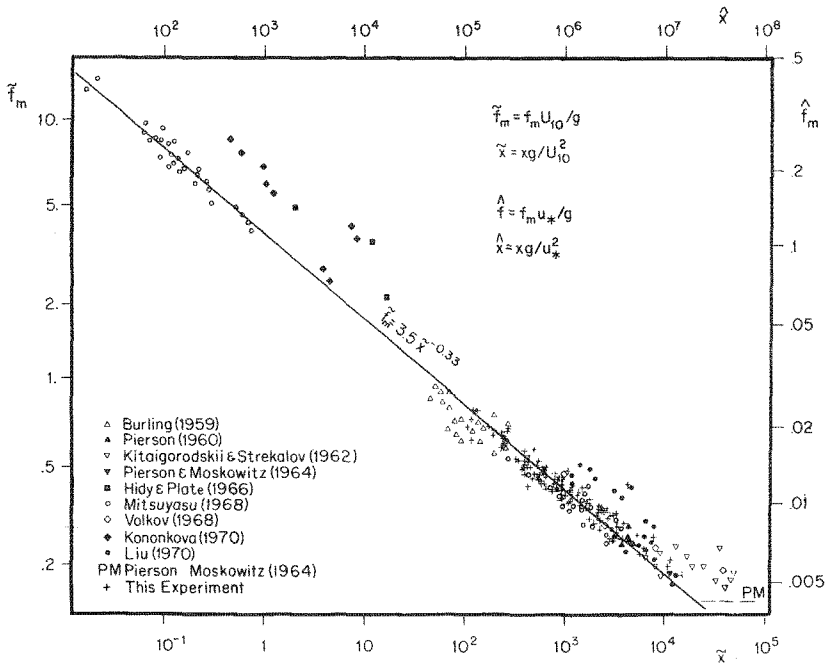


Fig. 2.6. Peak frequency v. fetch scaled according to Kitaigorodskii. Data at small fetches are obtained from wind-wave tanks. (Capillary-wave data was excluded where possible.)

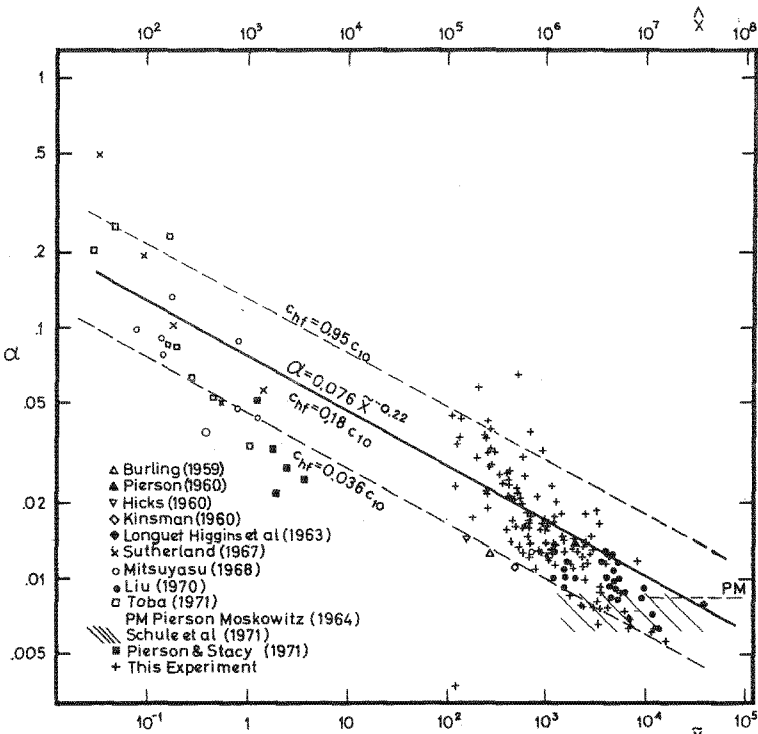
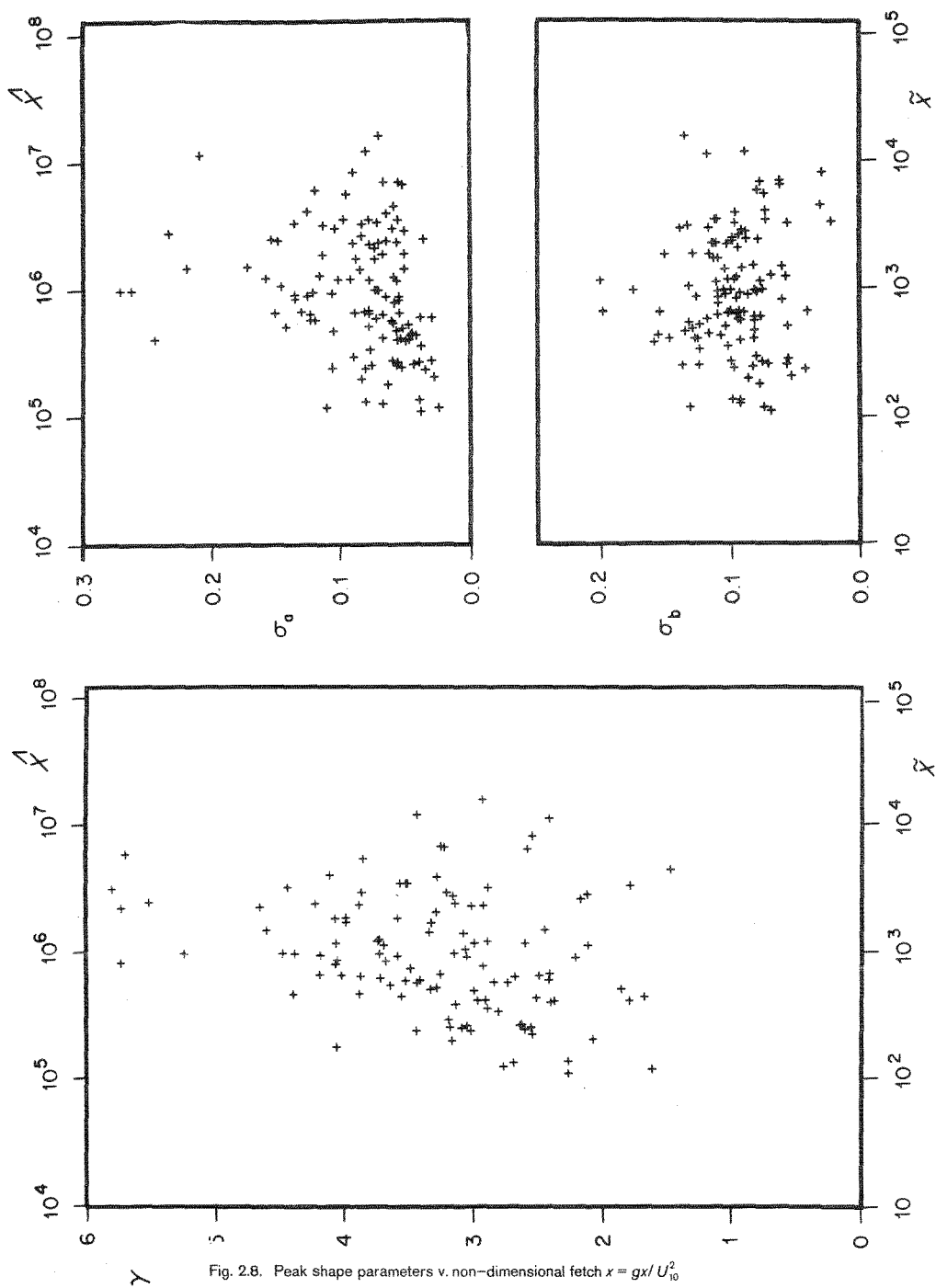


Fig. 2.7. Phillips constant v. fetch scaled according to Kitaigorodskii. Small-fetch data are obtained from wind-wave tanks. (Capillary-wave data was excluded where possible.) Measurements by Sutherland (1967) and Toba (1971) were taken from W.J. Pierson and R.A. Stacy [1973]

Fig. 2.8. Peak shape parameters v. non-dimensional fetch  $x = gx/U_{10}^2$

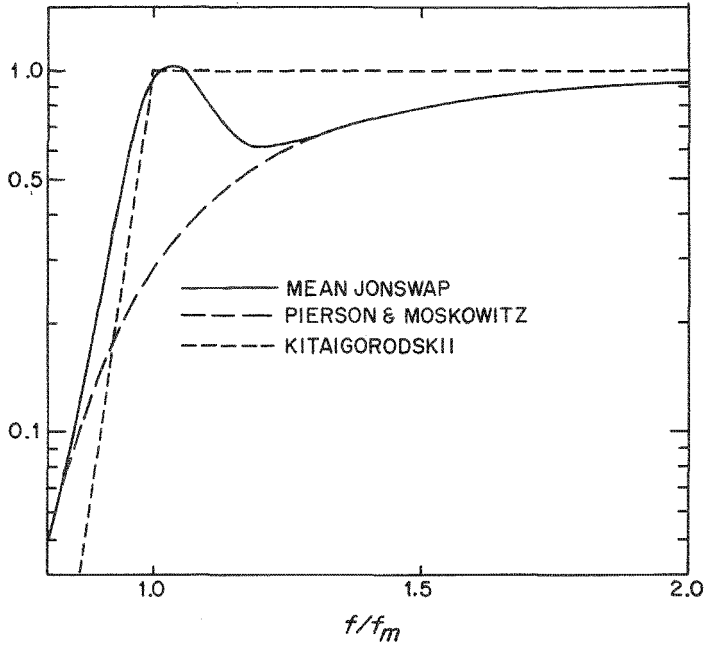


Fig. 2.9. Shape function  $\psi = E(f) / [\alpha g^2 (2\pi)^{-4} f^{-5}]$

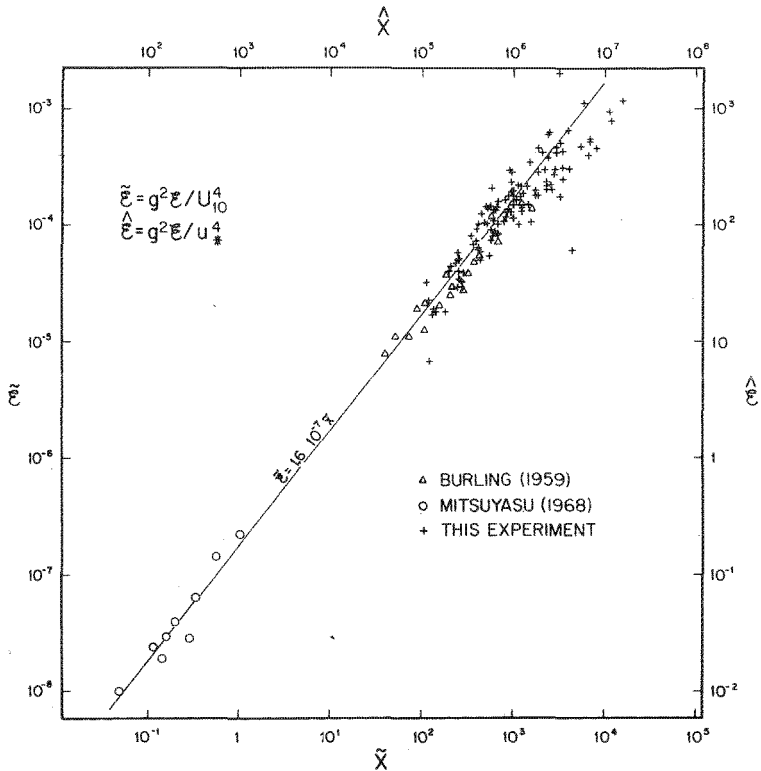


Fig. 2.10. Energy v. fetch scaled according to Kitaigorodskii. Data at small fetches are obtained from wind-wave tanks

Our  $\alpha$  parameters in Fig. 2.7 are seen to lie a little higher than the data from some of the other groups. This may be due partly to the function-fitting techniques used to evaluate  $\alpha$ . H. Mitsuyasu [1969] for example, mentions three methods, of which the one used for the  $\alpha$  values shown in Fig. 2.7 yielded systematically smaller estimates by 10 to 20 % than the other two. Our technique of simultaneously optimizing five spectral parameters tended to yield  $\alpha$  values about 20 % higher than, say, a straight-line fit to the function  $E(f) f^5$  for all frequencies  $f$  greater than  $f_m$ , which corresponds more closely to the standard method.

A significant feature of Fig. 2.7 is that  $\alpha$  is clearly not a universal constant, as required by Phillips' original dimensional argument. Our analysis of the source functions presented later in Sections 2.6–2.9 indicates that the energy balance in the  $f^{-5}$  region of the spectrum between  $f_m$  and about  $3 f_m$  is indeed not governed by white-capping, as envisaged by Phillips, but primarily by the energy input from the atmosphere and the nonlinear energy transfer by wave-wave interactions towards lower and higher frequencies\*.

The straight line

$$f_m = 3.5 \bar{x}^{-0.33} \quad (2.4.3)$$

in Fig. 2.6 represents the best fit to the data (H. Mitsuyasu [1969] finds the same exponent); the line

$$\alpha = 0.076 \bar{x}^{-0.22} \quad (2.4.4)$$

in Fig. 2.7 is based on dynamical scaling considerations (Section 2.8). Although it yields a reasonable overall fit for all field and wave-tank data, an exponent of  $-0.4$  is a better approximation to the average slope of our  $\alpha$  distribution.

The peak shape parameters  $\gamma$ ,  $\sigma_a$  and  $\sigma_b$  (Fig. 2.8) are more highly scattered than the scale parameters. Since they characterize the properties of a rather narrow spectral peak, some variability is to be expected from the statistical indeterminacy associated with the spectral measurement. However, this accounts for an r.m.s. relative variability of only about 20 %, which is considerably smaller than observed. Attempts were made to reduce the variability by subdividing the data with respect to additional parameters such as the air-sea temperature difference, currents, and the direction of the wind relative to the profile. No reduction of the scatter was achieved. However, local non-stationaries (defined by the time derivative estimated from three neighboring spectra) above a certain threshold were found to account for some of the variability, and Figs. 2.6, 2.7 and 2.8 accordingly contain only generation cases for which the non-stationarity was below a critical value, determined empirically by the inequality  $\frac{\partial}{\partial t} < v_m \frac{\partial}{\partial x}$  where  $v_m$  represents the group velocity of the waves at the spectral peak.

It appears that the residual scatter of our data in Figs. 2.6, 2.7 and 2.8 is geophysically real and cannot be accounted for in a simple manner by additional parameters characterizing the mean generation conditions. The analysis of individual generation cases discussed in Section 2.7 shows that a variability of the same order occurs within each generation case, suggesting that it may be associated with small scale inhomogeneities of the wind field (Section 2.9).

A clear trend of the shape parameters with fetch is not discernible within the scatter of the data, although there is some indication of  $\gamma$  peaking to a maximum around  $\bar{x} = 10^3$ . Accordingly, we shall assume as first approximation that the spectral shape is self-preserving and consider in much of the following a mean spectrum defined by the parameters\*\*

$$\gamma = 3.3, \quad \sigma_a = 0.07, \quad \sigma_b = 0.09. \quad (2.4.5)$$

\* It could be surmised that the fetch dependence of our  $\alpha$  data is induced by the fetch dependence of our averaging band, defined with respect to  $f_m$  – e.g. due to an exponent in the spectral power law which differs slightly from  $-5$ . This is not the case. Essentially the same results were obtained using fixed frequency bands.

\*\* A more detailed dynamical analysis suggests that this is not strictly tenable, cf. Section 2.9.



Fig. 2.9 shows a comparison of the normalized shape functions

$$\varphi\left(\frac{f}{f_m}\right) = (2\pi)^4 \alpha^{-1} g^{-2} f^5 E(f) \quad (2.4.6)$$

for this spectrum, the Pierson-Moskowitz spectrum and a schematic empirical spectrum proposed by S. A. Kitaigorodskii [1962]. The form corresponding to (2.4.5) is qualitatively very similar to the shape functions observed by T. P. Barnett and A. J. Sutherland [1968] and H. Mitsuyasu [1968a, 1969].

To conclude our summary of empirical fetch relationships, Fig. 2.10 shows a plot of the nondimensional energy  $\tilde{\mathcal{E}} = \mathcal{E} \times g^2 U_{10}^{-4}$ , where  $\mathcal{E} = \int E(f) df$ . The data is well represented by the linear relationship

$$\tilde{\mathcal{E}} = 1.6 \times 10^{-7} \tilde{x}. \quad (2.4.7)$$

For a self-similar spectrum,  $\tilde{\mathcal{E}} \sim \alpha f_m^{-4}$ , so that the exponents  $n_f$ ,  $n_\alpha$  and  $n_{\tilde{\mathcal{E}}}$  in the power laws for  $f_m$ ,  $\alpha$  and  $\tilde{\mathcal{E}}$  should satisfy the relation

$$4n_f - n_\alpha + n_{\tilde{\mathcal{E}}} = 0. \quad (2.4.8)$$

The values given in equations (2.4.3), (2.4.4) and (2.4.7) yield

$$4(-0.33) - (-0.22) + 1 = -0.1 \quad (2.4.9)$$

which lies within the error of about  $\pm 0.2$  estimated from the error bands of the individual exponents.

## 2.5. The Directional Distribution

The majority of investigated generation cases occurred during the latter part of July 1969, when the directional data of all but one of the pitch-roll buoys was questionable, or during the period August 1–August 15, 1969, when only the innermost section of the profile (without pitch-roll buoys) was in operation. Unfortunately, the directional data from the single pitch-roll buoy and the linear array at Station 4 did not encompass a sufficiently wide range of dimensionless fetch values  $\tilde{x}$  to permit a systematic investigation of the fetch dependence of directional parameters. Thus we have assumed – in analogy with the similar result found for the frequency spectra – that the scaled directional distributions  $s(\theta, f/f_m)$  are independent of fetch.

Averaging over all ideal generation cases, the linear array yields a mean beam width for frequencies near the spectral peak of  $\theta'_s \approx 19^\circ \pm 5^\circ$ . This corresponds to an equivalent pitch-roll beam width of  $\theta_s \approx 27^\circ \pm 8^\circ$  ( $f_m \approx 0.4$  Hz) which is reasonably close to the value  $31^\circ$  for a  $\cos^2 \theta$  distribution. At frequencies appreciably higher than the peak frequency, the linear array was normally too strongly aliased to be interpreted reliably. The pitch-roll buoy at Station 10 also yielded beam widths  $\theta_s \approx 30^\circ$  for  $f = f_m$ .

Examples of the dependence of beam width on frequencies greater than  $f_m$  is shown in Fig. 2.11. Data from both the functioning and questionable pitch-roll instruments are included in the figure. The malfunctioning instruments were characterized by random variations in the mean direction from one recording to another. Rather surprisingly, however, the mean square angular spread for all instruments were found to be reasonably consistent. A possible explanation is that the compass was sticking and the orientation of the buoy remained relatively constant during any given recording. This interpretation finds some support through the fact that for the same wave conditions the frequency dependence of the mean angle  $\theta_m$  was generally similar for all pitch-roll instruments except for random shifts of the zero reference angle. We infer from Fig. 2.11 that the directional distribution may be modeled by  $\cos^2 \theta$  ( $\theta_s \approx 30^\circ$ ) near the peak of the spectrum – in accordance with the linear array data – changing gradually to an approximately uniform half-plane radiation ( $\theta_s \approx 43^\circ$ ) at high frequencies,  $f > 2$  to  $3 f_m$ .

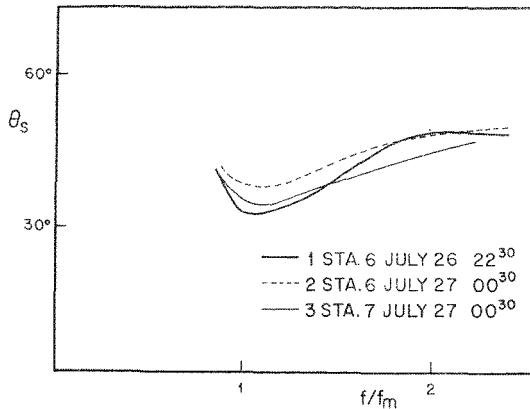


Fig. 2.11. Typical frequency dependence of the root-mean-square directional spread  $\theta_s$  measured for fetch limited spectra

Since most of the wave energy is concentrated near the peak we have assumed for simplicity a frequency independent  $\cos^2 \theta$  spreading function in computing net source functions, nonlinear transfer rates, etc. It was found that the principal conclusions regarding the energy balance were in fact rather insensitive to the precise form assumed for the spreading function.

## 2.6. The Mean Source Function

The empirical average dependences (2.4.3), (2.4.4) of the spectral parameters  $\bar{f}_m$  and  $\alpha$  on fetch  $\bar{x} = g\bar{x}/U_{10}^2$ , together with the (constant) average shape parameters (2.4.5), define a mean one-dimensional spectrum at each  $\bar{x}$ , from which a mean one-dimensional source function can be computed through equation (2.1.2),

$$S\left(\frac{f}{f_m}, \bar{x}\right) = \frac{\bar{v}g}{U_{10}^2} \left( \frac{\partial E}{\partial \alpha} \frac{d\alpha}{d\bar{x}} + \frac{\partial E}{\partial \bar{f}_m} \cdot \frac{d\bar{f}_m}{d\bar{x}} \right). \quad (2.6.1)$$

Fig. 2.12 shows the mean JONSWAP spectrum and the associated mean source function  $S$  (a  $\cos^2 \theta$  spreading factor was assumed in evaluating  $\bar{v}$ ). The plus-minus distribution of the source function is associated with the transition of the spectral peak towards lower frequencies, the positive lobe corresponding to the rapidly growing waves on the forward face of the spectrum and the negative lobe to the attenuation of the waves on the rear slope of the peak as they approach equilibrium (the overshoot effect – cf. also Fig. 2.5).

Several authors have pointed out that the form of the source function, in particular the overshoot effect, is difficult to explain in terms of a linear (or any frequency decoupled) theory, and have suggested that cross-spectral energy transfer due to resonant wave-wave interactions, white-capping or some other form of nonlinear coupling may be significant (T. P. Barnett and A. J. Sutherland [1968], B. V. Korvin-Kroukovsky [1967], H. Mitsuyasu [1969], A. J. Sutherland [1968]). Our computations of the nonlinear energy transfer due to resonant wave-wave interactions, also shown in Fig. 2.12, indicate that this process can indeed account for the principal features of the observed source function, including the plus-minus signature, the major part of the wave growth on the forward face of the peak, and the overshoot phenomenon. We attribute the difference between the observed source function  $S$  and the nonlinear energy transfer  $S_{n1}$  to the positive energy input from the atmosphere, which is discussed further in the context of the overall energy balance of the spectrum in Section 2.9.

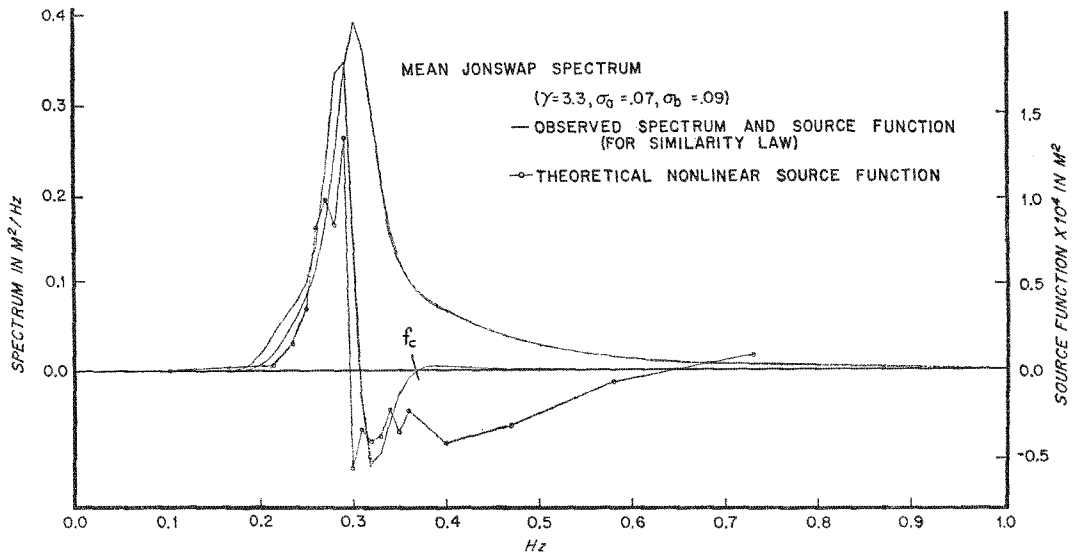


Fig. 2.12. Mean JONSWAP spectrum, source function  $S$  computed from power laws (2.4.3), (2.4.4) using (2.7.1), and computed nonlinear energy transfer  $S_{nl}$

The spectra and source functions shown in Fig. 2.12 correspond to particular values of the fetch  $x$  and windspeed  $U_{10}$ . In general the ratio of the source functions  $S$  and  $S_{nl}$  may be expected to vary with the nondimensional fetch  $\tilde{x}$ . However, under certain scaling conditions – which we return to in Section 2.9 – the ratio is approximately independent of  $\tilde{x}$ . From the Boltzmann-integral expression for the nonlinear energy transfer (K. Hasselmann [1962, 1963a]) – namely

$$\frac{\partial N_4}{\partial t} = \int T (N_1 N_2 N_3 + N_1 N_2 N_4 - N_1 N_3 N_4 - N_2 N_3 N_4) \times \\ \times \delta(\omega_1 + \omega_2 - \omega_3 - \omega_4) dk_1 dk_2$$

where  $k_4 = k_1 + k_2 - k_3$ ,  $N_j = N(k_j) = \hat{F}(k_j)/\omega_j$ ,  $\omega_j = \sqrt{gk_j}$ ,  $\hat{F}(k)$  is the two dimensional wave spectrum with respect to wavenumber, and the transfer coefficient  $T$  is a quadratic homogeneous function of the four wavenumbers  $k_1, \dots, k_4$  – it follows that for a family of self-similar spectra of the form  $E'(f, \theta) = \alpha g^2 (2\pi)^{-4} f^{-5} \psi'(f/f_m, \theta)$  the nonlinear transfer  $S_{nl}$  scales with respect to  $\alpha$  and  $f_m$  according to

$$S_{nl} = U_{10}^4 g^{-2} \alpha^3 f_m^{-4} \psi(f/f_m) \quad (2.6.2)$$

where  $\psi(f/f_m)$  is a dimensionless function depending on the shape  $\psi'$  of the spectrum. To compare  $S_{nl}$  and  $S$  it is useful to consider integral momentum transfer properties of the functions, which are relatively insensitive to the shape of the spectrum (and will be related later to the momentum transfer across the air-sea interface). Since wave-wave interactions

are conservative, the net momentum transfer  $\rho_w g \int \frac{\bar{k}_x}{2\pi f} S_{nl} df$  is zero. ( $\bar{k}_x$  represents the average

value of  $k_x$  integrated over the normalized directional distribution of  $S_{nl}$ .) However, the integral over any one of the three lobes of the distribution in Fig. 2.12 is non zero, and is of the general form, say for the third lobe (i.e. the positive lobe at high frequencies),

$$\tau_{\text{hf}} = \varrho_w g \int_{f_c}^{\infty} \frac{\bar{k}_x}{2\pi f} S_{\text{nl}} df = c \varrho_w U_{10}^2 \alpha^3 \bar{f}_m^{-2} \quad (2.6.3)$$

where  $c$  is a dimensionless constant dependent only on the shape of the spectrum and  $f_c$  represents the lower limit of the lobe (cf. Fig. 2.12). On the other hand, according to (2.1.1) the net momentum transfer  $\varrho_w g \int_0^{\infty} \frac{\bar{k}}{2\pi f} S df$  is equal to the momentum advected away by the wave field,

$$\tau_{\text{ad}} = \varrho_w g \int_0^{\infty} \frac{k_x v_x}{2\pi f} \frac{dF}{dx} df d\theta = \frac{3}{8} \varrho_w g \frac{d\mathcal{E}}{dx}. \quad (2.6.4)$$

The factor  $3/8$  follows from the assumption of a  $\cos^2 \theta$  spreading factor. Empirically,  $\mathcal{E} \sim \bar{x}^{1 \pm 0.1}$  from (2.4.7),  $\bar{f}_m \sim \bar{x}^{-0.33 \pm 0.03}$  from (2.4.3), so that the ratio  $\tau_{\text{hf}}/\tau_{\text{ad}}$  remains constant if  $\alpha \sim \bar{x}^{-0.22 \pm 0.04}$  as given by (2.4.4), in accordance with the overall distribution of  $\alpha$  in Fig. 2.7. We note that these exponents correspond not only to a constant ratio  $\tau_{\text{hf}}/\tau_{\text{ad}}$ , but also to fetch independent equivalent friction coefficients  $c_{\text{hf}} = \tau_{\text{hf}}/\varrho_a U_{10}^2$ ,  $c_{\text{ad}} = \tau_{\text{ad}}/\varrho_a U_{10}^2$ .

The ratio  $\tau_{\text{hf}}/\tau_{\text{ad}}$  is rather insensitive to the angular distribution. For example, a  $\cos^4 \theta$  rather than a  $\cos^2 \theta$  spreading factor increases  $\tau_{\text{ad}}$  by about 10 %, whereas the computations of  $S_{\text{nl}}$  yield about 15 % higher values for  $\tau_{\text{nl}}$ . The uncertainties associated with the angular distribution are generally smaller than the variability introduced through the cubic dependence of  $S_{\text{nl}}$  (eq. (2.6.2)) on the rather scattered parameter  $\alpha$ . However, a  $\cos^2 \theta$  distribution near the peak is consistent with computations of the two-dimensional source function  $S_{\text{nl}}$ , which has approximately this angular distribution in the low-frequency positive lobe (cf. Fig. 2.13). A narrower angular beam is found to become broadened by the nonlinear transfer near the peak. Fig. 2.13 also indicates that the nonlinear transfer tends to broaden the angular distribution at higher frequencies more than at low frequencies, in accordance with Fig. 2.11.

As pointed out in the previous section, the power laws (2.4.3), (2.4.4) and (2.4.7) are almost but not strictly compatible with a self-similar spectrum, since they violate (although by less than the error limits) the condition (2.4.8)\*. We return to the question of self-similarity and scaling in connection with the overall momentum and energy balance of the spectrum

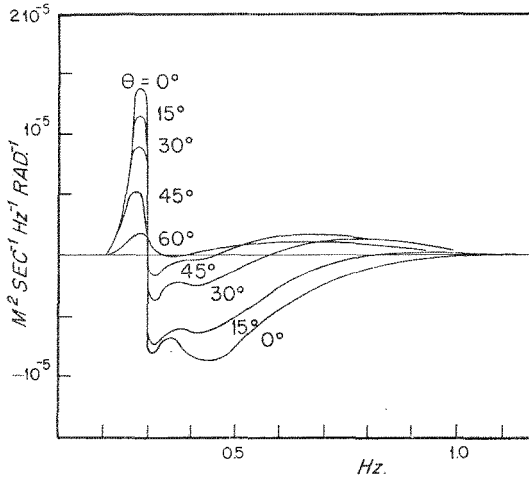


Fig. 2.13. Two-dimensional nonlinear source function  $S_{\text{nl}}^{(2)}(f, \theta)$  computed for the mean JONSWAP spectrum

\* Strict self-similarity together with a constant ratio  $\tau_{\text{hf}}/\tau_{\text{ad}}$  requires  $\bar{f}_m \sim \bar{x}^{-0.3}$ ,  $\alpha \sim \bar{x}^{-0.2}$ ,  $\mathcal{E} \sim \bar{x}$ .

in Section 2.9. We simply remark here that the spectral scales vary in such a manner that to first order both the source function ratio  $S:S_{n1}$  and the nonlinear momentum transfer  $\tau_{nf}$  to high frequencies remain constant over a five-decade range of fetches. This is apparently not coincidental but a consequence of the nonlinear interactions.

## 2.7. Analysis of Individual Generation Cases

To establish the representativeness of the source function derived from the mean fetch dependence of the set of all scaled spectra, five generation cases were investigated independently. The examples were chosen arbitrarily from the various periods of "ideal" generation conditions.

In each case the spectral parameters  $(f_m, \alpha, \gamma, \sigma_a, \sigma_b) = (a_1, a_2, a_3, a_4, a_5)$  were evaluated for each spectrum and plotted as functions of fetch  $x$  and time  $t$ . From the spatial and time derivatives of the parameters obtained graphically from these plots the source function was then determined using the relation

$$S = \frac{\partial E}{\partial t} + \bar{v} \frac{\partial E}{\partial x} = \frac{\partial E}{\partial a_j} \left( \frac{\partial a_j}{\partial t} + \bar{v} \frac{\partial a_j}{\partial x} \right) \quad (2.7.1)$$

for the parametrised spectrum. This technique was regarded as more accurate than straightforward estimates of the spatial and time derivatives from finite differences of the measured spectra. On account of the peaked form of the spectrum, the spatial and time resolution of the spectral field was only marginally adequate to trace the rapid growth of a given frequency component during its brief period on the forward face of the spectrum. Thus if the finite difference method is applied in the usual manner to estimate

$$\frac{\partial F}{\partial t} \approx \frac{\Delta F}{\Delta t}, \quad \frac{\partial F}{\partial x} \approx \frac{\Delta F}{\Delta x}$$

at a fixed frequency, the source function appears strongly smoothed with respect to frequency. This difficulty is avoided by transforming to a new representation in terms of parameters  $a_1 \dots a_n$  which vary smoothly with respect to space and time. A comparison of the source functions computed by both techniques is given in Fig. 2.19 (generation case 4).

A listing of the relevant parameters of all cases studied (including three other JONSWAP spectra and the Pierson-Moskowitz spectrum) is given in Table 2. The weather situation for all generation cases was very similar and is illustrated by the two examples in Figs. 2.14 and 2.15. More detailed histories of the winds measured along the profile, together with the times and positions of the wave measurements, are shown for the individual generation cases in the appendix, Fig. 2A.1. The fetch and time behaviour of the spectral parameters are presented in Figs. 2A.2–2A.11 of the appendix. In all cases, the  $\tilde{x}$  dependence of the scale parameters could be adequately represented by the power laws  $\tilde{f} \sim \tilde{x}^{-0.3}$ ,  $\alpha \sim \tilde{x}^{-0.4}$ . The shape parameters were too strongly scattered to define derivatives, so that these were taken to be zero, as in the average case. Figures 2.16–2.20 show the source functions,  $S$  evaluated for each case at the positions indicated in Figs. 2A.1–2A.11 using equation (2.7.1), and the computed nonlinear transfer rate  $S_{n1}$ .

Although both the details and relative magnitudes of  $S$  and  $S_{n1}$  show considerable variability, the results tend to confirm the average source functions of Fig. 2.12. The variability appears consistent with the inaccuracies entailed by the experimental differentiations and the sensitivity of the cubic wave-wave interaction integrals with respect to the wave spectrum. We note that the scatter of the spectral shape parameters is characterized by rather small spatial and time scales and is comparable to the scatter seen in the plots for the complete ensemble of generation cases (Fig. 2.8) – suggesting that in both cases the variability is caused by the gustiness of the wind.

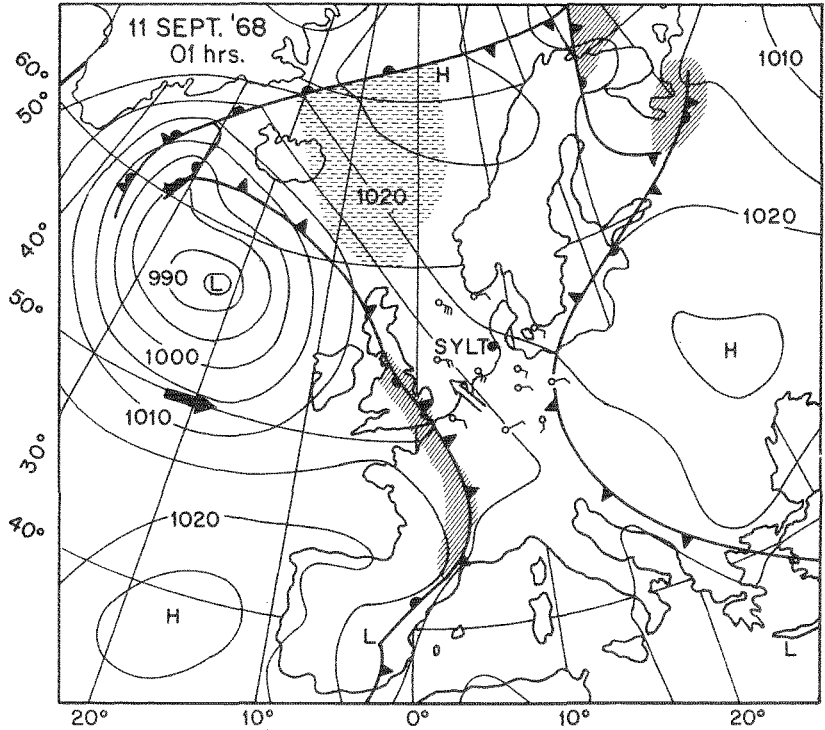


Fig. 2.14. Weather map for generation case 1

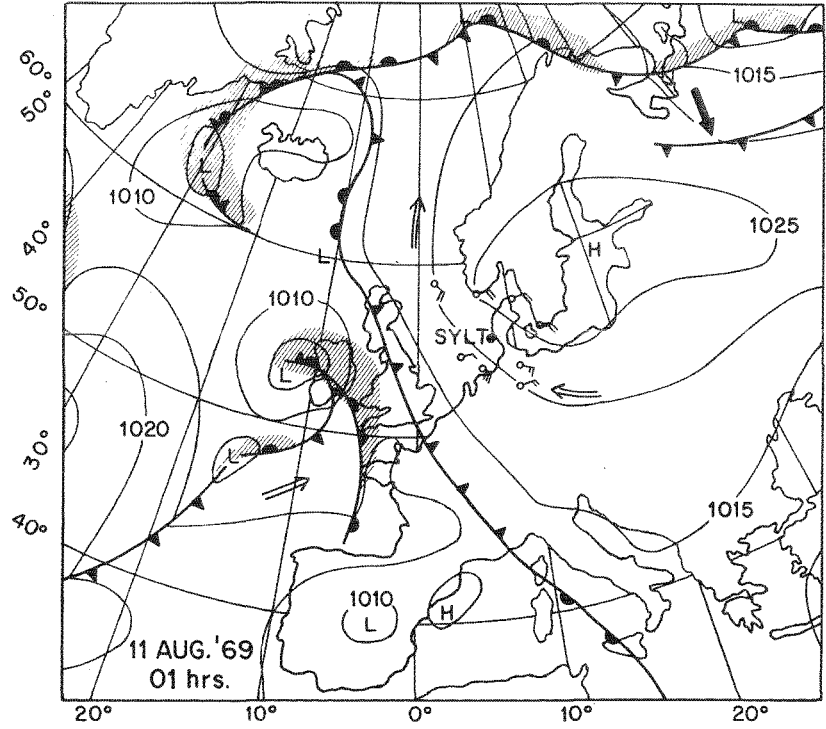
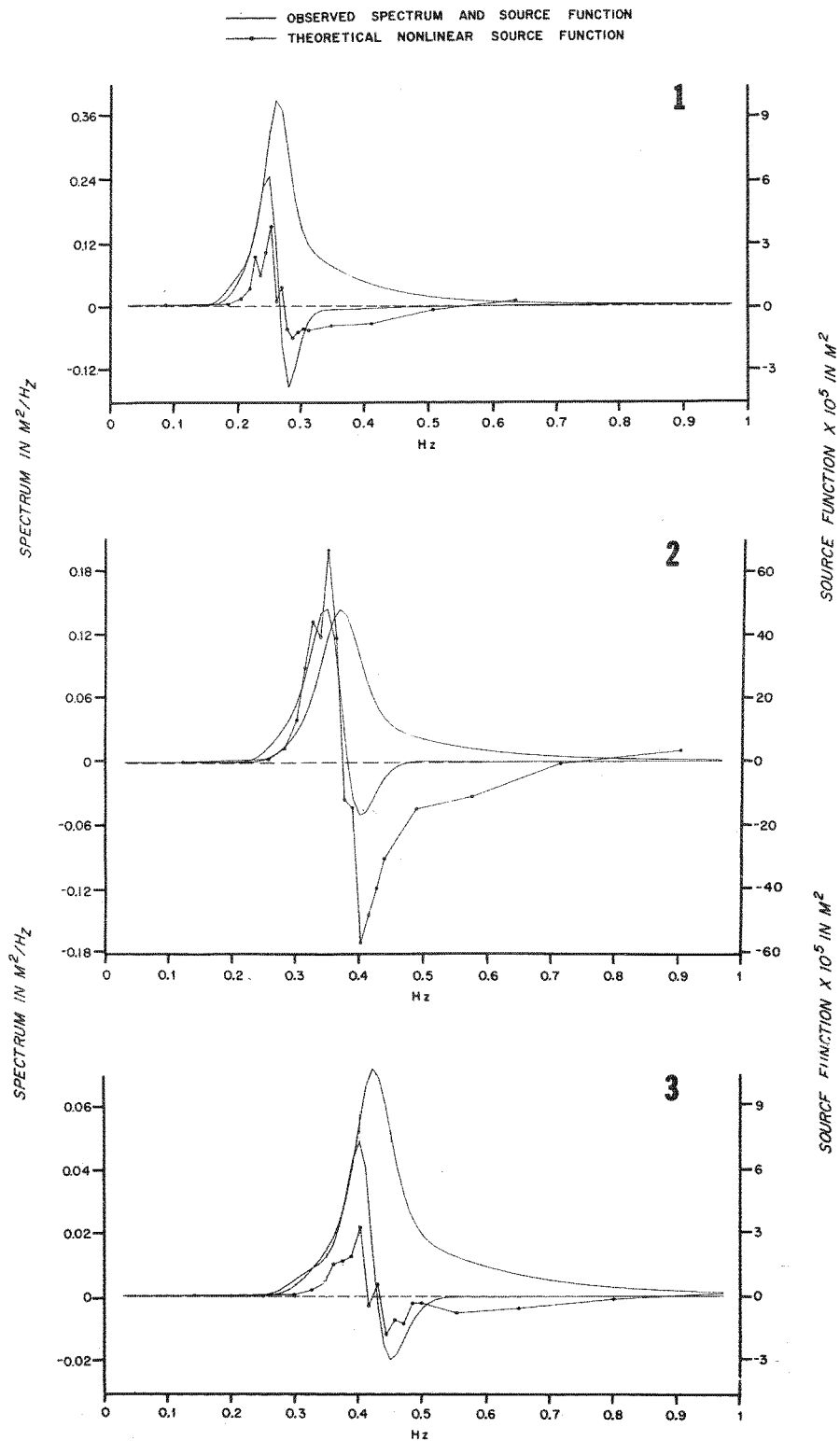


Fig. 2.15. Weather map for generation case 5



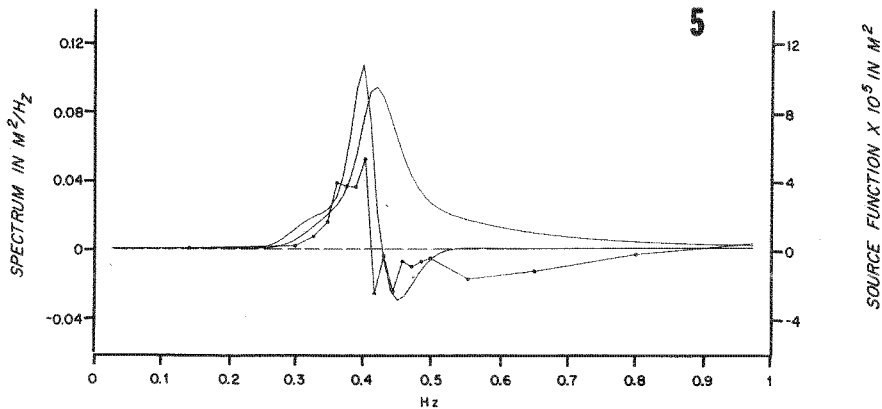
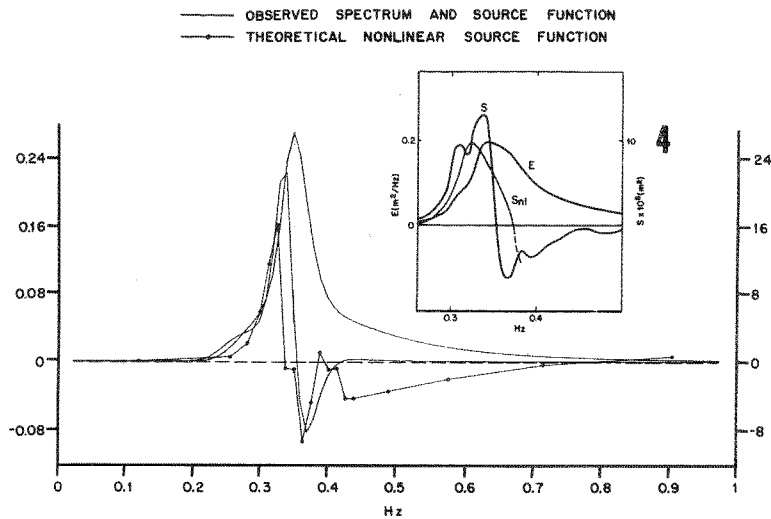


Fig. 2.16. Spectrum, empirical source function and computed nonlinear energy transfer for generation case 1

Fig. 2.17. Same as Fig. 2.16 for generation case 2

Fig. 2.18. Same as Fig. 2.16 for generation case 3

Fig. 2.19. Same as Fig. 2.16 for generation case 4. The inset shows the (less accurate) estimate of the source function obtained from direct differences of the measured spectra. The spectrum represents the average of the three spectra used in the finite differences; the nonlinear transfer rate was computed for this mean spectrum

Fig. 2.20. Same as Fig. 2.16 for generation case 5



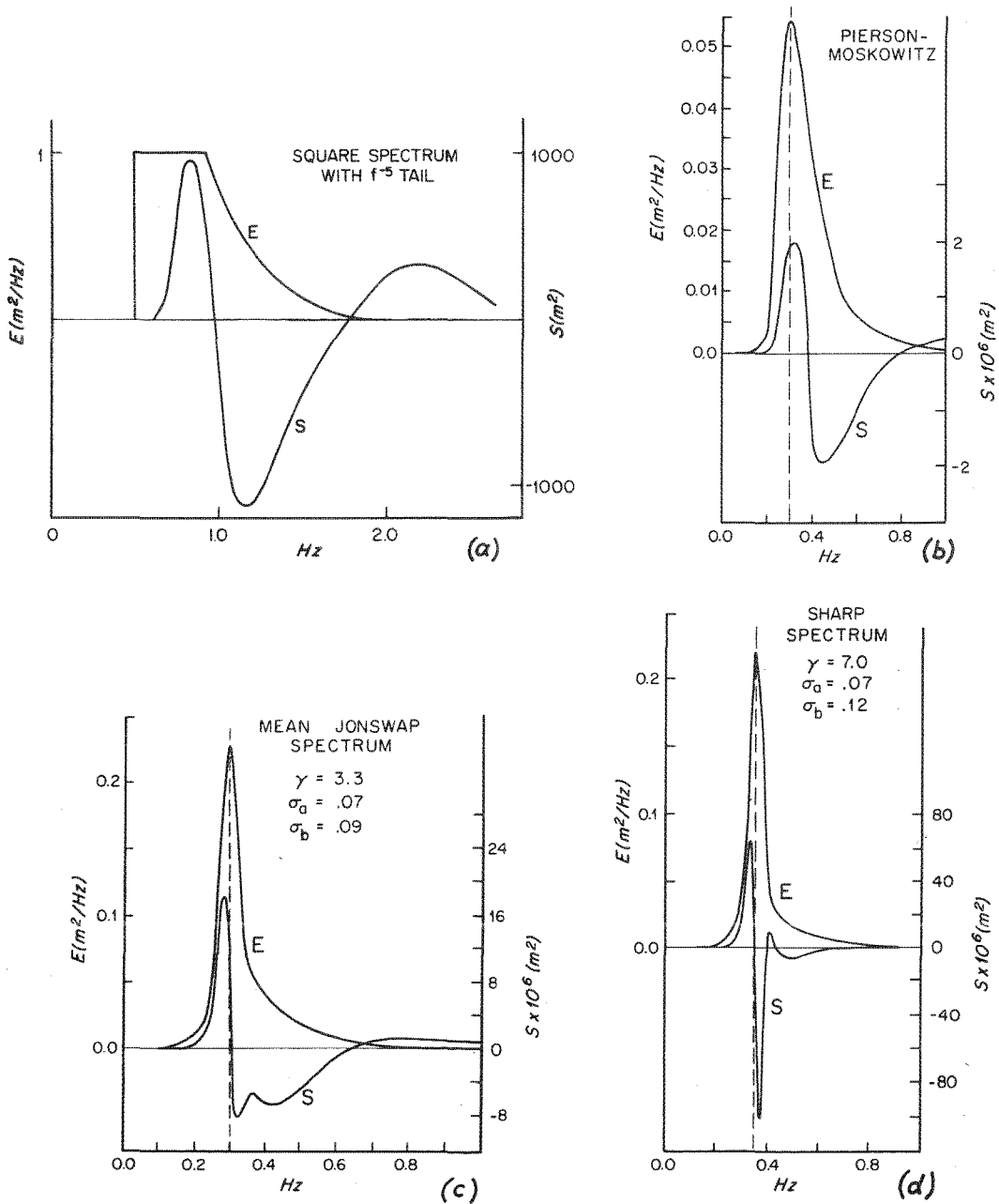


Table 2  
Generation Cases

Case	Time	Date	Fetch	$U_{10}$	$\alpha \cdot 10^3$	$f_m$	$\gamma$	$\sigma_a \cdot 10^3$	$\sigma_b \cdot 10^3$	$\bar{x} \cdot 10^{-3}$	$\bar{f}_m$	$\alpha^p \cdot 10^3$ (1)	$f_m^p$ (1)	$\frac{\partial \alpha}{\partial t} / \frac{\partial \alpha}{\partial x} v_m$	$\frac{\partial f_m}{\partial t} / \frac{\partial f_m}{\partial x} v_m$	$c_{ad} \cdot 10^3$	$c_{hf} \cdot 10^3$	$c_w^{min} = 10^3 \cdot c_w^{min2}$ (2)
1	12 <sup>00</sup>	15 Sep. 1968	km 37	m/s 7.0	9.1	Hz 0.263	3.06	85	83	7.4	0.188	10.6	0.187	0.92	0.36	0.046	0.08	0.13
2	15 <sup>30</sup>	26 Jul. 1969	11	8.8	15.6	0.371	3.67	104	104	1.39	0.333	15.4	0.325	$0 \pm 0.05$	- 0.24	0.045	0.15	0.20
3	11 <sup>30</sup>	1 Aug. 1969	5.25	9.0	15.5	0.421	3.42	72	92	0.636	0.386	18.3	0.421	0.16	0.18	0.052	0.09	0.14
4	19 <sup>30</sup>	1 Aug. 1969	8	10.7	20.4	0.349	3.86	57	77	0.685	0.381	18.0	0.411	- 0.27	$0 \pm 0.02$	0.072	0.22	0.29
5	15 <sup>30</sup>	10 Aug. 1969	5.25	9.2	20.5	0.416	3.24	60	100	0.608	0.390	18.5	0.428	0.12	0.16	0.072	0.18	0.25
Mean JONSWAP							3.3	70	90					0	0	0.050 <sup>(3)</sup>	0.13	0.18
Sharp JONSWAP							4.2	50	70								0.12	
Very sharp JONSWAP							7.0	68	123									
Pierson- Moskowitz					8.1		1			> 20- 50	0.14					0	0.09	0.09

(1)  $\alpha^p, f_m^p$  as inferred from power laws (2.4.3), (2.4.4) for given  $\bar{x} = gx/U_{10}$ .

(2)  $c_w^{min} = c_{ad} + c_{hf}$ ;  $\tau_w^{min}/\tau = c_w^{min}/c_{10} = c_w^{min} \cdot 10^3$  for  $c_{10} = 10^{-3}$ .

(3) From equation (2.4.7).

## 2.8. Origin of the Spectral Peak

It appears from the preceeding two sections that nonlinear wave-wave interactions can account for the observed shift of the spectral peak towards lower frequencies at about the rate observed. However, the evolution of the peak and its persistence throughout the development of the wave field still remain to be explained. To investigate this question, nonlinear transfer rates were computed for a number of spectral shapes with broader or narrower distributions than the mean JONSWAP spectrum. Fig. 2.21 shows the nonlinear transfer rates computed for a sequence of spectra with successively sharper peaks. A  $\cos^2 \theta$  spreading factor was assumed in all cases.

Panel a gives an example of a fairly white spectrum with a low frequency cut-off. In all such cases it is found that the nonlinear energy transfer tends to enhance the energy level towards the low frequency end of the distribution, causing a peak to develop. The evolution of the peak continues up to and beyond the already rather pronounced form shown in the second panel (a Pierson-Moskowitz spectrum). This is evidenced by the position of the positive lobe of the source function directly beneath the spectral peak. However, as the peak continues to sharpen, the positive lobe of the nonlinear energy transfer gradually moves towards the forward face of the spectrum, until the spectrum reaches a state (approximately given by the mean JONSWAP spectrum) where the peak no longer grows but shifts towards lower frequencies without change of shape (panel c). For a still more pronounced spike, the nonlinear source function finally develops two positive side lobes on either side of a strong negative lobe directly beneath the peak, and the distribution tends to flatten again (panel d).

Hence it appears that the evolution of a rather sharp spectral peak of approximately the form observed can be explained as a self-stabilizing property of the nonlinear interactions. The superposition of an additional atmospheric energy input with a smooth frequency distribution, as discussed in the following section, does not appreciably affect the form of this self-adjusting spectral distribution.

We have not been able to find a simple physical explanation for the particular forms of the nonlinear source functions shown in Fig. 2.21. Generally, simultaneous conservation of two independent scalar quantities, in this case energy and action, requires a plus-minus-plus distribution of the one-dimensional nonlinear energy transfer (K. Hasselmann [1963a] – this is well known also for the case of two-dimensional turbulence, where the nonlinear interactions conserve both energy and mean square vorticity). However, the position of the first positive lobe directly beneath the spectral maximum for moderately peaked distributions is rather unexpected, as it is known from general entropy theorems (in the present context cf. K. Hasselmann [1963a] and [1966]) that wave-wave interactions change the spectrum irreversibly in the direction of a uniform energy distribution in wavenumber space (corresponding to an  $f^3$  one-dimensional frequency spectrum). Intuitively, we should therefore expect a negative rather than positive lobe of the source function at the position of the peak. However, this is the case only for extremely peaked spectra. Numerical investigations of the transfer integral indicate that the form of the transfer function near the peak is dominated by interactions in which all components of the interacting quadruplets lie in the vicinity of the spectral peak, and that the high-frequency range of the spectrum is of only minor significance for the evolution and stability of the peak (cf. also K. Hasselmann [1963b]). A more detailed explanation of the behaviour of the computed nonlinear transfer distributions requires investigation of the rather complex algebraic structure of the coupling coefficients and resonant interaction surfaces.

A complete compilation of the nonlinear transfer computations carried out for this study can be found in W. Sell and K. Hasselmann [1972]. Several improvements over the numerical method used in earlier computations (K. Hasselmann [1963b]) were introduced, including a symmetrical treatment of the wave "collision" processes which yielded accurate overall conservation of energy, momentum and action, and furthermore provided consistency checks through three independent estimates of the transfer rates. Typical computation times on a CDC 6600 (NCAR) were 30 minutes per spectrum. The results were checked against

independent computations using a different numerical technique by D. Cartwright (unpublished); the overall agreement of the smoothed distributions lay within a few percent (cf. W. Sell and K. Hasselmann [1972]). The fine scale variability of the nonlinear computations presented in Sections 2.6–2.8 is associated with the finite mesh size used for the integration. Reduction of the mesh size by a factor of two removes most of the variability, but would require an eight fold increase in computing time.

## 2.9. The Energy and Momentum Balance of the Spectrum

Having gained some insight into the role of nonlinear interactions in controlling the shape of the spectrum and its evolution from short to long waves, we may attempt to construct a picture of the overall energy balance of the spectrum. Unavoidably, we shall be handicapped herein by incomplete knowledge of the remaining processes governing the spectral energy balance – in particular the input by the wind and the dissipative mechanisms. Thus to some extent our conclusions will remain ambiguous, and inequality relationships will normally take the place of equations. However, in certain cases two-sided inequalities can be narrowed down to yield quantitative predictions.

The net source function  $S$  in the energy balance equation may be divided generally into three terms,

$$S = S_{in} + S_{nl} + S_{ds}$$

representing, respectively, the energy input  $S_{in}$  from the atmosphere, the nonlinear cross-spectral transfer  $S_{nl}$  due to conservative wave-wave interactions, and a dissipation term  $S_{ds}$ . We include in  $S_{ds}$  not only pure energy losses but also any cross-spectral energy transfer which may accompany nonlinear dissipative processes such as white-capping, for example in conjunction with the attenuation of long waves by damped short waves, cf. O. M. Phillips [1963], M. S. Longuet-Higgins and R. W. Stewart [1964], K. Hasselmann [1971].

From the measured net source function  $S$  and the computed nonlinear transfer  $S_{nl}$  we may infer the value of the sum  $S_{in} + S_{ds} = S - S_{nl}$ , but can say nothing about the partition of the sum without further information about  $S_{in}$  or  $S_{ds}$ . Assuming for the moment that the dissipation is negligible in the main part of the spectrum, the source functions  $S$  and  $S_{nl}$  as computed for the mean JONSWAP spectrum in Fig. 2.12 imply a net energy balance of the form indicated schematically in Fig. 2.22. The energy input has approximately the same distribution as the spectrum (in accordance with the linear dependence on the spectrum predicted by most wave generation theories) and is balanced by the negative nonlinear transfer away from the main part of the spectrum to lower and higher frequencies. At low frequencies the positive nonlinear energy transfer is removed by advection, whereas at high frequencies some form of dissipation needs to be invoked to balance the positive contributions from both the nonlinear transfer and the atmospheric input.

It is of interest to compute the minimal momentum transfer  $\tau_w^{\min}$  from the atmosphere to the wave field needed to maintain this “minimum-dissipation” spectral balance. First, the atmosphere must supply the momentum

$$\tau_{ad} = \rho_w g \int S \frac{k}{2\pi f} df$$

advected away by the wave field. In Section 2.6 this was shown to be given by  $3/8 \rho_w g d\mathcal{E}/dx$  (eq. (2.6.4)), or substituting the empirical linear fetch dependence (2.4.7) for the energy  $\mathcal{E}$ ,

$$\tau_{ad} = c_{ad} \rho_a U_{10}^2 \quad (2.9.1)$$

where

$$c_{ad} = \frac{3}{8} \frac{\rho_w}{\rho_a} 1.6 \times 10^{-7} = 0.05 \times 10^{-3}.$$

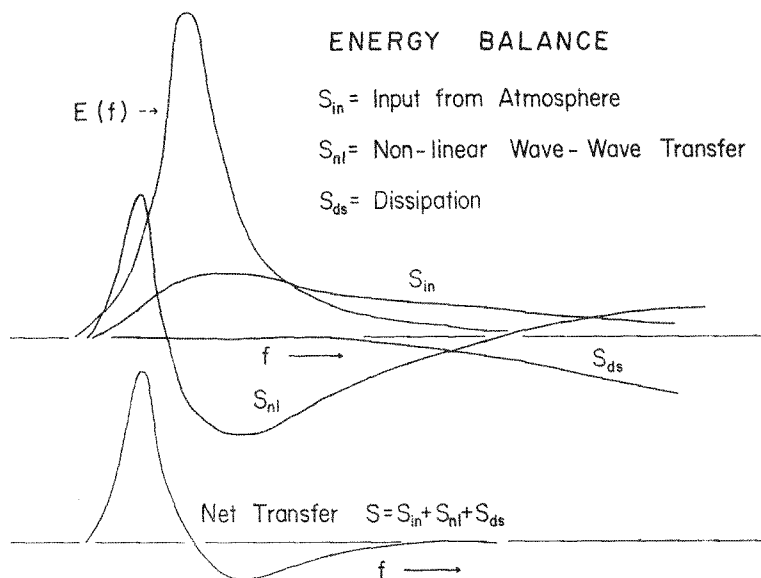


Fig. 2.22. Schematic energy balance for the case of negligible dissipation in the main part of the spectrum

Secondly, the momentum  $\tau_{hf}$  transferred to high frequencies in the positive lobe of the nonlinear source function, which is passed on to currents through dissipation, must be replaced by an equal atmospheric input which enters the wave field in the central region of the spectrum. This contribution was shown in Section 2.6 to be of the form (eq. (2.6.3))  $\tau_{hf} = c_{hf} \alpha^3 \bar{f}_m^{-2} U_{10}^2$ , which reduces in the case of the empirical power laws (2.4.3) and (2.4.4) to

$$\tau_{hf} = c_{hf} \varrho_a U_{10}^2 \quad (2.9.2)$$

where

$$c_{hf} = c_{\varrho_w} / \varrho_a (0.076)^3 (3.5)^{-2}. \quad (2.9.3)$$

Computations for the mean JONSWAP spectrum yield  $c_{hf} = 0.13 \times 10^{-3}$ . Summing (2.9.1) and (2.9.2) we obtain for the minimal momentum transfer from the atmosphere to the wave field

$$\tau_w^{\min} = \tau_{ad} + \tau_{hf} = c_w^{\min} \varrho_a U_{10}^2$$

with

$$c_w^{\min} = c_{ad} + c_{hf} \approx 0.2 \times 10^{-3}. \quad (2.9.4)$$

Comparing this value with the drag coefficient  $c_{10} \approx 10^{-3}$  for the total momentum transfer  $\tau$  across the air-sea interface, we conclude that at least 20 % of the total sea surface drag is induced by the wave field. We note that this represents a conservative lower limit even if dissipation in the central region of the spectrum is discounted. It assumes that the atmospheric input is identically zero for frequencies in the high-frequency positive lobe of the nonlinear source function, and conversely that the dissipation is identically zero outside the lobe. A continuous transition of both source functions  $S_{in}$  and  $S_{ds}$  across the lobe boundary, which appears more probable (cf. Fig. 2.22), would increase the estimate of the net atmospheric input. Assuming an arbitrary dissipation, rather than the minimal dissipation compatible with  $S$  and  $S_{nl}$ , the wave induced drag coefficient  $c_w$  may take any value between  $c_w^{\min}$  and the theoretical maximum  $c_{10}$ .

The calculations for the coefficients  $c_{ad}$ ,  $c_{hf}$  and  $c_w^{\min}$  apply for all fetches for which the power laws (2.4.3), (2.4.4) and (2.4.7) remain valid and the spectrum retains the same shape.

The latter condition is not strictly satisfied (cf. Section 2.4) but is not critical for the estimates. It enters only in the computations for  $c_{\text{hf}}$  through the shape dependence of the coefficient  $c$  in eq. (2.9.3). For the six spectra listed in Table 1,  $c_{\text{hf}}$  varies by only a few percent.

However, the calculations do depend critically on the power laws of the spectral scale parameters. In view of the cubic dependence of  $S_{\text{nl}}$  and  $\tau_{\text{hf}}$  on  $\alpha$ , the systematic deviations of our  $\alpha$  data (Fig. 2.7) from the mean line (2.4.4) drawn through the overall data cannot be ignored. In Fig. 2.7, dotted lines have been drawn parallel to the mean  $-\alpha$  line to delineate the theoretical upper limit  $c_{\text{hf}} = c_{10} - c_{\text{ad}} = 0.95 c_{10}$ , which is five times greater than mean value  $c_{\text{hf}} = 0.18 c_{10}$ , and a corresponding value  $c_{\text{hf}} = 0.036 c_{10}$ , which is one fifth of the mean value. The JONSWAP  $\alpha$  data spans both limits in the range  $10^2 \leq \tilde{x} \leq 10^4$ , corresponding to changes in  $c_{\text{hf}}$  by a total factor of 25!\* On the other hand, since the energy data (Fig. 2.10) fall along a fairly well defined line  $\sim \tilde{x}$  in this range, the advective drag coefficient remains approximately constant. This forces us to reexamine our first-order hypothesis of self-similarity and a common scaling law for  $S$  and  $S_{\text{nl}}$ .

The ratios  $\tau_{\text{lf}}:\tau_{\text{mf}}:\tau_{\text{hf}}$  of the momentum fluxes obtained by integrating the nonlinear (momentum) source function over the low-frequency (positive), median-frequency (negative) and high-frequency (positive) lobes, respectively, are generally of order 1:(-4):3. These values are insensitive to the details of the spectral shape. For the mean JONSWAP spectrum – which agrees best with our data in the range around  $\tilde{x} \approx 10^3$  – we find  $\tau_{\text{lf}} \approx \tau_{\text{ad}} \approx 1/20 \tau$ . Thus the momentum advected away by the wave field is of the same order as the momentum transferred to the low-frequency waves by nonlinear interactions – or stated differently, the nonlinear momentum flux to low frequencies is approximately balanced by that fraction of the momentum input from the atmosphere which remains in the wave field and is not dissipated.

However, for short fetches ( $\tilde{x} \approx 10^2$ ) the higher JONSWAP  $\alpha$  values imply  $\tau_{\text{hf}} \approx \tau$  so that  $\tau_{\text{lf}} \approx 1/3 \tau_{\text{hf}} \approx 1/3 \tau$ , which is approximately six times greater than  $\tau_{\text{ad}}$ . Hence in this case the non-dissipated atmospheric input  $\tau_{\text{ad}}$  is unable to support the nonlinear momentum flux to low-frequencies. The momentum gained by the low frequencies must therefore be largely compensated by a momentum loss in the central region of the spectrum, so that – in contrast to the distribution shown in Fig. 2.12 – the positive and negative lobes of the net source function  $S$  (weighted with a factor  $k/\omega$  to transform from energy to momentum) approximately cancel. A large negative lobe in  $S$  tends to enhance the spectral peak relative to the background, or increase  $\gamma$  while decreasing  $\alpha$ . Fig. 2.8 and four of the five individual generation cases studied suggest that  $\gamma$  does indeed increase for small fetches, while  $\alpha$  decreases more rapidly than the power law (2.6.4) for a shape-preserving spectrum.

For fetches  $\tilde{x} > 10^3$ , the nonlinear momentum transfer to low frequencies decreases more rapidly than the net non-dissipated momentum  $\tau_{\text{ad}}$  supplied to the wave field. It follows that the growth of the spectrum at low frequencies is governed by the wind forces (and possibly dissipation) rather than wave-wave interactions. In this case, we should expect the peak to begin to flatten for  $\tilde{x} > 10^3$ . Figure 2.8 and the four individual generation cases mentioned above suggest that this may indeed be the case. For very large fetches, the asymptotic Pierson-Moskowitz spectrum is, of course, much flatter than the mean JONSWAP spectrum.

In summary, we find that for small fetches nearly all of the momentum flux  $\tau$  across the air-sea interface enters the wave field in the central region of the spectrum, in agreement with F. W. Dobson's [1971] direct measurements of surface pressure and wave height correlations.

About  $\left(90 + 5 \atop - 30\right)\%$  of the wave-induced momentum flux  $\tau_w$  is transferred to shorter waves by wave-wave interactions, where it passes to currents through dissipation, while  $\left(5 + 5 \atop - 2\right)\%$

\* The sensitivity of the nonlinear energy transfer on the spectrum, coupled with the sparsity of reliable data, led K. Hasselmann [1963b] to underestimate the significance of wave-wave scattering for the energy balance of the spectrum. The earlier computations were based on a Neumann spectrum, which has a far less pronounced peak than observed in the present spectra.

remains in the wave field and is advected away. Approximately  $(80 \pm 10)\%$  of the maximal wave growth observed on the forward face of the spectrum can be attributed to the nonlinear energy transfer across the spectrum\*. The corresponding energy loss on the rear slope of the peak is only partially balanced by the input from the atmosphere and results in a sharpening of the spectral peak towards the equilibrium form discussed in Section 2.8. The energy level of the spectrum adjusts to a value for which the nonlinear interactions are just able to remove (primarily to high wavenumbers) the energy supplied by the wind.

With increasing fetch, the nonlinear momentum transfer  $\tau_{hf}$  to high wavenumbers decreases to approximately 15% of  $\tau$  at  $\bar{x} = 10^3$ . The wave growth on the forward face of the spectrum is still dominated by the nonlinear transfer, but the associated energy loss on the rear slope of the peak is now largely compensated by the input from the atmosphere. Assuming negligible dissipation in the main part of the spectrum, approximately 20% of the momentum transfer to the ocean is needed to maintain the observed energy and momentum balance of the wave field. Alternatively, most of the momentum transfer across the air-sea interface may be entering into the principal wind sea components, as in the case of small fetches, and is being dissipated in the same region of the spectrum. Neither possibility can be ruled out on the basis of present observations or theories.

The same ambiguity besets the interpretation of the energy and momentum balance in the remaining fetch range extending from  $\bar{x} = 10^3$  to the upper limit  $\bar{x} = 10^4$ , where the spectral parameters border on the values for a fully-developed spectrum – assuming such a spectrum to exist. Our  $\alpha$  data, distributed below the mean line (2.4.4), indicate that the nonlinear transfer becomes less important than the atmospheric input in this range and that the spectral peak should begin to flatten again. The minimal wave-induced momentum flux without dissipation may fall to as low 5–10% of the total air-sea momentum flux – but any fraction up to the theoretical 100% limit is conceivable if dissipation in the central region of the spectrum is important.

Although we have not been able to observe a systematic transition of our spectra into a fully developed spectrum of the form proposed by Pierson and Moskowitz, it is interesting to note that the parameters  $\alpha = 0.081$ ,  $\bar{f}_m = 0.14$  of the latter spectrum lie rather close to the mean curves (2.4.3) and (2.4.4) – as opposed to our  $\alpha$  data for  $10^3 < \bar{x} < 10^4$ . Hence wave-wave interactions should still be significant for the fully developed spectrum. Computations of the nonlinear momentum transfer  $\tau_{hf}$  to high frequencies for the Pierson-Moskowitz spectrum imply a minimal wave-induced drag  $\tau_w^{\min} \approx 0.09 \tau$ . (Fig. 2.21 b.)

## 2.10. Variability of the Spectrum

Having considered the average properties of the energy balance of the wave field, we return now to the question of the variability of the peak shape parameters. As pointed out in Section 2.4, the considerable scatter of  $\gamma$ ,  $\sigma_a$  and  $\sigma_b$  in Fig. 2.8, and to a lesser extent  $\alpha$  in Fig. 2.7, cannot be explained simply by the statistical uncertainty of the spectral estimates or the neglect of additional external parameters in Kitaigorodskii's similarity law. The fact that comparable scatter is observable also within individual generation cases (Section 2.7) suggests a small-scale mechanism such as the gustiness of the wind as origin. However, since the peak is a stable feature of the nonlinear energy transfer (Section 2.8), some additional

---

\* Motivated by linear feedback theories of wave generation, the growth rate on the forward face of the spectrum has generally been expressed in previous field experiments in terms of the exponential growth factor  $\beta = S/E$ . For a self-similar spectrum defined by (2.4.1), (2.4.5) we obtain  $\beta \approx 6 \left( \frac{U_{10}}{c} \right)^n \cdot 10^{-3} \cdot f$ , where  $c$  is the phase velocity and  $n = 1.03$  or  $1.33$  depending on whether the scaling laws (2.4.3), (2.4.4) or (2.4.3), (2.4.7) are applied. Both relations agree within the scatter of the data with R. L. Snyder and C. S. Cox's [1966] and T. P. Barnett and J. C. Wilkerson's [1967] results in the range  $1.2 < U_{10}/c < 3$  relevant for this experiment. J. R. Schule et al. [1971] measured somewhat smaller growth rates.

instability mechanism must be acting to magnify the effect of weak inhomogeneities of the wind field on the peak shape parameters.

An instability of this kind may be identified in the propagation characteristics of the energy of the peak. Locally, the peak energy propagates in space at the group velocity corresponding to peak frequency  $f_m$ . However, at the same time the peak moves in the frequency domain towards lower frequencies. Hence we may envisage the energy of the peak as following a curved characteristic in the  $x-t$  plane defined by the pair of equations

$$\frac{dx}{dt} = \frac{g}{4\pi f_m} \quad (\text{group velocity at frequency } f_m)$$

$$\frac{df_m}{dt} = -\lambda(x)$$

where the rate of decrease  $\lambda(x)$  of  $f_m$  is a given function of  $x$  depending on the local wave spectrum. In the ideal case of a homogeneous, stationary wind field, the set of characteristics emanating from the initial (shore) line  $x = 0$  at different initial times  $t_0$  are displaced parallel to one another and never intersect. However, small perturbations of the wind field produce local distortions and displacements of the characteristics which normally lead to an intersection of the rays at some distance from the disturbance. At the caustic points, the peak is enhanced by the superposition of energy from different origins, whereas the energy is reduced in regions in which the characteristics diverge. (It may be noted in this context that the observed variability of the peak-shaped parameters can not be reduced by considering the combination  $\gamma(\sigma_a + \sigma_b)$ , which is roughly proportional to the energy in the peak. Thus the scatter cannot be explained simply as a local redistribution of the energy within the peak, but represents a variability both in the net energy and the shape of the peak.) Physically, a gust of, say, 2 km scale will cause a local shift of the peak towards lower frequencies, causing the peak to propagate faster than peaks generated earlier by the undisturbed wind at the same fetch. Ultimately, the peak generated in the gust will then overtake the earlier peaks, (Fig. 2.23).

To express this analytically, we need to translate the spectral form of the radiative transfer equation (2.1.1) into an equivalent parametrized form. Let us assume generally that

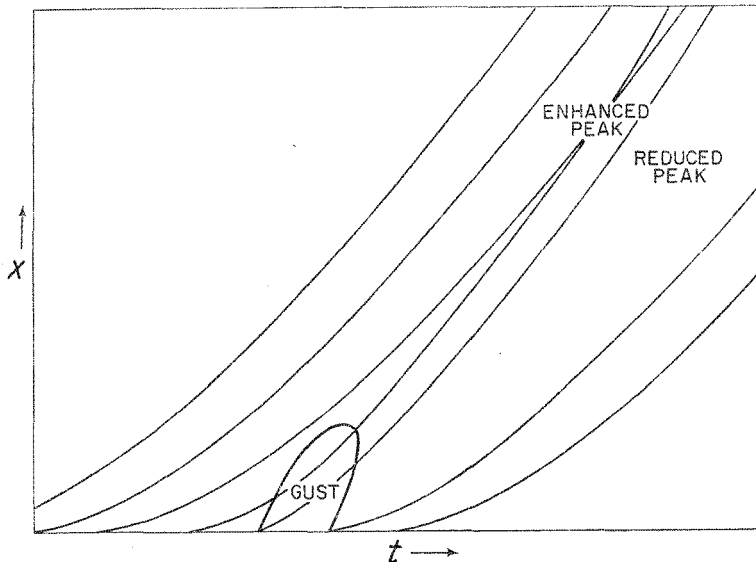


Fig. 2.23. Focusing of peak propagation characteristics by small scale inhomogeneities of the wind field



we can model all spectra  $F(\mathbf{k}; \mathbf{x}, t)$  in a given problem by a class of functions  $\tilde{F}(\mathbf{k}; a_1, \dots, a_n)$  containing  $n$  free parameters  $a_j$ , and that there exists an algorithm for computing the parameters for any given spectrum  $F(\mathbf{k})$  by some best-fitting procedure,

$$a_j = \varphi_j(F) \quad (2.10.1)$$

where the functional  $\varphi_j$  is differentiable, i.e. a variation  $\delta F(\mathbf{k})$  yields a variation of the parameters

$$\delta a_j = \varphi'_j(\delta F) \quad (2.10.2)$$

in which  $\varphi'_j$  is a linear functional of  $\delta F$ .

Applying (2.10.2) to a variation of the model spectrum

$$\begin{aligned} \delta \tilde{F} &= \frac{\partial \tilde{F}}{\partial a_j} \delta a_j, \quad \text{it follows that} \\ \varphi'_i \left( \frac{\partial \tilde{F}}{\partial a_j} \right) &= \delta_{ij}. \end{aligned} \quad (2.10.3)$$

Since we assume that  $F$  can be approximated by  $\tilde{F}$  for all  $\mathbf{x}$  and  $t$ , we may substitute  $\tilde{F}$  in the radiative transfer equation (2.1.1) to obtain

$$\frac{\partial \tilde{F}}{\partial a_j} \left( \frac{\partial a_j}{\partial t} + \mathbf{v} \cdot \nabla a_j \right) = S. \quad (2.7.1)$$

Applying the operation  $\varphi'_i$  and invoking (2.10.3), the parametrized radiative transfer equation takes the form

$$\frac{\partial a_i}{\partial t} + D_{ijk} \frac{\partial a_j}{\partial x_k} = S_i \quad (2.10.4)$$

where

$$D_{ijk} = \varphi'_i \left( v_k \frac{\partial \tilde{F}}{\partial a_j} \right) \quad (2.10.5)$$

and

$$S_i = \varphi'_i(S). \quad (2.10.6)$$

Both the coefficients  $D_{ijk}$  and the source function  $S_i$  depend on the parameters  $a_j$ ; the latter also depends on the wind speed and possibly other parameters. We have neglected the refractive terms in (2.10.4).

In the case of the parametrization  $(a_1, \dots, a_5) = (f_m, \alpha, \gamma, \sigma_a, \sigma_b)$  applied in this experiment, all of the parameters except  $\alpha$  depend only on the properties of the spectrum in a narrow band of frequencies around the spectral peak (we ignore parameters specifying the directional distribution, as these were retained constant). Thus  $\varphi_i$  and  $\varphi'_i$  are essentially zero outside this band. In the functional  $\varphi'_i$  in (2.10.5) we may then replace the smoothly varying function  $v = g/4\pi f$  to first order by the constant value  $v_m = g/4\pi f_m$ , obtaining

$$D_{ij} = v_m \varphi'_i \left( \frac{\partial \tilde{F}}{\partial a_j} \right) + \text{higher order terms } \varepsilon_{ij} \text{ or, invoking (2.10.3),} \quad (2.10.7)$$

$$D_{ij} = v_m \delta_{ij} + \varepsilon_{ij}. \quad (2.10.8)$$

(The index  $k$  has been dropped since now  $\mathbf{x} \equiv x$ .) Equations (2.10.4) and (2.10.8) imply that the parameters characterizing the peak propagate approximately along characteristics defined by the fetch-dependent group velocity  $v_m$ , as anticipated.

In the case of  $\alpha$ , the appropriate propagation velocities  $D_{\alpha j}$  will be smaller than  $v_m$ , as  $\varphi_\alpha$  and  $\varphi'_\alpha$  are governed by the more slowly propagating, shorter waves of the spectrum.  $\alpha$  was determined in the present experiment by least-square fitting a Pierson-Moskowitz spectrum with free ordinate scales  $\alpha$ ,  $f_m$  to the observed spectrum in the frequency range  $1.2 f_m$  to  $0.7$  Hz (after prewhitening with the factor  $f^5$ ). With this procedure,  $\alpha$  is independent of the shape parameters (which were determined subsequently) and only weakly dependent on  $f_m$ , so that

$$\varphi'_\alpha \left( v \frac{\partial \tilde{F}}{\partial a_j} \right) = 0 \quad \text{for } j = 3, 4, 5$$

$$\varphi'_\alpha \left( v \frac{\partial \tilde{F}}{\partial f_m} \right) = \varepsilon_{\alpha f_m} \ll v_\alpha$$

where  $v_\alpha = \varphi'_\alpha (v \partial \tilde{F} / \partial \alpha)$  is an average group velocity in the frequency band  $1.2 f_m$  to  $0.7$  Hz.

Thus for all parameters, the propagation matrix  $D_{ij}$  is approximately diagonal, and eq. (2.10.4) takes the form

$$\frac{\partial a_i}{\partial t} + v_{(i)} \frac{\partial a_i}{\partial x} + \varepsilon_{ij} \frac{\partial a_j}{\partial x} = S_i \quad (2.10.9)$$

where

$$v_{(i)} = \begin{cases} v_\alpha & \text{for } i = 1 \\ v_m & \text{for } i = 2, \dots, 5 \end{cases} \quad \begin{array}{l} \text{(The index } i \text{ is enclosed in parenthesis to indicate} \\ \text{that it is excluded from the summation convention.)} \end{array}$$

Consider now a solution of (2.10.9),  $a_i = \bar{a}_i + a'_i$ , which consists of the known time-independent solution  $\bar{a}_i(x)$  for a given time-independent source  $S_i$  and a superimposed time-dependent fluctuation  $a'_i(x, t)$  induced by a small fluctuation  $S'_i(x, t)$ . Subtracting the transfer equations for  $a_i$  and  $\bar{a}_i$  we obtain, with  $v_{(i)} = \bar{v}_{(i)} + v'_{(i)}$ ,  $\mathcal{E}_{ij} = \bar{\mathcal{E}}_{ij} + \mathcal{E}'_{ij}$ ,

$$\begin{aligned} \frac{\partial a'_i}{\partial t} + v_{(i)} \frac{\partial a'_i}{\partial x} + \varepsilon_{ij} \frac{\partial a'_j}{\partial x} &= S'_i - v'_{(i)} \frac{\partial \bar{a}}{\partial x_i} - \varepsilon'_{ij} \frac{\partial \bar{a}_j}{\partial x} \\ &= R_i(\bar{a}, a', x, t), \text{ say.} \end{aligned} \quad (2.10.10)$$

Making use of the fact that the cross-coupled terms  $\varepsilon_{ij} \partial a'_j / \partial x$  are small compared with the diagonal propagation terms  $v_{(i)} \partial a'_i / \partial x$ , equations (2.10.10) may be solved iteratively, the  $n$ th iteration  $a_{i,n}$  being defined as the solution of

$$\begin{aligned} \frac{\partial a_{i,n}}{\partial t} + v_{(i)}(\bar{a} + a_{n-1}) \cdot \frac{\partial a_{i,n}}{\partial x} &= -\varepsilon_{ij}(a_{n-1}) \cdot \frac{\partial a_{j,n-1}}{\partial x} \\ &+ R_i(\bar{a}, a_{n-1}, x, t). \end{aligned} \quad (2.10.11)$$

Setting  $a_{i,0} = 0$ , the first-order solution is obtained by integrating (2.10.11) along the zero'th order characteristics

$$\frac{dx}{d\theta} = v_{(i)}(\bar{a}_1) \quad (\bar{a}_1 = f_m)$$

$$\frac{dt}{d\theta} = 1.$$

The second iteration then involves integration along the perturbed characteristics

$$\frac{dx}{d\vartheta} = v_{(i)} (\bar{a}_1 + a_{1,1})$$

$$\frac{dt}{d\vartheta} = 1.$$

The rays  $x = x(\vartheta, t_0)$ ,  $t = \vartheta + t_0$  obtained by integrating these equations under the initial condition  $x = 0$  for  $t = t_0$  will, in general, not yield a unique mapping of the entire  $x, t$  plane into the plane of characteristic coordinates  $\vartheta, t_0$ , since the rays will normally cross at some finite distance from the initial boundary line  $x = 0$ . The caustic limiting the one-to-one mapping region is defined by the condition

$$A = \begin{vmatrix} \frac{\partial x}{\partial \vartheta} & \frac{\partial t}{\partial \vartheta} \\ \frac{\partial x}{\partial t_0} & \frac{\partial t}{\partial t_0} \end{vmatrix} = v_{(i)} - \int_0^{\vartheta} \frac{\partial}{\partial t_0} v_{(i)} (x(t_0, \vartheta')) d\vartheta' = 0. \quad (2.10.12)$$

Beyond the caustic, the solutions  $a_{i,2}$  are no longer uniquely defined. This probably represents a limitation of the iteration procedure rather than a genuine singularity of the complete solution  $a_i$ . At the caustic, the perturbations  $a_i$  become large and the iterative approach is no longer valid. This can be seen by continuing the iteration to the third order, for which the cross-coupled gradient terms on the right-hand side

$$\begin{aligned} \varepsilon_{ij} \frac{\partial a_{j,2}}{\partial x} &= \varepsilon_{ij} \left[ \frac{\partial a_{j,2}(\vartheta, t_0)}{\partial \vartheta} \cdot \frac{\partial \vartheta}{\partial x} + \frac{\partial a_{j,2}(\vartheta, t_0)}{\partial t_0} \frac{\partial t_0}{\partial x} \right] \\ &= \varepsilon_{ij} \left[ \frac{\partial a_{j,2}}{\partial \vartheta} - \frac{\partial a_{j,2}}{\partial t_0} \right] A^{-1} \end{aligned}$$

are found to approach infinity at the caustic  $A = 0$ .

A quantitative analysis of the behaviour of the solution near the caustic requires a more detailed investigation of the source function than can be given here. We note here simply that the amplification of the perturbations near the caustic is associated formally with the existence of the cross-coupling gradient terms  $\varepsilon_{ij} \partial a_i / \partial x_j$ . In the case of  $a_1 \equiv f_m$ , these terms vanish since  $f_m$  is defined independently of the remaining spectral parameters; the scatter of  $f_m$  is indeed found to be considerably smaller than for the remaining spectral parameters.  $\alpha$  also contains only a weak cross term  $\varepsilon_{\alpha f_m} \cdot \partial f_m / \partial x$  and is observed to have less scatter than the shape parameters, which can be shown to be more strongly cross-coupled (particularly to  $\alpha$ ). Thus intersections of the characteristics yield large variations of the peak energy and bandwidth, but only minor changes in the peak frequency and the high-frequency range of the spectrum – as would be expected physically.

The distance of the caustics downwind from the generating wind-field inhomogeneities depends on the scale and magnitude of the perturbations. According to eq. (2.10.12), a gust of time scale  $T$  causing a local perturbation of the peak frequency  $\delta f_m = -r f_m$  (which then persists along the peak propagation path) will result in the development of a caustic at a downwind distance  $x$  defined by

$$0 = v_m - \int \frac{\partial v_m}{\partial f_m} \frac{\partial \delta f_m}{\partial t_0} d\vartheta' \approx v_m - \int v_m \frac{r}{T} d\vartheta' \approx v_m - \frac{x r}{T}$$

or

$$x = 0 \left( \frac{v_m T}{r} \right).$$

For example, a gust of ten minute duration producing a 10 % change in the peak frequency at 0.4 Hz ( $v_m \approx 2$  m/s) would produce unstable caustic amplification about 12 km downwind. The values appear consistent with the magnitudes and scales of observed fluctuations (Section 2.7).

## 2.11. Conclusions

From measurements and computations of the net source function, the energy transfer due to nonlinear resonant wave-wave interactions, and the net local momentum transfer from the atmosphere to the ocean, we have been able to identify the following principal features of the energy balance of fetch-limited spectra:

1. The shape of the spectrum is determined primarily by the nonlinear energy transfer from the central region of the spectrum to both shorter and longer wave components. In particular, the pronounced peak and steep forward face can be explained as a self-stabilizing feature of this process. The rapid wave growth observed for waves on the forward face of the spectrum can also be largely attributed to the nonlinear transfer to longer waves.

2. For short fetches ( $\tilde{x} = gx/U_{10}^2 = O(10^2)$ ) approximately  $80\% \pm 20\%$  of the total momentum  $\tau$  transferred from the atmosphere to the ocean goes into the principal components of the wave spectrum, in accordance with F. W. Dobson's [1971] measurements. About  $\left(5 \begin{smallmatrix} +5 \\ -2 \end{smallmatrix}\right)\%$  of the momentum  $\tau_w$  transferred from the atmosphere to the waves is retained in the wave field and is advected away. The rest is transferred by nonlinear interactions to short waves, where it is converted to current momentum by dissipative processes. In the main part of the spectrum the dissipation appears to be negligible.

3. For larger fetches ( $\tilde{x} = 10^3 - 10^4$ ), the advection of momentum by the wave field is of the order of 5 % of the total momentum transfer  $\tau$ , as before, but the momentum transferred to short waves by nonlinear interactions drops to  $\left(20 \begin{smallmatrix} +20 \\ -15 \end{smallmatrix}\right)\%$  of  $\tau$ . In the absence of direct measurements of the atmospheric input and the dissipation, it can be concluded in this case only that the spectral energy balance must lie between two limiting situations: the wave-induced drag  $\tau_w$  accounts for  $\left(25 \begin{smallmatrix} +25 \\ -15 \end{smallmatrix}\right)\%$  of  $\tau$ , and all of the dissipation occurs via the nonlinear transfer to high wavenumbers, or  $\tau_w$  is of the order of  $\tau$ , and most of the momentum entering the wave spectrum is dissipated by processes involving only a minor redistribution of energy by resonant wave-wave interactions.

4. To first order, wave-tank and field data from various sources scale in accordance with S. A. Kitaigorodskii's [1962] law. Over a five decade range of fetches extending from  $\tilde{x} = 10^{-1}$  to  $10^4$ , the frequency and energy scales of the wave spectrum vary in such a manner that the minimal wave-induced drag  $\tau_w^{\min}$  (as inferred from highly scale-sensitive computations of the nonlinear transfer to short waves) lies in a range between 10 % and 100 % of  $\tau$  – supporting the view that in general the spectrum adjusts to a level at which the energy input by the wind can be largely removed by the nonlinear energy transfer to shorter waves. This would explain, among other features, the similarity of the spectral shape for wave-tank and field experiments and the observed decrease of Phillips' "constant"  $\alpha$  with fetch. The JONSWAP data falls within the last two decades of these plots; the decrease in the ratio  $\tau_w^{\min}/\tau$  with fetch discussed in points 2. and 3. reflects a small but systematic deviation of the JONSWAP  $\alpha$  data from the mean trend over all wave-tank and field data. This may point to limitations in attempting to scale complex atmospheric boundary-layer processes in terms of the wind speed alone.

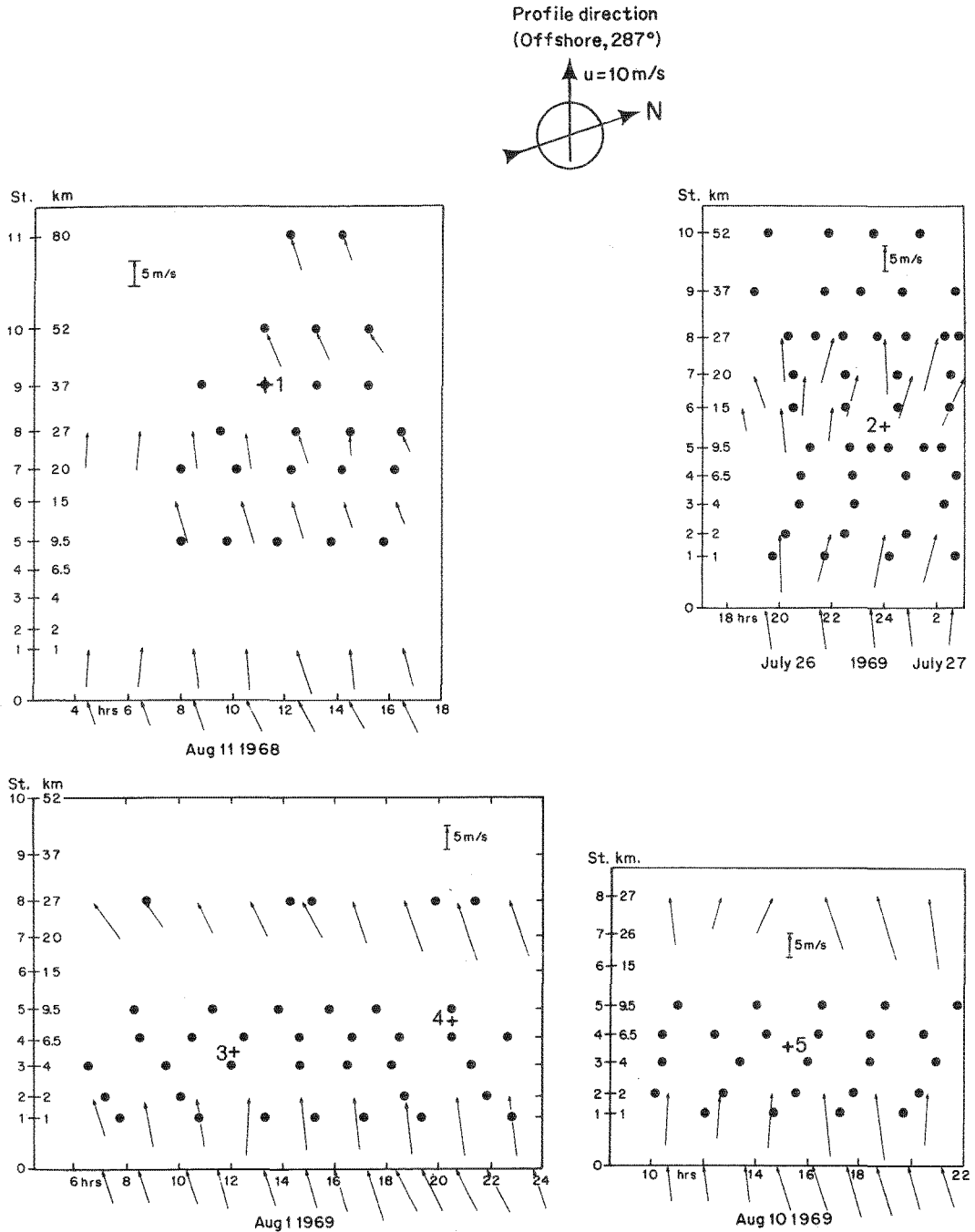
A number of questions have remained unanswered. The mechanism of the energy transfer from the wind to the waves was not determined. The transition of the fetch-limited spectrum

to a fully developed equilibrium form (assuming this exists) involves a number of open problems, including the role of dissipation in the low-frequency range of the spectrum. Finally, the mechanism of energy dissipation at high wavenumbers remains to be clarified. It is intended to investigate some of these questions in more detail in future joint studies.

Applied to the problem of numerical wave prediction, the principal conclusion to be drawn from our study is that the nonlinear energy transfer due to wave-wave scattering requires more careful modelling than hitherto. Ignored entirely in earlier prediction schemes (e.g. L. Baer [1963], W. J. Pierson, L. J. Tick and L. Baer [1966]), the nonlinear transfer terms have been parametrised by rather simple – essentially scaling – relations in later models (T. P. Barnett [1968], J. A. Ewing [1971]). It appears now that a more sophisticated description including a number of critical shape parameters is called for.

## Appendix

Wind field and spectral parameters for generation cases 1–5 as summarised in Table 2.



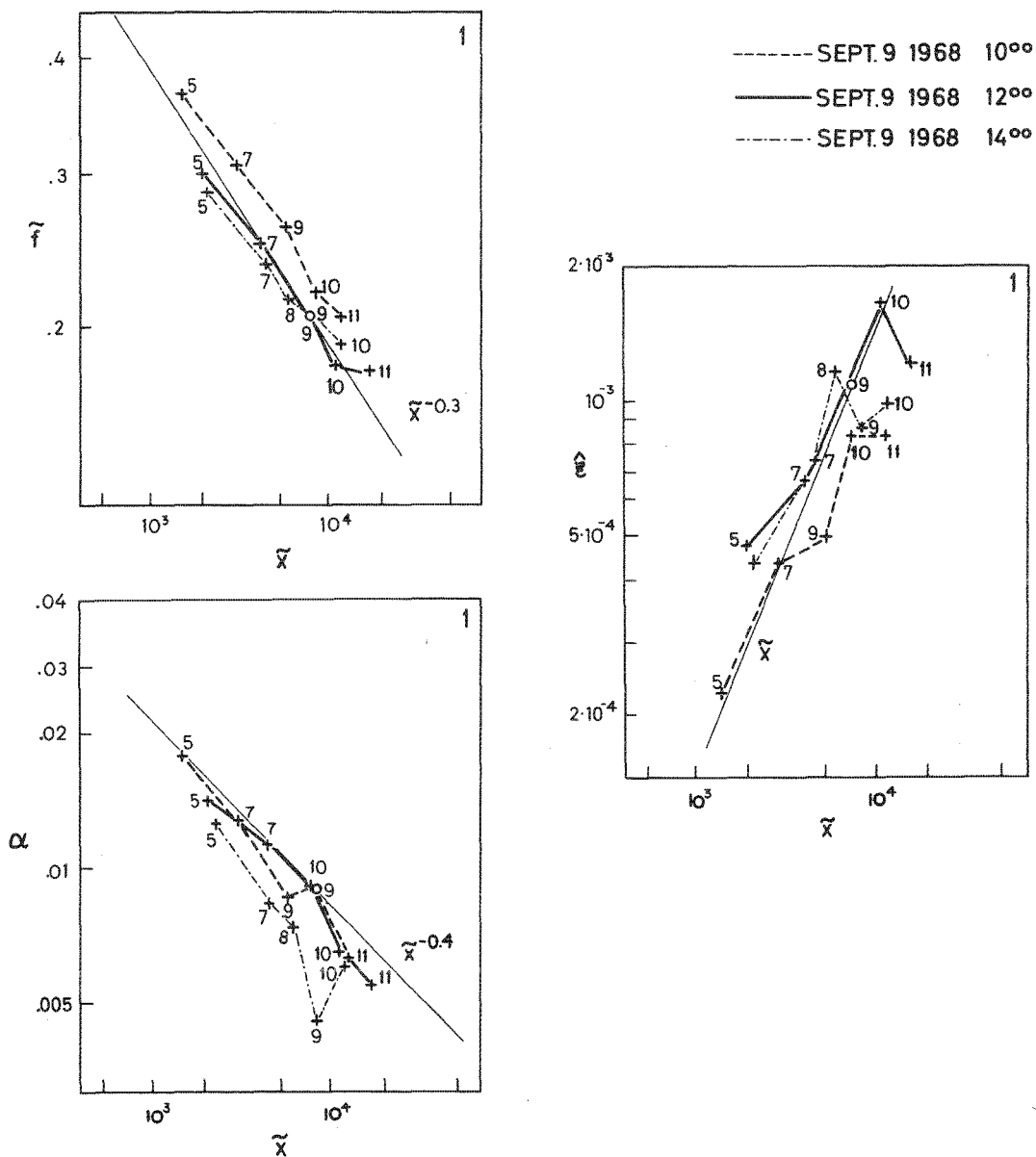


Fig. 2 A.2. Scale parameters  $\tilde{f}$ ,  $\alpha$  and  $v \cdot x$  for generation case 1. The dot (Station 9) denotes the position at which the source function was computed. Straight lines represent the fetch dependence used in computing the derivatives  $\frac{1}{\tilde{x}}$ . Estimates of the (smaller) time derivatives were obtained from neighbouring measurements taken 2 hrs. earlier and later (broken lines) than the measurements at 12<sup>h</sup> (full line)

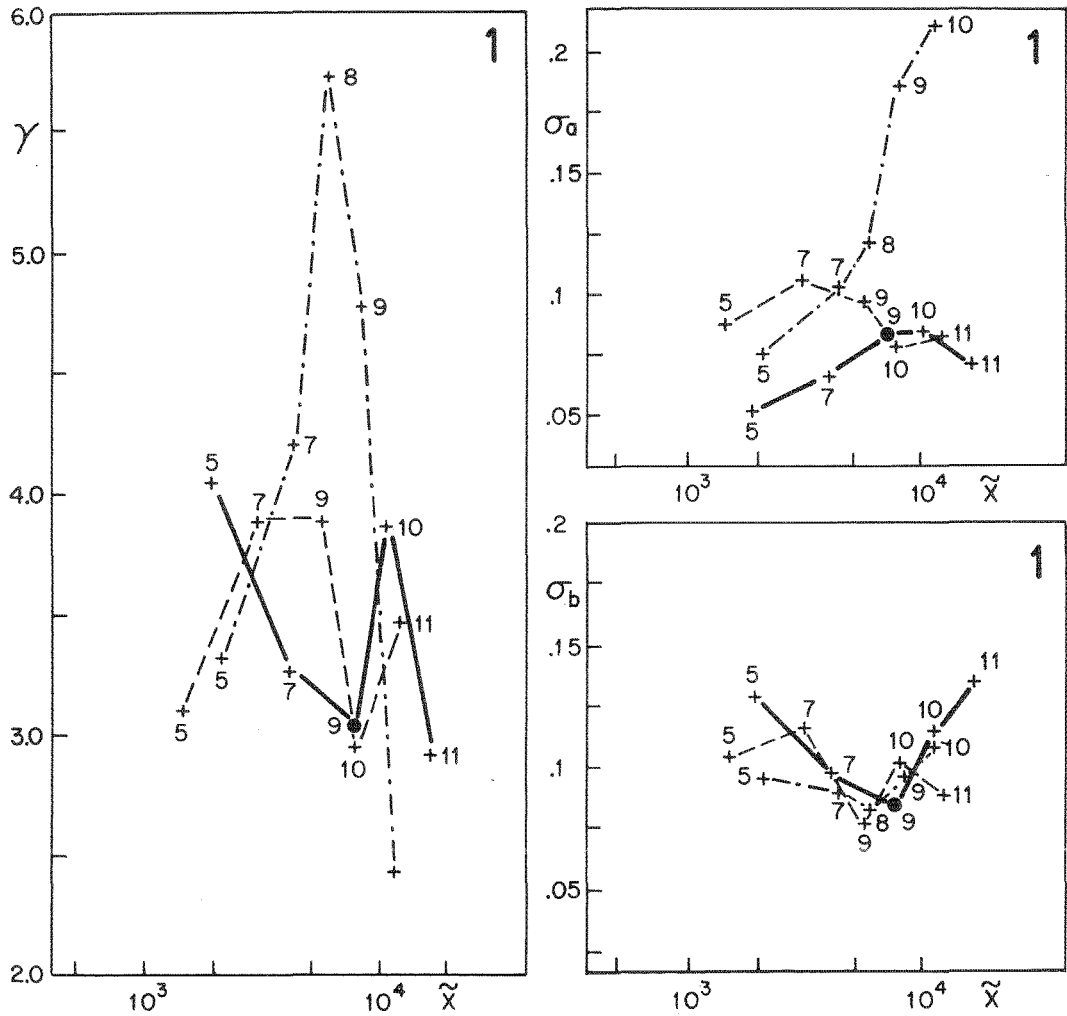


Fig. 2 A.3. Shape parameters, and  $v \cdot x$  for generation case 1. Meaningful  $x$  and  $t$  derivatives cannot be defined on account of the scatter



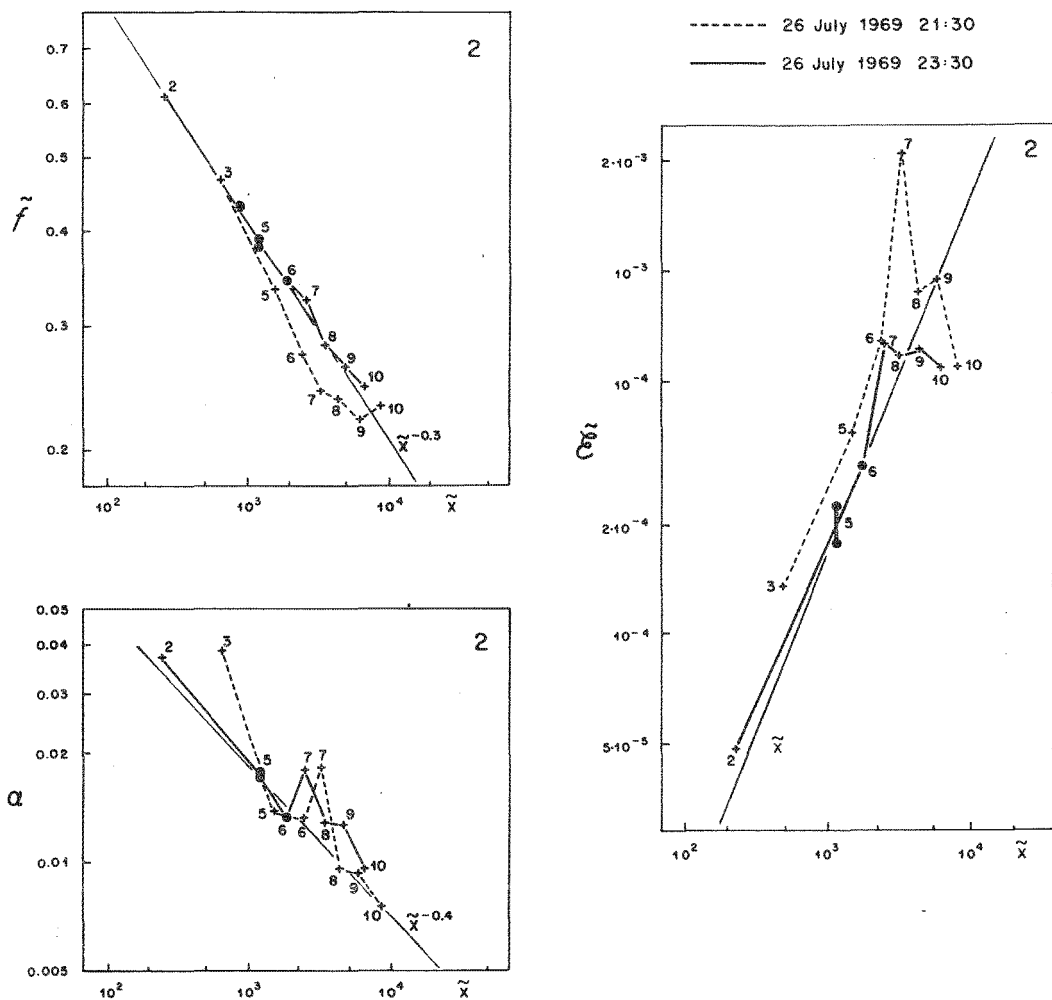


Fig. 2 A.4. Same as Fig. 2 A.2 for generation case 2

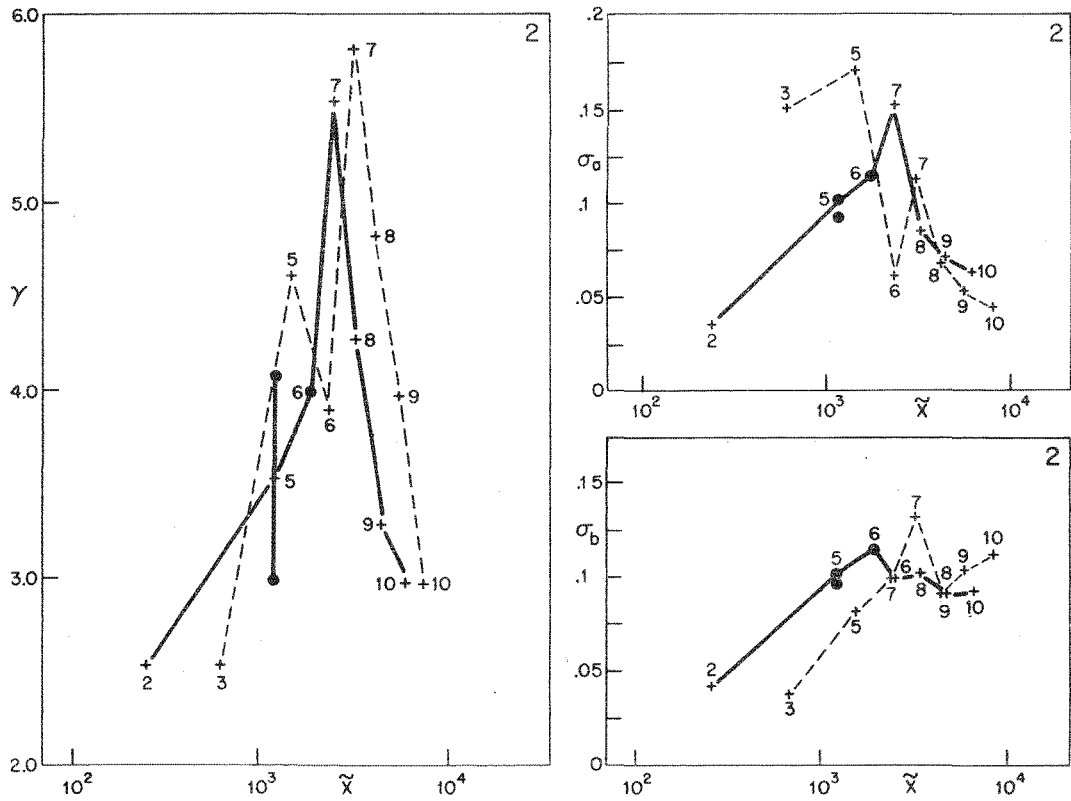


Fig. 2 A.5. Same as Fig. 2 A.3 for generation case 2

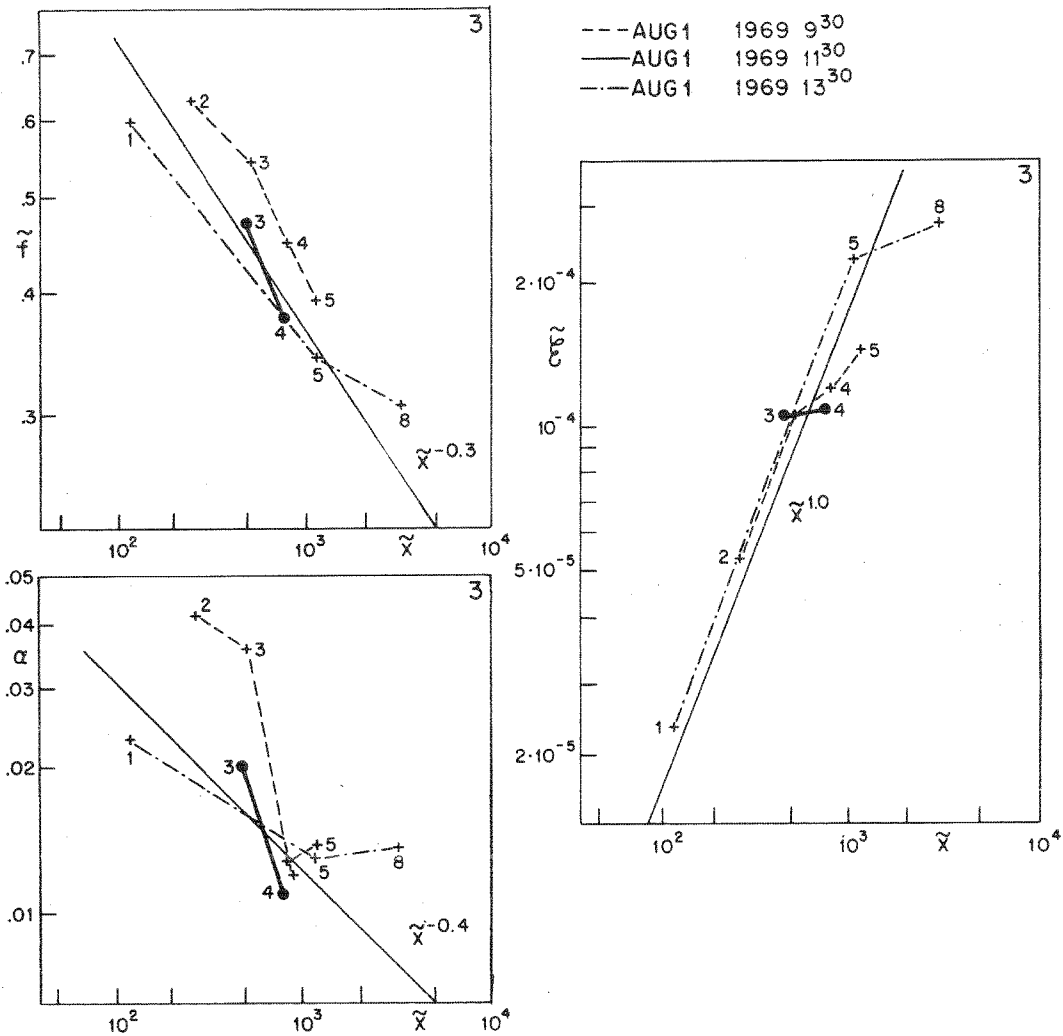


Fig. 2 A.6. Same as Fig. 2 A.2 for generation case 3

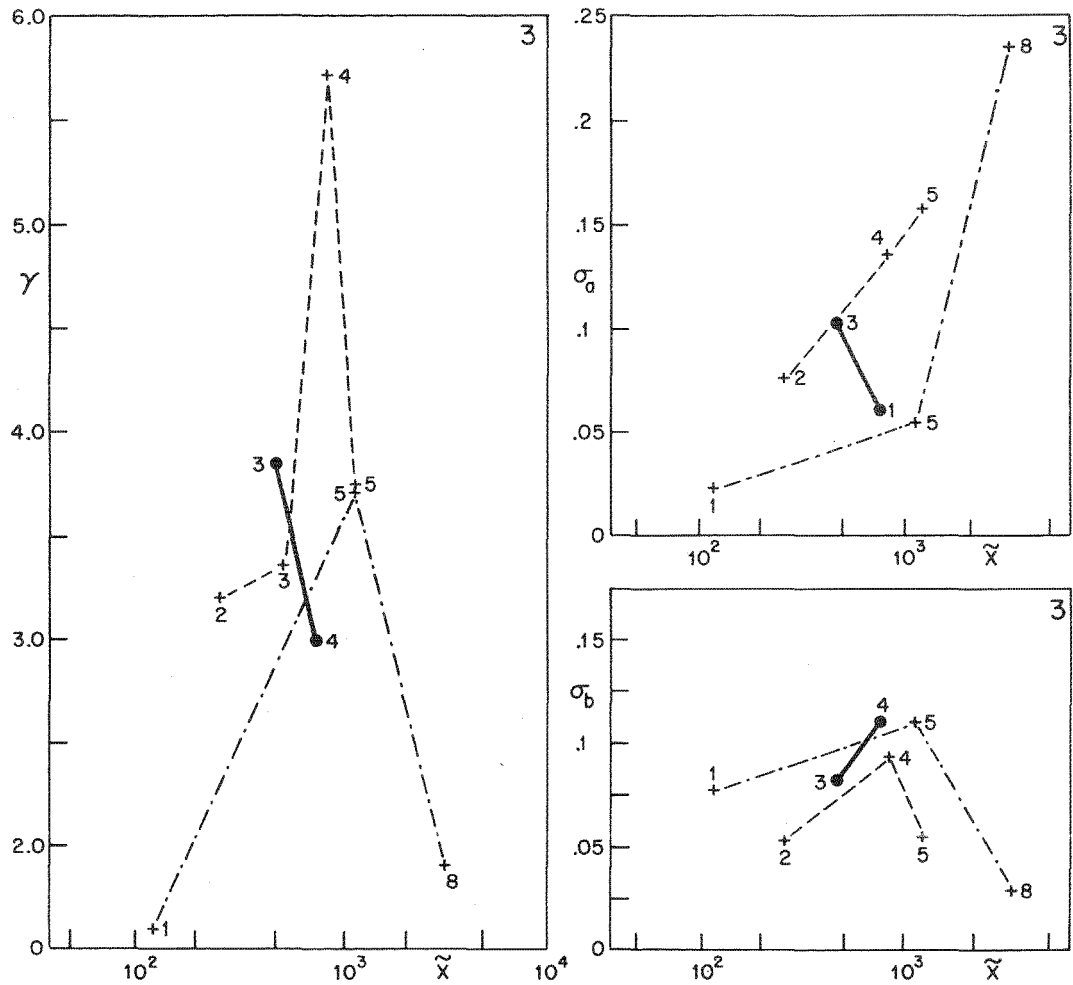


Fig. 2 A.7. Same as Fig. 2 A.3 for generation case 3

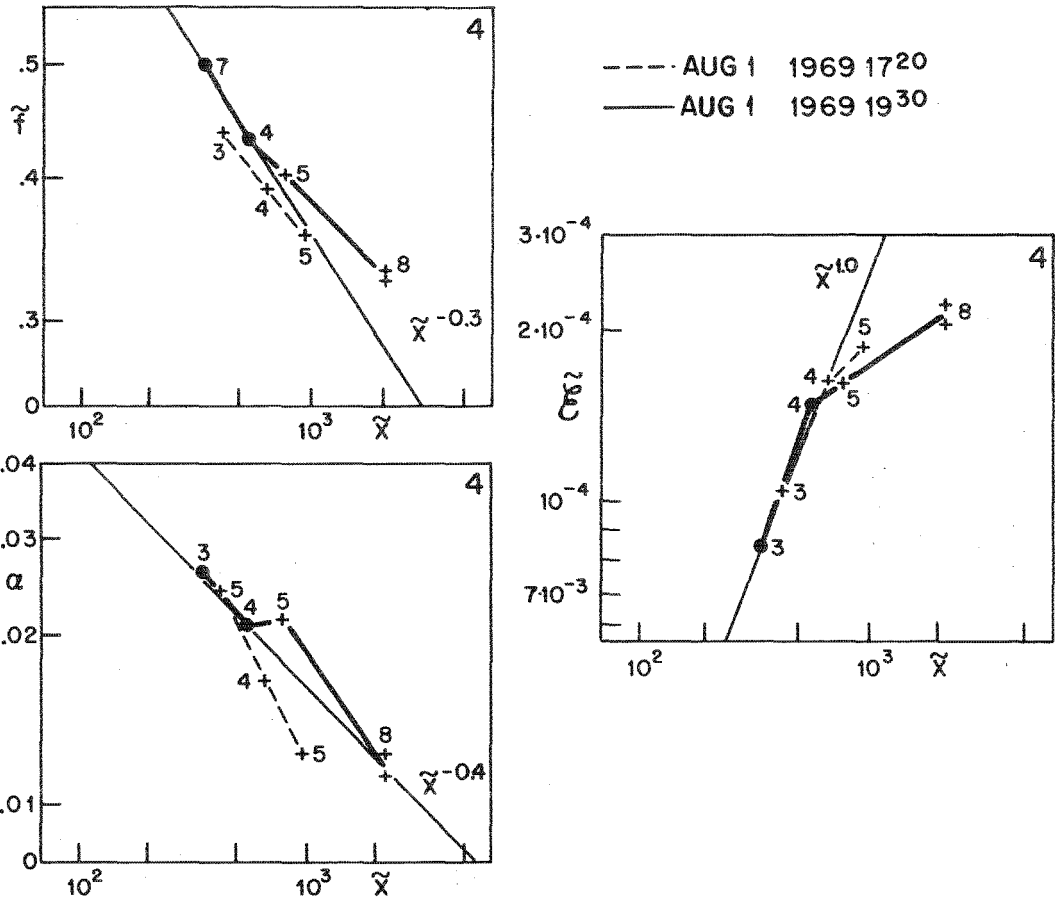


Fig. 2 A.8. Same as Fig. 2 A.2 for generation case 4

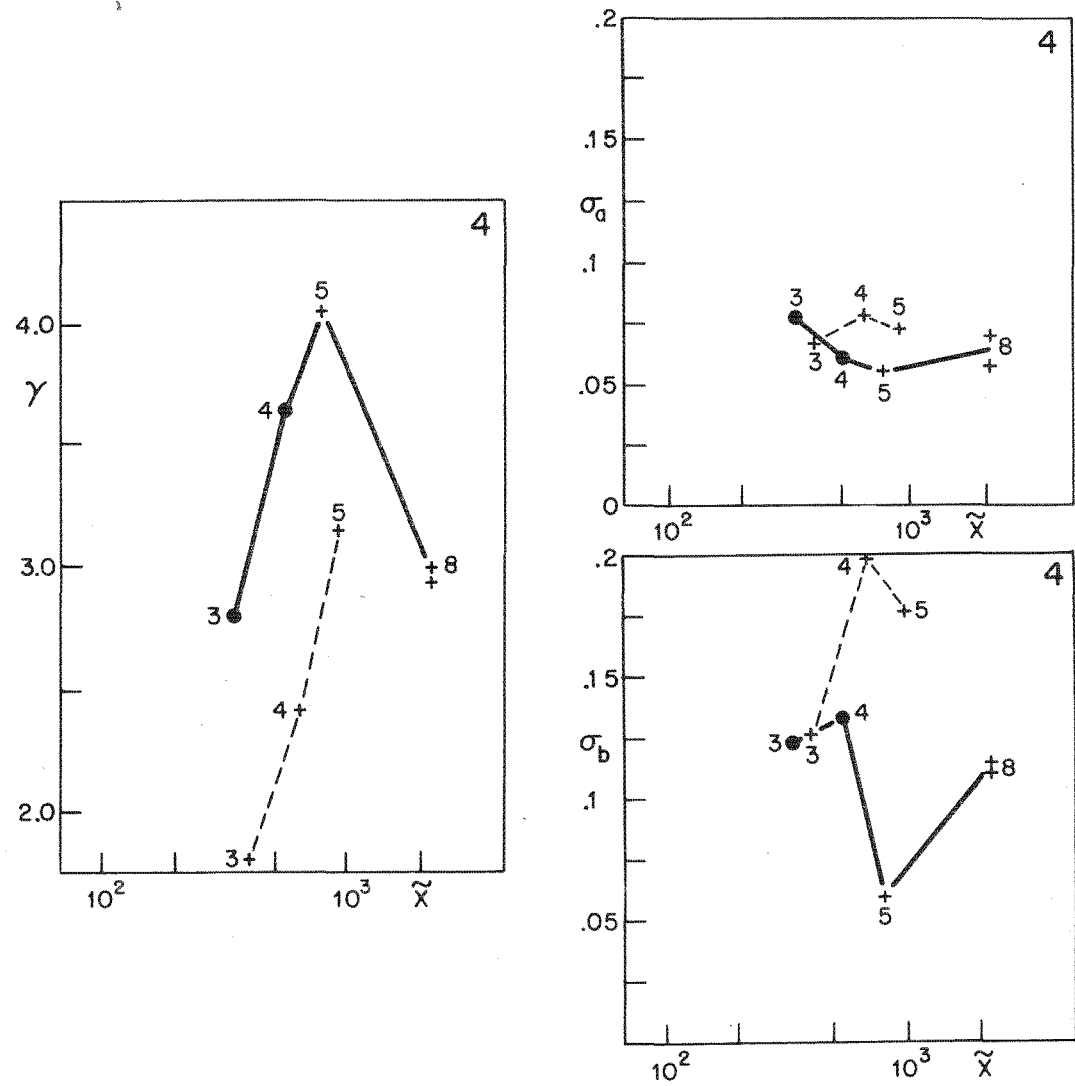


Fig. 2 A.9. Same as Fig. 2 A.3 for generation case 4

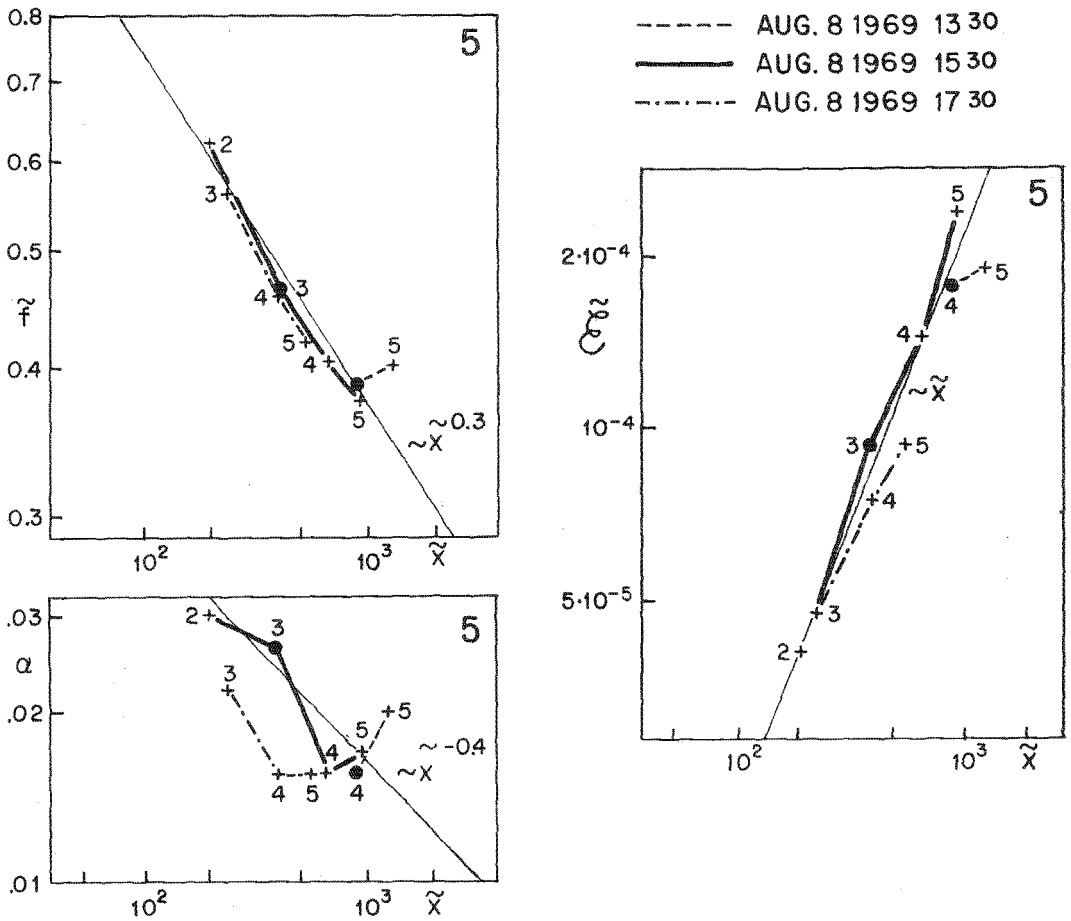


Fig. 2 A.10. Same as Fig. 2 A.2 for generation case 5

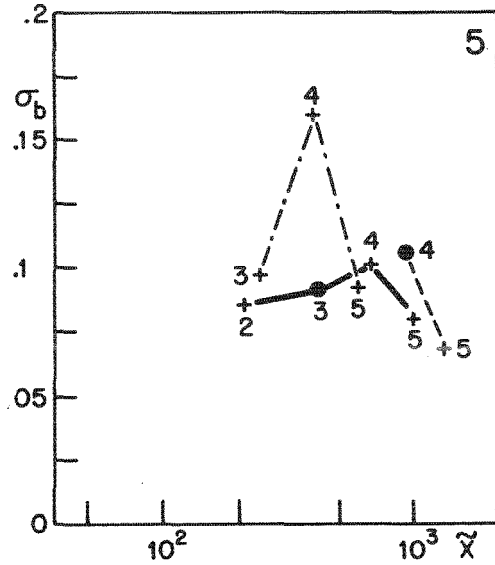
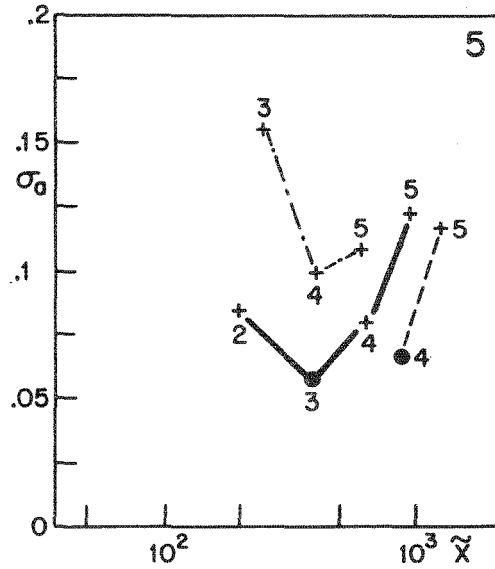
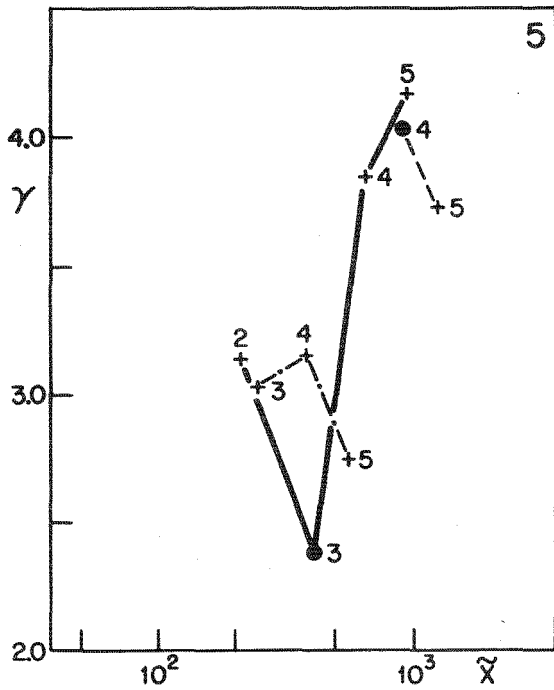


Fig. 2 A.11. Same as Fig. 2 A.3 for generation case 5



### 3. Swell Attenuation

#### 3.1. Conservation of Action and Energy Flux

A little less than one-third (654) of the wave spectra recorded during JONSWAP contained well-defined low-frequency swell peaks. In most cases the swell energy decreased from the outer to the innermost stations of the profile by factors varying from 0.2 to 0.7; the strongest decay occurred along the inshore, shallower section of the profile (cf. Fig. 3.1). The swell beams were sufficiently narrow to be characterized simply by their mean frequency  $f$ ,

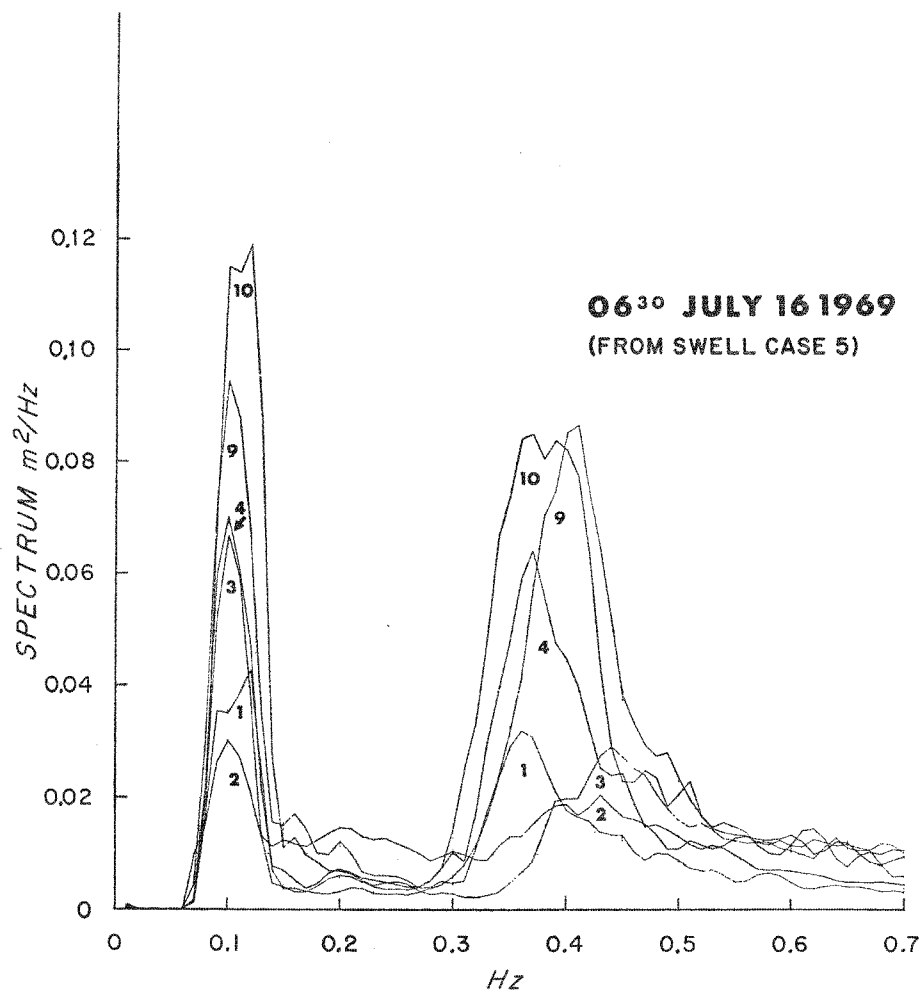


Fig. 3.1. Examples of swell peaks observed during swell case 5. Numbers refer to wave stations. The swell energy decreases towards shore, with the exception of Station 1, where the energy is enhanced by refraction (the energy flux  $I$  at Station 1 is generally smaller than at Station 2, cf. Fig. 3.2)

frequency width  $\Delta f$ , mean direction  $\theta$  ( $=\theta_m$ , cf. Section 1.5), directional spread  $\Delta\theta$  ( $=\theta_s$ ) and total energy  $\mathcal{E}$  – or, more conveniently, the total shoreward energy flux  $I = v_x \mathcal{E}$ , where  $v_x = v \cos \theta$  is the group velocity of the swell in the direction parallel to the profile. In the ideal case of no energy loss, negligible refraction by currents, parallel bottom contours orthogonal to the profile and constant swell frequency, the flux  $I$  remains constant along the propagation path of the swell.

In the general case in which no restrictions are invoked other than the standard assumption of slowly varying mean fields, the rate of change of  $I$  or  $\mathcal{E}$  can be deduced from the action balance equation

$$\frac{\partial N}{\partial t} + \frac{\partial}{\partial x_i} (\dot{x}_i N) + \frac{\partial}{\partial k_i} (k_i N) = S/\omega' \quad (3.1.1)$$

where  $N(\mathbf{k}; \mathbf{x}, t) = F(\mathbf{k}; \mathbf{x}, t)/\omega'$  is the action spectrum,  $\omega' = (gk \tanh kH)^{1/2}$  is the (intrinsic) frequency of the wave components in a reference system moving with the local current  $\mathbf{U}(\mathbf{x}, t)$ ,  $H(\mathbf{x}, t)$  is the water depth,

$$\begin{aligned} \dot{x}_i &= v_i = \partial\Omega/\partial k_i \\ k_i &= -\frac{\partial\Omega}{\partial x_i} \end{aligned} \quad (3.1.2)$$

and  $\omega = \Omega(\mathbf{k}, \mathbf{x}, t) = (gk \tanh kH)^{1/2} + \mathbf{k} \cdot \mathbf{U}$  denotes the dispersion relation in a fixed reference system.

Equation (3.1.1) represents the generalization of the energy balance equation (2.1.1) to the case of refraction by arbitrary space- and time-dependent currents and water depths. It expresses in spectral form the conservation of action for individual wave packets (cf. G. B. Whitham [1967], F. P. Bretherton and C. J. R. Garrett [1968]) propagating along the rays in  $\mathbf{x}, \mathbf{k}$  phase space defined by eqs. (3.1.2).

Noting that  $\frac{\partial}{\partial x_i} (\dot{x}_i) + \frac{\partial}{\partial k_i} (k_i) = 0$  (eq. (3.1.2)), eq. (3.1.1) may be written in the equivalent form

$$\frac{DN}{Dt} \equiv \frac{\partial N}{\partial t} + \dot{x}_i \frac{\partial N}{\partial x_i} + k_i \frac{\partial N}{\partial k_i} = \frac{S}{\omega'} \quad (3.1.3)$$

which states that in the absence of an energy source  $S$  the action density remains constant along the path of a wave group in  $\mathbf{x}, \mathbf{k}$  space (Liouville's theorem, cf. R. Dorrestein [1960], G. E. Backus [1962]).

In applying (3.1.3) to the case of a narrow swell peak, we may integrate over the small region of wavenumbers representing the swell to yield a propagation equation for the total swell energy  $\mathcal{E}$ ,

$$\frac{\partial}{\partial t} \left( \frac{\mathcal{E}}{\omega'} \right) + \frac{\partial}{\partial x_i} \left( v_i \frac{\mathcal{E}}{\omega'} \right) = \frac{\Phi}{\omega'} \quad (3.1.4)$$

where  $\Phi = \int S d\mathbf{k}$  and the swell frequency  $\omega'$  was taken as constant in the integration.

In the particular case in which all fields are homogeneous with respect to  $y$ , the currents vanish, and the frequency remains constant, eq. (3.1.4) reduces (after multiplying by  $\omega'/v_x$  and noting that  $\partial v_x / \partial t = 0$  for  $\omega = \text{const}$ ) to the simple form

$$\frac{DI}{Dx} \equiv \frac{1}{v_x} \frac{\partial I}{\partial t} + \frac{\partial}{\partial x} I = \Phi \quad (3.1.5)$$

where  $D/Dx$  represents the total derivative with respect to the normal-to-shore coordinate  $x$  taken along the propagation path of the swell – i.e. with  $dt = \frac{1}{v_x} dx$ ,  $dy = \frac{v_y}{v_x} dx$  (the latter variable is irrelevant in the present context, however).

The routine analysis of our swell data was based on the idealized energy flux equation (3.1.5). However, integrations of the exact equation (3.1.4) were also carried out for a number of special cases, using a general ray refraction routine which included spatial and temporal variations of both currents and water depths. The errors incurred in (3.1.5) through neglect of currents, tidal variations of water depth and slow changes of the swell frequency were found to be negligible. Significant deviations from the  $y$ -independent case arose, however, through the local focusing caused by lateral variations of the bottom topography. The modifications were found to be highly sensitive to small variations of the swell frequency and direction and were virtually impossible to model deterministically (Section 3.4).

### 3.2. Attenuation Due to Bottom Friction

In the generation study (Part 2), the source function in the energy balance equation was determined empirically by differentiating the observed spectral fields. We adopt here the inverse procedure and integrate the energy flux equation (3.1.5), assuming a particular form for the source function. The theoretical model can then be tested by comparing the predicted with the observed spectra. This approach avoids the inaccuracies of experimental differentiation, but is feasible only if the source functions and spectra are sufficiently simple to permit a straightforward numerical integration. In the present case, the simplicity stems from the narrow peak approximation and our preconceptions regarding the structure of the source function (which will be found subsequently to need revision).

It is generally assumed that the attenuation of swell propagating in shallow water is caused by bottom friction. Wave tank measurements (J. A. Putnam and J. W. Johnson [1949], R. P. Savage [1953], K. Kajiura [1964], Y. Iwagaki et al. [1965]) and – to a lesser extent – field data (C. L. Bretschneider and R. O. Reid [1954], H. Walden and H. J. Rubach [1967], K. Hasselmann and J. I. Collins [1968]) support the usual assumption that the tangential stress  $\tau_b$  acting on the ocean bottom can be modelled approximately by a quadratic friction law

$$\tau_b = c_b \mathbf{U} |\mathbf{U}| \quad (3.2.1)$$

where  $\mathbf{U}$  denotes the current immediately outside the thin turbulent boundary layer at the bottom and  $c_b$  is a drag coefficient, which in the ocean is generally of order  $10^{-2}$ .

K. Hasselmann and J. I. Collins [1968] have shown that a friction law of the form (3.2.1) implies a quasi-linear source function (cf. eq. (2.1.1))

$$S = S_{bf}(\mathbf{k}) = -v_{ij} k_i k_j F(\mathbf{k}) \quad (3.2.2)$$

in which the coefficient  $v_{ij}$  represents a kinematic viscosity tensor given by

$$v_{ij} = \frac{g c_b}{\omega^2 \cosh^2 kH} \left\{ \delta_{ij} \langle |\mathbf{U}| \rangle + \frac{\langle U_i U_j \rangle}{|\mathbf{U}|} \right\}. \quad (3.2.3)$$

The expressions in cornered parentheses denote ensemble averages and can be computed from the known Gaussian distribution of the currents.

Substituting eqs. (3.2.2) and (3.2.3) in (3.1.1) and integrating over the swell peak, we obtain the net source function

$$S_{bf} = - \frac{g c_b k^2 \mathcal{E}}{\omega^2 \cosh^2 kH} \left( \langle |\mathbf{U}| \rangle + \frac{\langle U_{||}^2 \rangle}{|\mathbf{U}|} \right) \quad (3.2.4)$$

where  $U_{||}$  denotes the component of  $\mathbf{U}$  parallel to the direction of wave propagation.

The above relations apply for an arbitrary bottom current  $\mathbf{U} = \mathbf{U}^w + \mathbf{U}^c$  consisting of a superposition of the wave orbital velocity  $\mathbf{U}^w$  and a mean current  $\mathbf{U}^c$ . In most of our swell cases, the wave orbital velocities varied within the range 0.1–5 cm/s, whereas the tidal currents were typically of order 20–40 cm/s. Hence to a good approximation the expectation

values on the right hand side of eq. (3.2.4) may be replaced by the appropriate expression for the mean current.

Assuming constant  $U^c$  along a ray, the flux equation (3.1.5) can then be readily integrated to give

$$\ln I = c_0 g V \xi \tag{3.2.5}$$

where

$$V = |U^c| + (U^c_x)^2 / |U^c| \tag{3.2.6}$$

and

$$\xi = \int_x^{\infty} \frac{k^2}{\omega^2 v_x \cosh^2 kH} D x. \tag{3.2.7}$$

According to (3.2.5) the energy flux  $I$  decays exponentially with respect to the normalized distance coordinate  $\xi$  at a rate proportional to the current factor  $V$ .

3.3. Energy Flux Analysis of Swell Data

Ten distinct swell cases were investigated (Table 3). For each swell case, the decay of the energy flux  $I$  with respect to the normalized distance  $\xi$  was computed for a sequence of rays at four-hourly intervals, Figs. 3.2a-j (to avoid congestion, only every second or third decay curve is shown in some of the figures). The points on the curves correspond to station positions, the flux values at the times corresponding to the transition of the rays through the stations being obtained by interpolating between the four-hourly measurements at each station. The origin of  $\xi$  is chosen at Station 1, and the coordinate increases with distance  $x$  offshore. Due to the  $\cosh^{-2} kH$  weighting factor in the definition (3.2.7), most of the change in  $\xi$  occurs in the shallow water close to shore, resulting in a more or less linear increase of  $\xi$  with respect to station number.

Table 3  
Swell Cases  
(No. of independent spectra: 678-24 = 654)

Swell Case	Start Time	End Time	No. of Spec-tra	No. of Rays (4 hr. sequ.)	$f$	$\delta f$	$\theta$	$I_{in}$	$\Gamma \cdot 10^3$
1	1968 12 <sup>h</sup> Sep. 8		12	2	10 <sup>-3</sup> Hz 89	10 <sup>-3</sup> Hz 14-17	deg 107	m <sup>3</sup> s <sup>-1</sup> 2·10 <sup>-2</sup>	m <sup>2</sup> s <sup>-3</sup> 160
	09 <sup>h</sup> Sep. 24	23 <sup>h</sup> Sep. 24	24	3	86-91	10-17	120	10 <sup>-1</sup>	45
	09 <sup>h</sup> Sep. 24	23 <sup>h</sup> Sep. 24	37	4	88-102	10-16	120	10 <sup>-1</sup> -2·10 <sup>-1</sup>	80
4	1969								
	04 <sup>h</sup> Jul. 4	02 <sup>h</sup> Jul. 5	36	5	78-98	10-17	120	10 <sup>-1</sup> -2·10 <sup>-1</sup>	49
	20 <sup>h</sup> Jul. 14	22 <sup>h</sup> Jul. 16	142	13	102-116	10-20	130	2·10 <sup>-2</sup> -4·10 <sup>-2</sup>	34
	12 <sup>h</sup> Jul. 22	14 <sup>h</sup> Jul. 23	80	7	77-120	6-15	141	5·10 <sup>-3</sup> -2·10 <sup>-2</sup>	1.9
	04 <sup>h</sup> Jul. 26	22 <sup>h</sup> Jul. 26	53	5	119-137	9-16	138	3·10 <sup>-1</sup>	89
	10 <sup>h</sup> Jul. 27	09 <sup>h</sup> Jul. 30	179	17	68-98	8-16	99	10 <sup>-2</sup> -5·10 <sup>-1</sup>	27
	15 <sup>h</sup> Aug. 2	02 <sup>h</sup> Aug. 4	56	8	87-101	8-15	120	10 <sup>-3</sup> -3·10 <sup>-3</sup>	43
	08 <sup>h</sup> Aug. 9	19 <sup>h</sup> Aug. 10	59	9	80-92	6-14	120	5·10 <sup>-4</sup> -10 <sup>-3</sup>	30

Total: Total:
678 73
Mean:
38

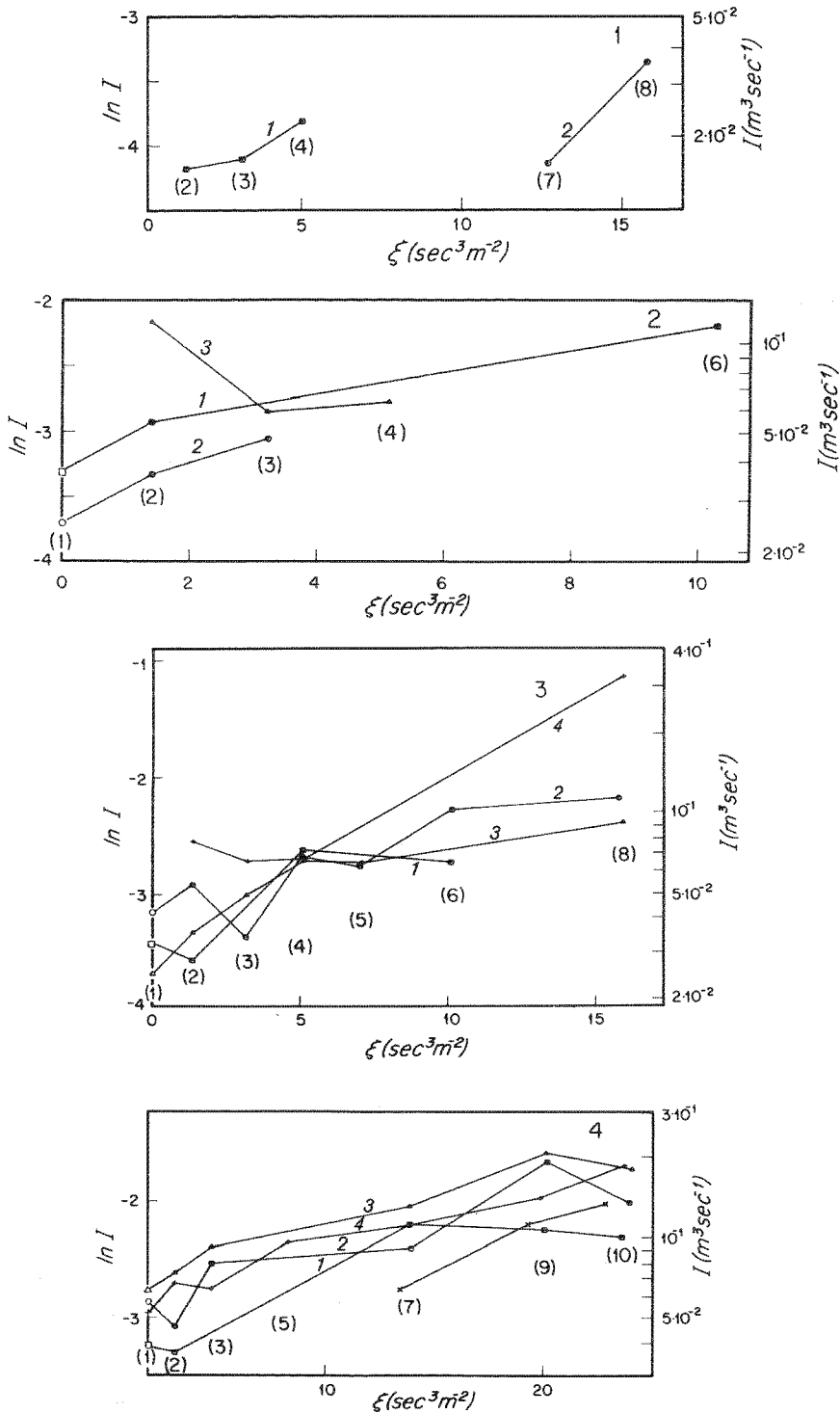


Fig. 3.2 a-d. Energy flux  $I$  as function of normalized propagation distance  $\xi$  along rays for swell cases 1-10. Series of rays separated for hours in time was analysed for each swell case. Numbers on the curves refer to the particular ray in the sequence. Station numbers are given in parentheses

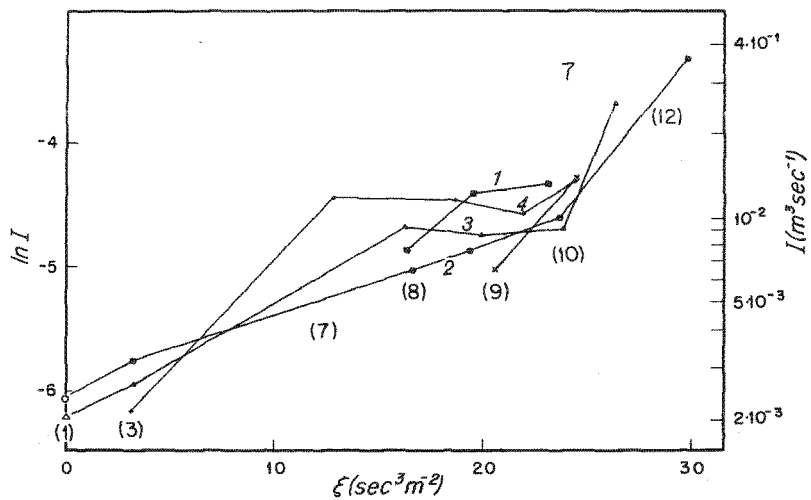
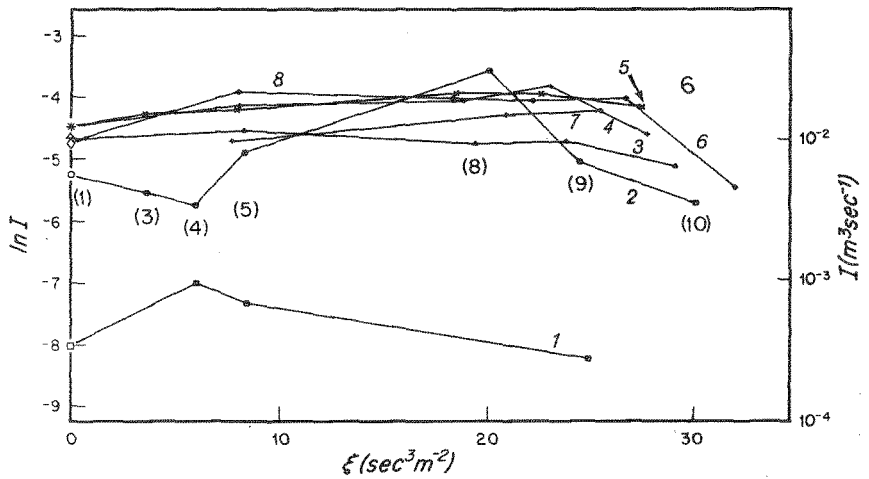
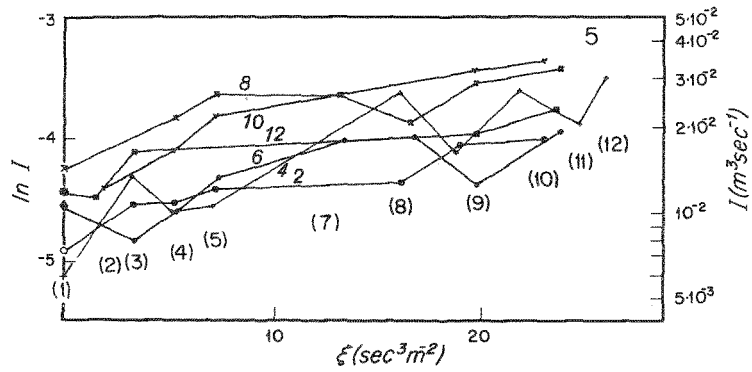


Fig. 3.2 e-g. Same as Fig. 3.2 a-d

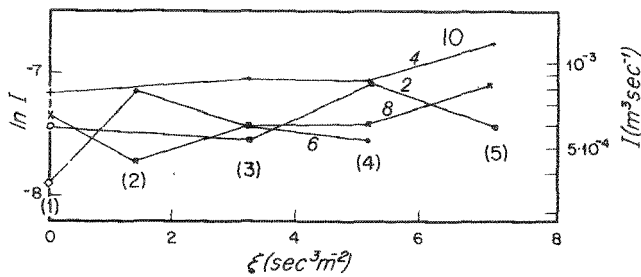
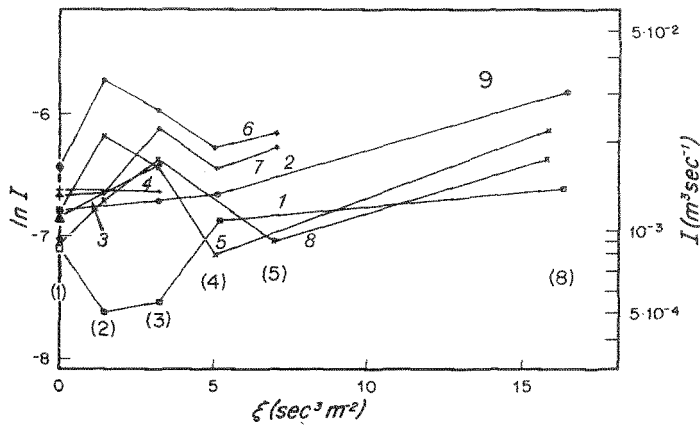
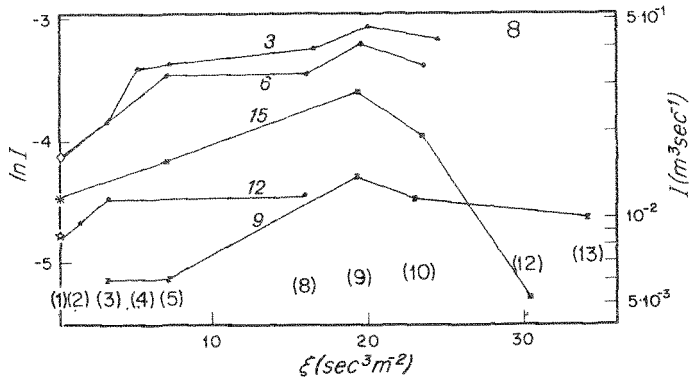


Fig. 3.2 h-j. Same as Fig. 3.2 a-d

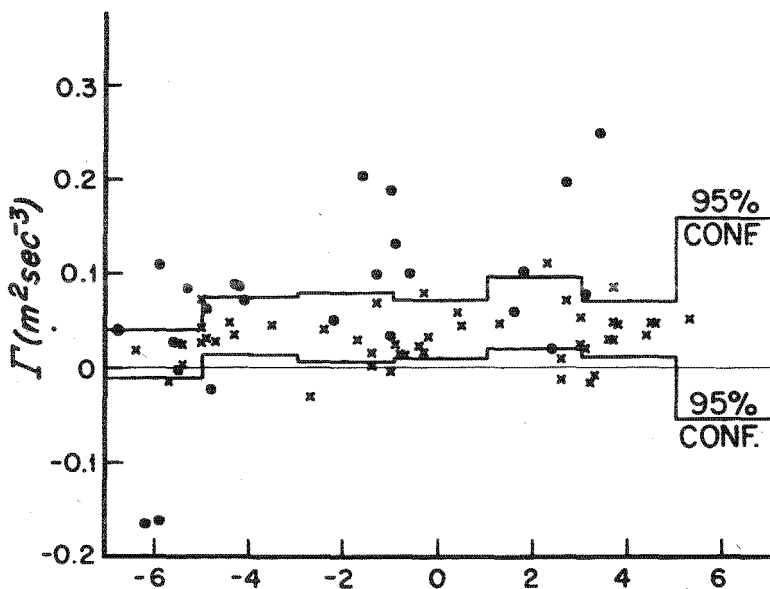
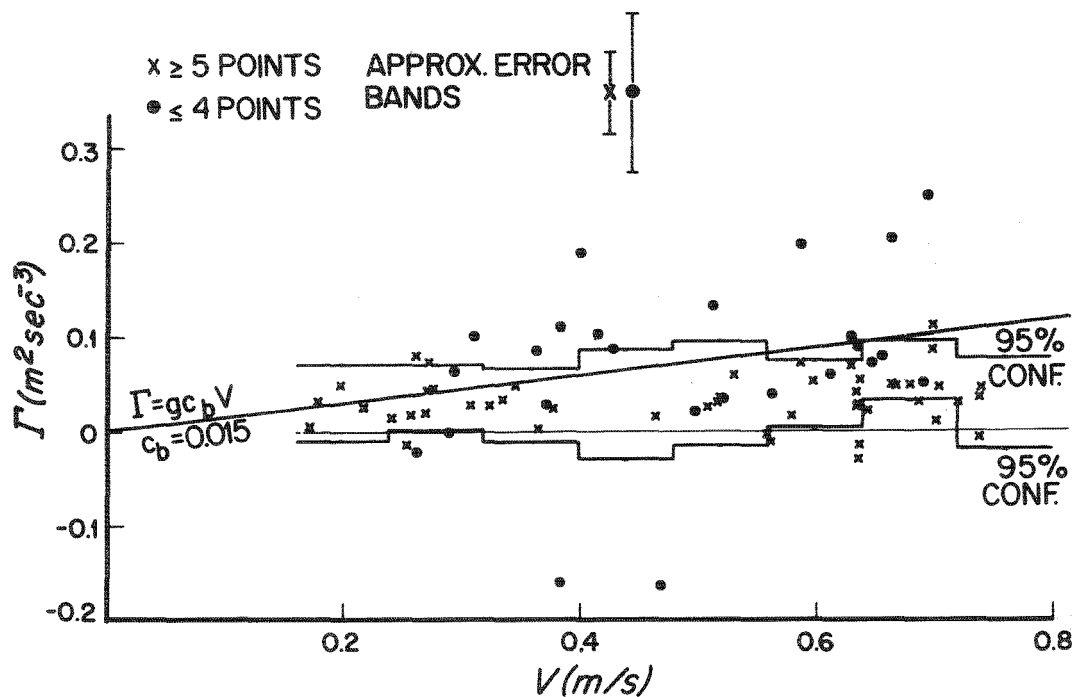


Fig. 3.3 a,b. Decay parameter  $\Gamma$  versus current parameter  $V$  and phase of tide. Data are divided into two classes  $\times$ ,  $\bullet$  depending on number of energy flux measurements / available to define the mean slope  $\Gamma$  (eq. (3.3.1)). Stepped lines denote 95% confidence limits for mean values of  $\Gamma$  in finite abscissa segments



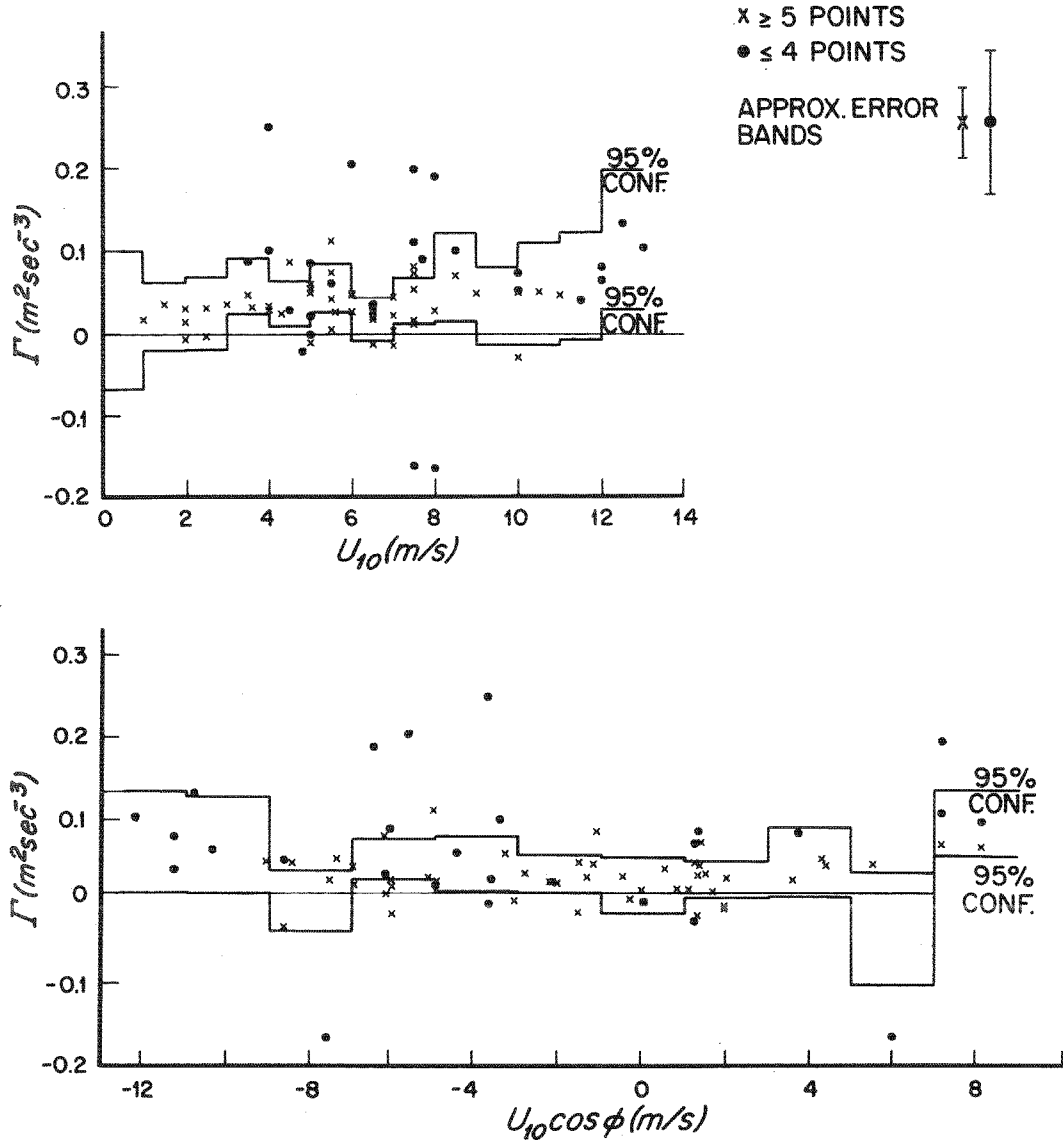


Fig. 3.4 a,b. Decay parameter  $\Gamma$  versus wind speed and component of wind velocity parallel to swell propagation direction. Data are divided into two classes  $\times$ ,  $\bullet$  depending on number of energy flux measurements / available to define the mean slope  $\Gamma$  (eq. (3.3.1))

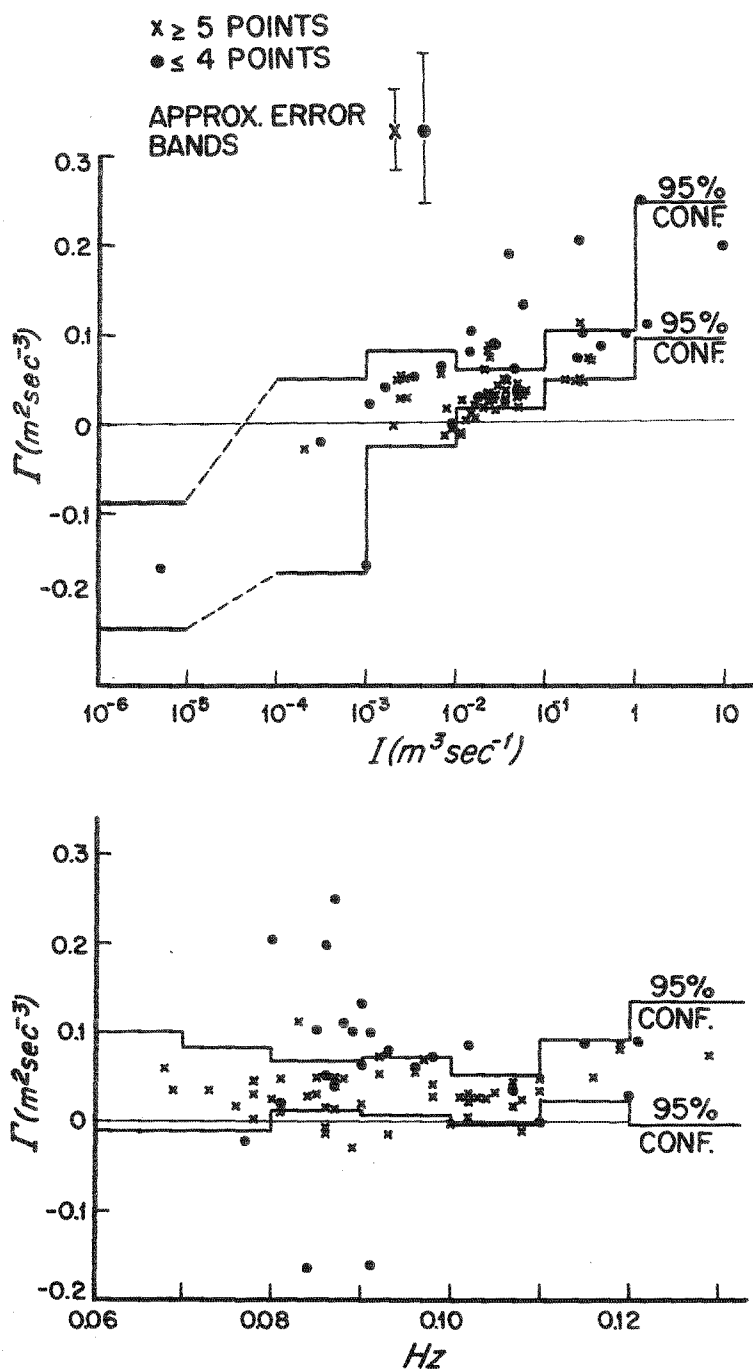


Fig. 3.5 a,b. Decay parameter  $\Gamma$  versus swell frequency and energy flux. Data are divided into two classes  $\times$ ,  $\bullet$  depending on number of energy flux measurements / available to define the mean slope  $\Gamma$  (eq. (3.3.1) )

To each decay curve a straight line was fitted by least squares. According to eq. (3.2.5), the slopes of the lines

$$\Gamma = \frac{d \ln I}{d \xi} \quad (3.3.1)$$

should be equal to  $c_b g V$ , so that a marked time variation was to be expected through the dependence on the time varying current factor  $V$ . However, a cursory inspection of Figs. 3.2a-j does not reveal an obvious tidal periodicity.

This is borne out by the plot of the set of all computed  $\Gamma$  values against  $V$ , Fig. 3.3a, which shows no dependence of  $V$  on  $\Gamma$ , as predicted by (3.2.5). The values of  $V$  were inferred for Station 8 from tidal current charts, which were found generally to give a good approximation to the measured currents. Errors incurred by assuming a constant current along the ray were also relatively small. The lines represent 95% confidence bands for the average values of  $\Gamma$  defined for separate 5 cm/s segments of the  $V$  axis. The statistical basis of these estimates is described in the Appendix. (Note that the r.m.s. error for the average within a segment is considerably smaller than for the individual estimate of  $\Gamma$ , as is apparent by the narrowness of the band.)

A general test of tidal influences on the decay rates, independent of the particular mechanism assumed, is provided by the plot of  $\Gamma$  against the phase of the tide, Fig. 3.3b. The time axis represents the time lag of the arrival of the swell at Station 1 relative to the nearest high tide in Helgoland (a convenient reference point in the vicinity of the profile - cf. Fig. 2.2 - for which published tide tables exist). The representation is meaningful only if the tides are predominantly semidiurnal, but this is the case. Again, no tidal modulation is apparent.

Figures 3.4a, b indicate that the swell decay rate is also essentially independent of the local wind speed and the component of the wind velocity parallel to the propagation direction of the swell. A dependence on these variables may have been anticipated either directly through air-sea interactions or indirectly through the (WKBj-type) coupling between the swell and the shorter wind-wave components (O. M. Phillips [1963], K. Hasselmann [1971]). However, neither process appears to be important in the present situation.

Finally, the dependence of the decay rate on the swell parameters themselves was investigated. No systematic variation was found with the swell propagation direction (cf. Table 3) or the swell frequency (Fig. 3.5a). However, there is some indication of an increase of the decay rate with the swell energy or, equivalently, the energy flux  $I$  (Fig. 3.5b). Despite the apparent limitations of the bottom friction model, it is perhaps of interest that the enhanced decay rates for  $I \geq 1 \text{ m}^3 \text{ s}^{-1}$  are consistent with this theory. For  $I = 1 \text{ m}^3 \text{ s}^{-1}$  the r.m.s. orbital velocity  $U^w$  near the bottom is of the order 10-20 cm/s, and since this is comparable with the tidal currents  $U^c$ , the approximation  $U^w \ll U^c$  leading to equations (3.2.5), (3.2.6) is no longer valid. The inclusion of the orbital velocities increases the value of the expression ( $\langle |U| \rangle + \langle U^2/|U| \rangle$ ) on the right hand side of (3.2.4) and thereby the attenuation factor  $\Gamma$ . For  $I \approx 10 \text{ m}^3 \text{ s}^{-1}$ ,  $\Gamma$  is enhanced by a factor of approximately 2, as observed.

### 3.4. Lateral Variations of Bottom Topography

Our analysis of the attenuation parameter  $\Gamma$  in the previous section was based on the  $y$ -independent energy flux equation (3.1.5). Lateral variations of the depth modify these results in two ways. Firstly, the normalized distance  $\xi$ , as defined by eq. (3.2.7), is no longer a unique function of  $x$ , since different depth profiles correspond to different ray paths. Computations of  $\xi$  using the true bottom topography and ray paths for a number of swell cases indicated that the errors induced in  $\Gamma$  in this manner were generally less than 20%. Secondly, the flux equation (3.1.5) itself is no longer strictly valid. The missing lateral energy flux terms (in addition to time dependent variations) are taken account of formally in the

general action balance equation (3.1.4). However, the straightforward application of (3.1.4) is restricted to regions in which the rays do not intersect. In practice it was found that in nearly all the cases computed the profile was intersected by at least one caustic and that the ray theory therefore needed to be generalized to allow for multiple sheets in the  $x, y$  plane. Although this is feasible in theory, it was found, in practice, that the caustics were produced by small scale irregularities of the bottom topography and their locations varied unstably with small changes in frequency and propagation direction of the swell.

Apart from the position of the caustics, the ray integrations revealed generally that most of the variability of the energy flux was induced by small scale topographic features and was virtually impossible to predict deterministically. The predominance of small scale features is illustrated in Fig. 3.6, which shows examples of depth sections along the profile and along a ray through Station 8 at an incident angle of  $34^\circ$  to the profile.

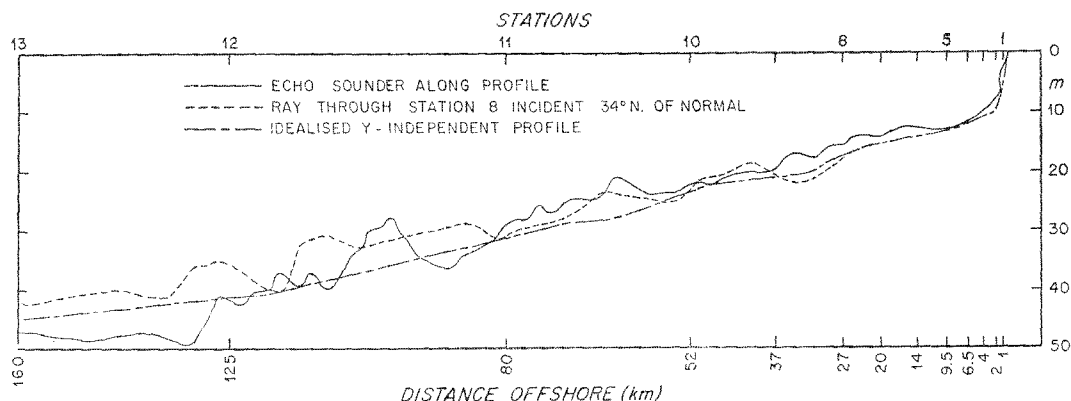


Fig. 3.6. Bottom depths along wave array (echo sounder) and a ray through Station 8 (computed from depth charts). The mean depth profile assumed in the parallel-bottom-contour calculation is also shown

A comparison of typical sets of rays computed for the idealized case of parallel bottom contours and the true bottom topography are shown in Fig. 3.7. It is apparent that small local perturbations can produce significant changes in the ray pattern at large distances from the disturbances.

According to elementary ray theory, a depth perturbation  $-\delta H$  of dimensions  $L_\perp$  orthogonal to and  $L_\parallel$  parallel to the direction of wave propagation will produce focusing at a distance

$$R \approx \frac{1}{2} \frac{L_\perp^2 \sinh(2kH)}{L_\parallel k \delta H} \quad (3.4.1)$$

behind the disturbance. For a wavelength of 150 m (period  $\approx 10$  s) and typical values (see cf. Fig. 3.6)  $\delta H = 2$  m,  $L_\perp = L_\parallel = 4$  km,  $H = 15$  m, we obtain  $R \approx 30$  km. Closer to shore, the focusing distances are generally smaller due to the reduced value of the factor  $\sinh(2kH)$ . Thus it appears that the observed variability of the energy fluxes in Figs. 3.2a-j can be explained qualitatively by the convergence and divergence of rays due to small scale bottom irregularities. (A similar mechanism was suggested as the origin of the variability of the spectral parameters observed in the generation study, Part 2.)

An attempt was made to detect a possible systematic mean modification of the energy flux superimposed on these fluctuations by computing the refraction patterns for a smoothed bottom topography. Fig. 3.8 shows typical energy fluxes computed from the ray patterns for a bottom topography in which all scales smaller than 10 km were filtered out. The source

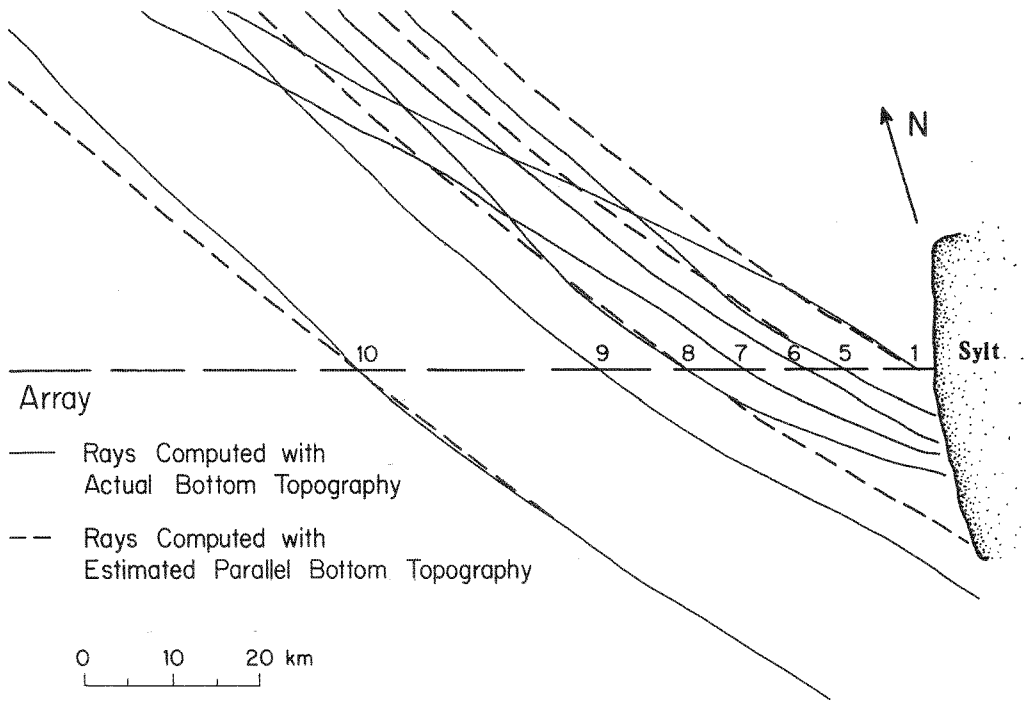


Fig. 3.7. Rays computed for the true bottom topography and the parallel bottom-contour approximation (0.08 Hz)

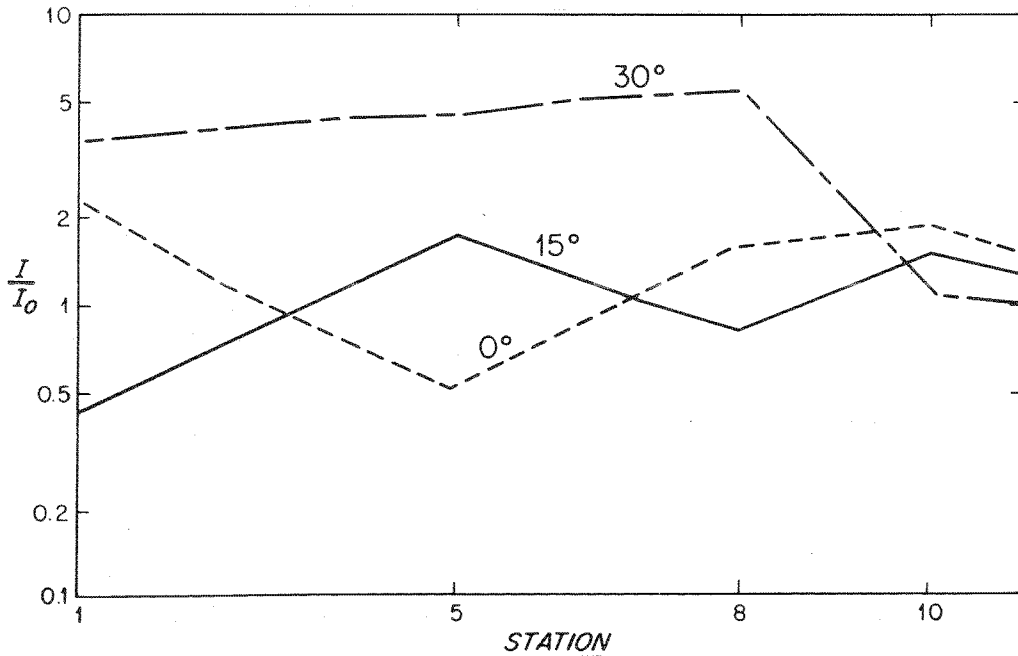


Fig. 3.8. Variations in energy flux  $I$  computed for a smoothed bottom topography (compared against the constant flux  $I_0$  for the case of parallel bottom contours)

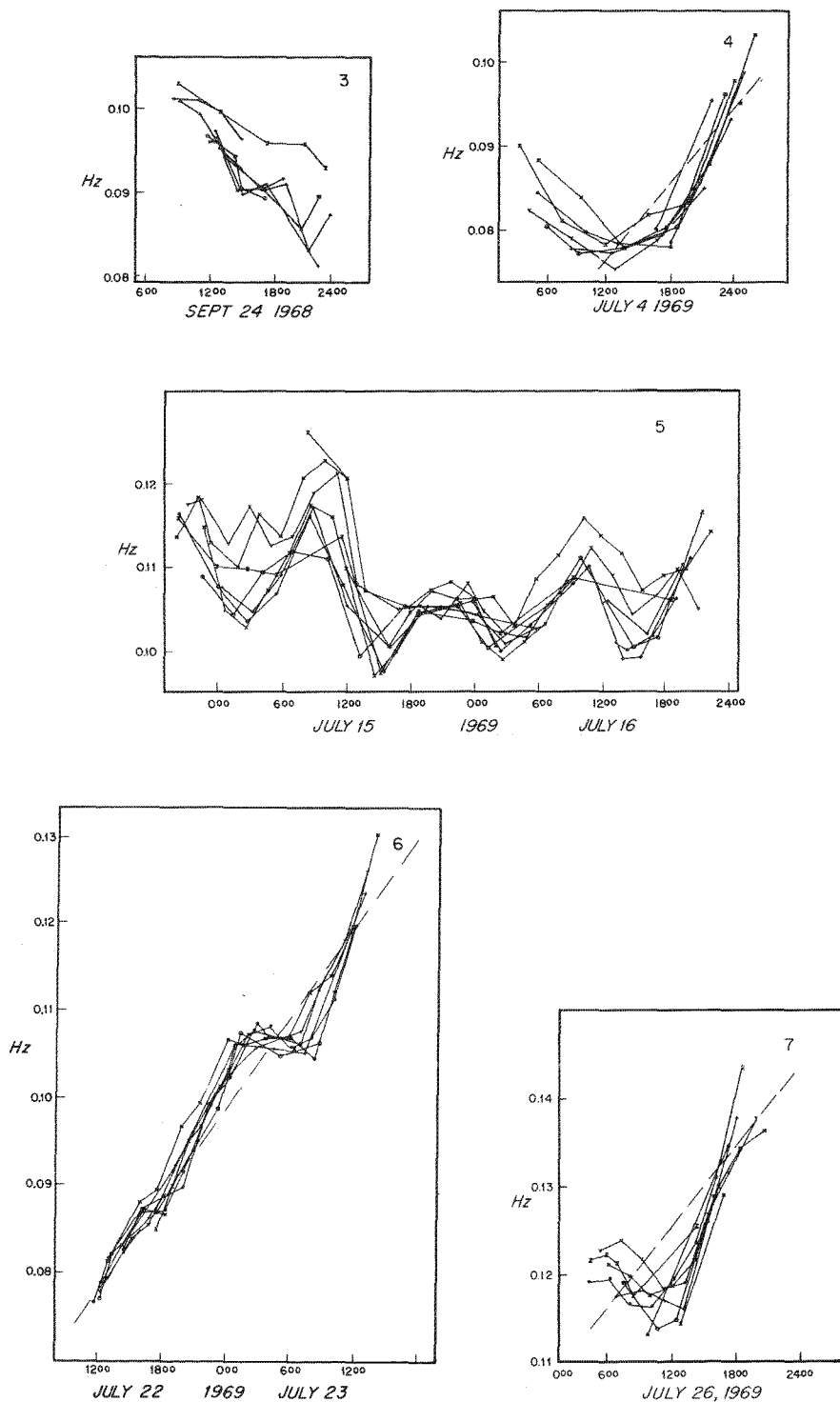


Fig. 3.9 a-e. Mean swell frequencies versus time for swell cases 3-10. Tidal modulation of this frequency bandwidth for swell case 8. Different curves correspond to different stations

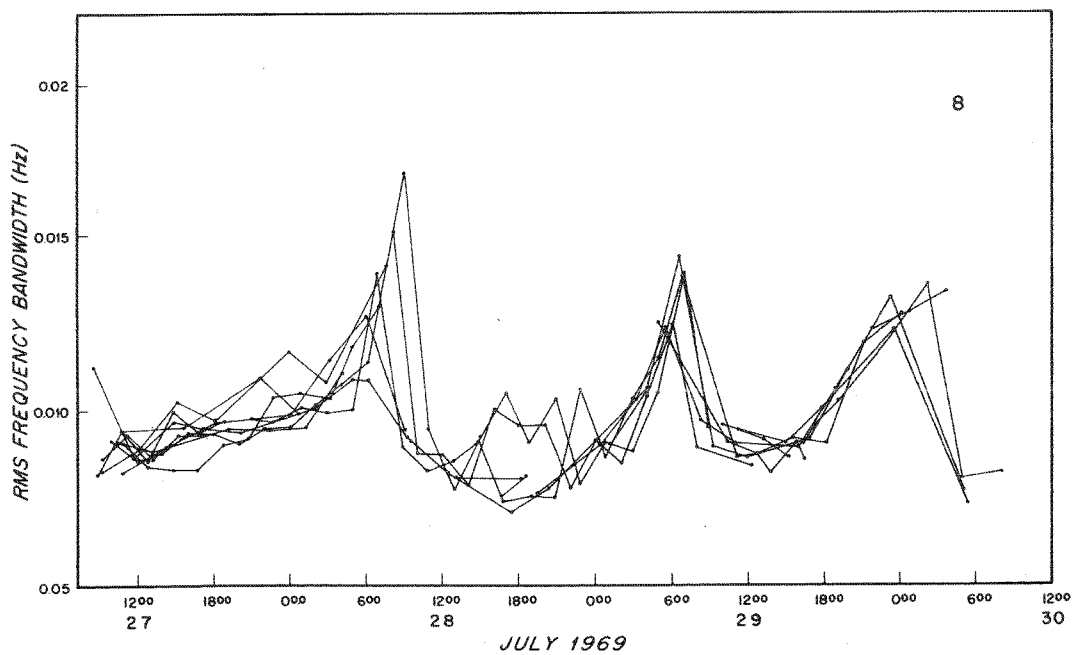
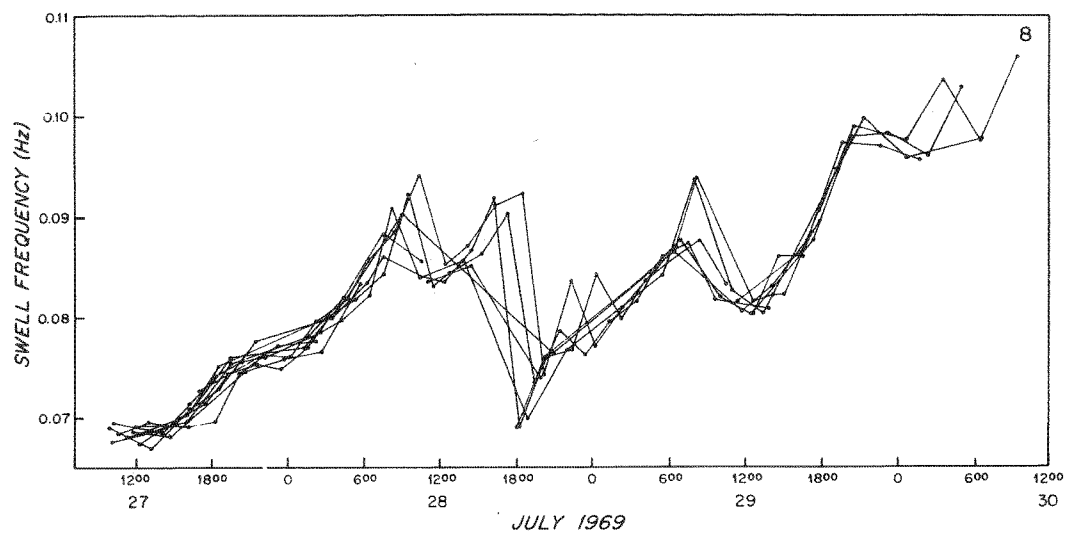


Fig. 3.9 f.g. Same as Fig. 3.9 a-e

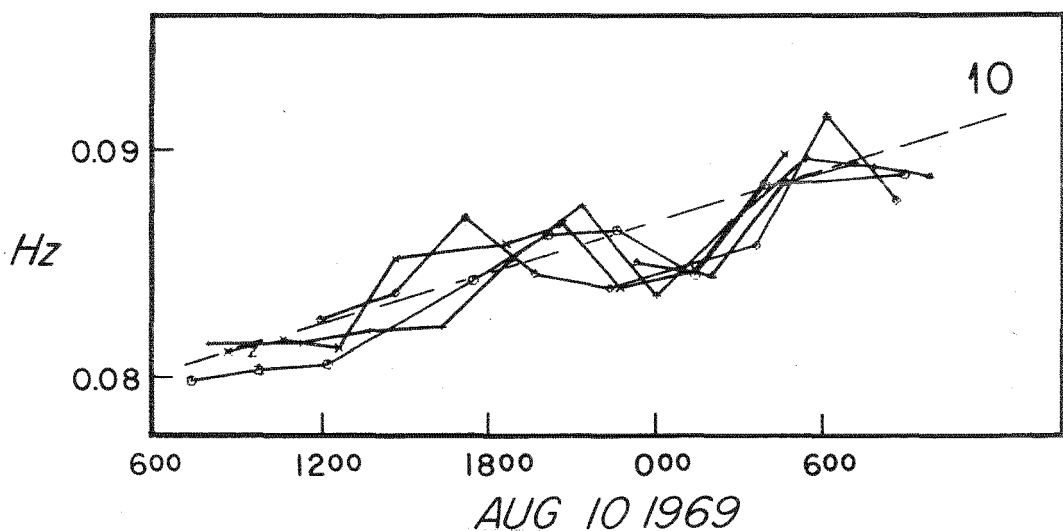
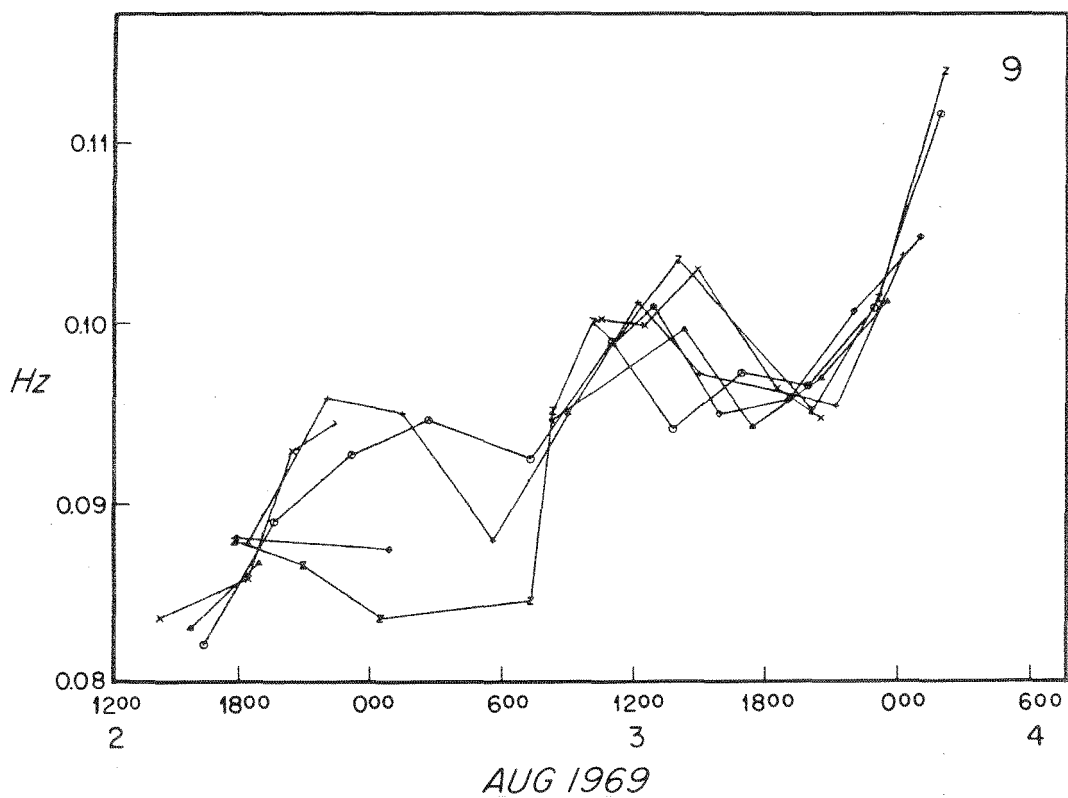


Fig. 3.9 h,i. Same as Fig. 3.9 a-e



function was taken as zero, so that variations of  $I$  are due entirely to lateral inhomogeneities. The values still fluctuate considerable from station to station and change randomly with propagation direction. Corresponding curves for neighbouring frequencies also differed appreciably. Although in this case no caustics occurred, it appears that the refraction pattern is still dominated by relatively short topographic features of scale slightly larger than the cut-off applied by the filter. A systematic dependence of the energy flux with respect to station number, direction of propagation or frequency could not be detected.

The observed energy fluxes (Figs. 3.2a–j) generally exhibit smaller variability than Fig. 3.8 – which applies to a monochromatic wave field – would lead one to expect. Presumably, the flux values for a real swell field should be obtained by integrating the monochromatic fluxes over a finite band of frequencies and propagation directions, which averages out some of the variability.

Similar conditions of random refraction may apply generally in continental-margin areas, in which the scale of the topographic features are usually small compared with the propagation distances over which the swell can interact significantly with the bottom.

### 3.5. Dispersion Characteristics

In their original study of swell off the coast of Cornwall, N. F. Barber and F. Ursell [1948] observed a characteristic linear increase of the swell frequencies with time which they explained in terms of a singular-event model. If the space-time region in which the swell is generated is small compared with the swell propagation distances and times, the source can be approximated by a  $\delta$ -function. Accordingly, only those swell components will be observed by an observer at distance  $D$  from the source for which  $D = \text{group velocity} \times \text{travel time}$ , or

$$f = \frac{g(t - t_0)}{4\pi D} \quad (3.5.1)$$

where  $t_0$  is the time of origin of the swell.

W. H. Munk and F. E. Snodgrass [1957], W. H. Munk, G. R. Miller, F. E. Snodgrass et al. [1963], F. E. Snodgrass et al. [1966], D. E. Cartwright [1971], and others have applied (3.5.1) to determine the distances and time of occurrence of swell sources, in general finding excellent agreement with expected source regions as determined from weather maps. The investigations were concerned with relatively long-period swell, normally in the 12–20 second range, originating in storms at great distances – in some cases exceeding half the circumference of the earth.

In the present study, direct access to the open ocean was restricted to the small northern opening of the North Sea. The longest available wave path, from the east coast of Greenland, was only 3000 km, but even this was limited to the  $10^\circ$  window between Iceland and Scotland. Consequently, most of the swells observed were generated rather near to the wave stations, and the dimensions of the source regions were normally not significantly smaller than the swell propagation distances. Moreover, all swell periods lay in the range between 7 and 15 s (frequently near 12 s), indicating that the swells were generated by rather moderate winds (10–23 m/s), which normally persist locally for longer periods than intense storms. Both factors combined to make the application of the usual  $\delta$ -event model questionable in many of our swell cases. Accordingly, the frequency histories shown in Figs. 3.9a–i often reflect the space-time evolution of the generation region as strongly as dispersion effects, and the relation (3.5.1) cannot be applied in a straightforward manner to determine the origin of the swell. However, by considering the propagation characteristics of the waves in conjunction with the weather maps, the various swell sources shown in Fig. 3.10 and their “case histories” could be reconstructed with some confidence.

Swell cases 4, 6 and 7 could be approximated by the  $\delta$ -event model. The time origins and distances inferred from (3.5.1) were identified on the weather maps with rather localized, short-lived regions of high winds directed towards Sylt. Case 1 probably also belongs to this

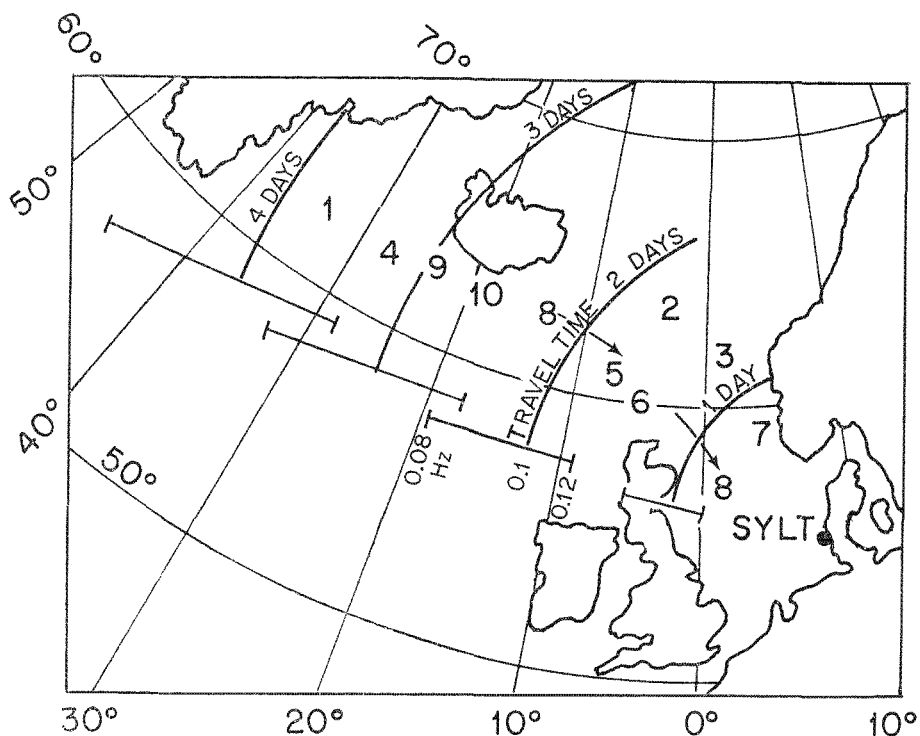


Fig. 3.10. Swell sources as inferred from weather maps and wave propagation times

category, but the swell was observed too briefly to determine the dispersion rate. The same restriction applies to swell case 2.

Swell cases 8, 9 and 10 show positive dispersion, but here the source distances inferred from (3.5.1) were either impossible ( $> 3000$  km, cases 8 and 10) or not consistent with the weather maps (case 9)\*. However, in these cases the observed dispersion could be explained naturally by the spatial and time dependence of less distant generating regions identified on the weather charts. For example, during the swell period 8 – the longest observed – the suspected generation region gradually wandered from south-east of Iceland into the northern part of the North Sea, weakening as it moved. Thus the high-frequency components generated later but nearer to the wave stations dominated over the swell components generated earlier at greater distances. The net effect was an anomalously slow frequency increase with time. Similar explanations apply to swell cases 9 and 10.

Conversely, the negative frequency trend of swell case 3 was attributed to a gradual increase of the wind strength in a fairly stationary generation region west of Norway. Swell case 5, finally, was associated with a stationary wind system north of Scotland. The narrowness of the swell peaks shown for this case in Fig. 3.1 were apparently not caused by dispersion, but simply reflect the peakedness of the spectrum in the generating region. Consistent with this interpretation, the ratios peak-width to peak-frequency are seen to be approximately the same for both the swell peaks and the higher-frequency, locally generated regions of the spectra.

Swells which persisted for a day or longer exhibited a pronounced semi-diurnal modulation of the frequency. N. F. Barber and F. Ursell [1948] first noted this effect and attributed it

\* Reflections off Greenland or Iceland in cases 8 and 10 were also inconsistent with the weather maps.

to the Doppler shift by tidal currents. Changes in the swell frequency are governed by the equation (cf. eq. (3.1.2))

$$\frac{D\omega}{Dt} = \frac{\partial\Omega}{\partial t} = k \cdot \frac{\partial U}{\partial t}$$

where the left hand side represents differentiation along the path of a wave group. In most cases, the swell travel time was of the same order as a tidal cycle, so that  $\Delta\omega \approx k \cdot \bar{U}$ , where  $\bar{U}$  is the mean tidal current. Taking  $k \approx \frac{2\pi}{150} \text{ m}^{-1}$  and  $\Delta\omega \approx 2\pi \times 0.003 \text{ s}^{-1}$  we obtain  $\bar{U} \approx 0.5 \text{ m/s}$ , which is a reasonable value for the North Sea. Interestingly, the frequency bandwidth of the swell peak often exhibits a stronger tidal modulation than the peak frequency itself, cf. Fig. 3.9g.

### 3.6. Conclusions

We have not been able to identify clearly the mechanism of swell attenuation. Interpreting the mean decay rate  $\Gamma = 0.04 \text{ m}^2 \text{ s}^{-3}$  in terms of a bottom friction model, assuming the usual quadratic stress relation, and taking a mean value 25 cm/s for the current parameter  $V$ , we obtain a drag coefficient  $c_b = 0.015$ . This is consistent with previous estimates. However, the theory predicts a linear dependence of the decay rate on  $V$ , which was not observed. Nor could a tidal modulation of the decay rate be detected. Although the quadratic friction law can undoubtedly only be regarded as a crude approximation of the dissipative processes in a non-stationary turbulent boundary layer, it appears improbable that the swell decay rate should be virtually independent of the rather strong tidal currents if bottom friction is indeed the dominant decay mechanism.

The search for correlations with other parameters was equally unsuccessful. Neither the wind speed nor the component of the wind velocity parallel to the direction of wave propagation affected the decay rate. No dependence was found on the swell frequency or propagation direction. However, there was a marginal indication of an increase of the decay rate with the swell energy.

Theoretical considerations rule out wave-wave interactions (K. Hasselmann [1963b]) or interactions with turbulence outside the bottom boundary layer (K. Hasselmann [1968]) as significant mechanisms of swell attenuation. Recalling that F. E. Snodgrass et al. [1966] observed no measurable attenuation of Pacific swell over distances of many thousand kilometers, and that the strongest decay rate in the present study was observed close to shore, some form of bottom interaction still appears the most likely candidate. Although improbable, it is conceivable that the interactions with the mean current in the bottom boundary layer are such that the rate of wave energy dissipation happens to turn out independent of the mean current – despite the fact that the mean current greatly exceeds the wave orbital velocities. A more attractive alternative is backscattering due to Bragg interactions with bottom irregularities of scale comparable with the wavelength of the swell. Recent computations by R. Long [1972] indicate that bottom “waves” in this wavelength range of only 10–20 cm r.m.s. amplitude would be adequate to explain the observed attenuation. However, detailed spectral measurements of the bottom topography and the separation of the incident and backscattered components of the swell field, both of which were not carried out in the present study, are needed to test this hypothesis.

With respect to swell kinematics, classical dispersive swell systems generated by distant storms appear to be the exception rather than the rule in the North Sea. The frequency histories of most swells were characterised by signatures impressed by the particular space-time structure of the generating wave fields.

Variations of the swell energy by factors of two or more are common and can be understood through the ray focusing caused by lateral inhomogeneities of the bottom topography. The refracting features are generally of relatively small scale; the cumulative

effect of many independent refractions produces a randomly scattered swell beam, in analogy with the scintillation of celestial objects seen through the atmosphere and other small-angle scattering problems (cf. V. I. Tatarski [1961], L. A. Chernov [1960]).

## Appendix

### Statistical Analysis of the Attenuation Parameter $\Gamma$

The least-square-error regression line through  $n$  measurements  $z_j \equiv \ln I_j$  at points  $\xi_j$ ,  $j = 1, \dots, n$  is given by

$$z = \Gamma (\xi - \bar{\xi}) + \bar{z} \quad (\text{A.1})$$

where

$$\Gamma = \overline{(z - \bar{z}) (\xi - \bar{\xi})} / \overline{(\xi - \bar{\xi})^2} \quad (\text{A.2})$$

and the over-bars denote mean values with respect to the ensemble of data points  $j = 1, \dots, n$ .

We make the standard assumption that errors in the estimate of  $\Gamma$  arise through errors in the variable  $\zeta_j = (z_j - \bar{z}_j) / (\xi_j - \bar{\xi}_j)$  with fixed  $\xi_j$ , and that the variance  $\sigma_\zeta^2 = \langle \zeta_j^2 \rangle$  of  $\zeta_j$  with respect to a hypothetical ensemble of repeated experiments is independent of  $j$ . In this case,  $\Gamma$  is approximately Gaussian for large  $n$  and the variance of  $\Gamma$  approaches

$$\sigma_\Gamma^2 = \sigma_0^2 / n \quad (\text{A.3})$$

where

$$\sigma_0^2 = \langle \zeta^2 \rangle / \overline{(\xi - \bar{\xi})^2}.$$

Eq. (A.2) was used to determine  $\Gamma$  for all swell rays  $k$ . In plotting these values  $\Gamma_k$  against various other parameters, such as the tidal current  $\bar{V}$ , the tidal phase, swell frequency, etc., the  $\Gamma_k$  data in separate segments of the parameter axes were combined into a single estimate

$$\bar{\Gamma} = \sum_{k=1}^m c_k \Gamma_k \quad (\text{A.4})$$

where  $k = 1, \dots, m$  refer to the  $m$  values in a given segment. The weights  $c_k$  were chosen to minimize the variance

$$\sigma_{\bar{\Gamma}}^2 = \langle (\bar{\Gamma} - \langle \bar{\Gamma} \rangle)^2 \rangle = \sum_{k=1}^m c_k^2 \langle (\Gamma_k - \langle \Gamma \rangle)^2 \rangle \quad (\text{A.5})$$

subject to the side condition

$$\sum_{k=1}^m c_k = 1. \quad (\text{A.6})$$

Substituting (A.3) in (A.5) (and replacing  $n$  now by  $n_k$ ) the minimal condition becomes

$$\delta \sum_{k=1}^m \frac{c_k^2 \sigma_0^2}{n_k} = 0$$

subject to (A.6), which has the solution

$$c_k = \frac{n_k}{\sum_{k=1}^m n_k}.$$

The variance of  $\bar{\Gamma}$  then becomes

$$\sigma_{\bar{\Gamma}}^2 = \frac{\sigma_0^2}{\sum_{k=1}^m n_k}. \quad (\text{A.7})$$

Eq. (A.7) was applied to compute the 95 % confidence limits shown in Figs. 3.3–3.5. On account of the repeated sum definitions (A.2) and (A.3),  $\bar{\Gamma}$  is fairly closely normal, and the 95 % confidence bandwidth is approximately equal to  $4\sigma_{\bar{\Gamma}}$ .

The quantity  $\sigma_0^2$  in (A.7) was estimated using (A.3). Multiplying the equation by  $n_k$ , replacing  $\langle \Gamma \rangle$  by the approximate value  $\bar{\Gamma}$ , and then summing over the  $m$  points of the interval, we obtain

$$m\sigma_0^2 \approx \sum_{k=1}^m n_k (\Gamma_k - \bar{\Gamma})^2.$$

This equation was then averaged over all intervals, yielding finally

$$\sigma_0^2 \approx \overline{\sigma_0^2} = \frac{\sum_{\text{intervals}} \left\{ \sum_{k=1}^m n_k (\Gamma_k - \bar{\Gamma})^2 \right\}}{\sum_{\text{intervals}} m}.$$

# Notation

		page
$a_i$	spectral parameter	42
$c_{10}$	drag coefficient	12
$C_{ij}$ (or $C$ )	co-spectrum of time-series $i$ and $j$	20
$c_b$	bottom friction coefficient	12
$c_{ad}, c_{hf}$	equivalent friction coefficients	41
$c_w$	drag coefficient corresponding to $\tau_w$	50
$c_w^{\min}$	minimal drag coefficient corresponding to $\tau_w^{\min}$	50
$D_{ij}, D_{ijk}$	coefficients in parametrical radiative transfer equation	54
$\mathcal{E}$	variance of surface displacement (total "energy" of the wave field)	38
$\tilde{\mathcal{E}}$	nondimensional variance ("energy") of surface displacement	38
$E(f)$	one-dimensional spectrum	20
$E_{PM}(f)$	Pierson-Moskowitz spectrum	32
$F(f, \theta)$	energy spectrum with respect to propagation direction $\theta$ and frequency $f$	19
$\hat{F}(\mathbf{k})$	two-dimensional wave spectrum with respect to wave number $\mathbf{k}$	40
$\hat{F}(\mathbf{k}, a_1, \dots, a_n)$	model spectrum containing $n$ free parameters $a_1, \dots, a_n$	54
$f$	frequency	11
$f', \tilde{f}, \hat{f}$	non-dimensional frequency parameters	28
$f_c$	out-off-frequency	41
$f_m$	frequency of spectral peak	15
$f_m, \hat{f}_m$	non-dimensional frequency of spectral peak	32
$H$	water depth	15
$I$	total shoreward energy flux	72
$\mathbf{k}$	$\mathbf{k} = (k_1, k_2)$ horizontal wavenumber vector	20
$k$	modulus of $\mathbf{k}$	20
$k_j, k_x$	wave number component $k_j, k_x$ averaged over directional distribution	20
$L_{\perp}, L_{\parallel}$	length dimensions orthogonal and parallel to the direction of wave propagation	82
$N_j, N$	$N_j = N(\mathbf{k}_j), N = N(\mathbf{k})$ particle-number or action density at wavenumber $\mathbf{k}_j, \mathbf{k}$	40
$n_f, n_a, n_{\tilde{\mathcal{E}}}$	exponents in power laws for $\hat{f}_m, \alpha$ and $\tilde{\mathcal{E}}$ versus non-dimensional fetch	38
$p$	exponent characterizing directional distribution	32
$Q_{ij}$ (or $Q$ )	quadrature spectrum of time series $i$ and $j$	20
$R$	coherence	21
$S, S'$	one-, two-dimensional source functions	27
$S_{bf}$	source function due to bottom friction	73
$S_{ds}$	source function representing dissipative processes	49
$S_{in}$	source function representing energy input from the atmosphere	49
$S_{nl}$	source function due to non linear, resonant wave-wave interactions	49
$S_i$	source function of parametrical radiative transfer equation	55
$s(f, \theta)$ , or $s(\theta)$	normalized angular distribution	20
$U_{10}$	wind velocity at 10 meters height above the sea surface	28
$U^c$	mean current at bottom	73
$U^w$	orbital velocity at bottom	73
$U(\mathbf{x}, t)$	current	72
$U_{\parallel}$	component of $U$ parallel to the direction of wave propagation	73
$\bar{U}$	mean tidal current	89

$u_*$	friction velocity	11
$V$	current parameter	74
$\bar{v}_i$	group velocity component averaged over directional distribution	27
$v$	$v = (v_1, v_2)$ group velocity	27
$v_m$	group velocity corresponding to frequency of spectral peak	37
$v_\alpha$	average group velocity in the frequency band used to define $\alpha$	55
$x$	(dimensional) fetch	11
$x', \hat{x}, \bar{x}$	nondimensional fetch parameters	11
$\alpha$	Phillip's equilibrium constant	32
$\beta$	exponential growth factor	52
$\gamma$	ratio of the maximal spectral energy to the maximum of the corresponding Pierson-Moskowitz spectrum	32
$\varepsilon_{ij}, \varepsilon_{afm}$	coupling coefficients in propagation equations for spectral parameters	54
$\xi$	normalized swell propagation distance	74
$\theta$	direction of wave propagation	20
$\theta_m$	mean direction of wave propagation	21
$\theta_s$	beam width defined in terms of pitch-roll directional spectrum	21
$\theta'_m, \theta'_s$	variables analogous to $\theta_m$ and $\theta_s$ for a pair of wave sensors	21
$\mathcal{G}$	time variable of characteristic coordinates	55
$\lambda, \lambda_m$	wavelength, wavelength at spectral peak	15
$\nu_{ij}$	kinematic viscosity tensor	73
$\rho_a$	density of air	27
$\rho_w$	density of water	40
$\sigma_a, \sigma_b$	left, right sided width of spectral peak	32
$\tau$	total momentum transfer across the air-sea interface	27
$\tau_{ad}$	momentum advected away by the wave field	41
$\tau_b$	tangential bottom stress	73
$\tau_{hf}$	net momentum transfer corresponding to the third (high frequency) lobe of the nonlinear source function $S_{n1}$	41
$\tau_{lf}$	net momentum transfer corresponding to the first (low frequency) lobe of the nonlinear source function $S_{n1}$	51
$\tau_{mf}$	net momentum transfer corresponding to the middle (negative) lobe of the nonlinear source function $S_{n1}$	51
$\tau_w$	net momentum flux from the atmosphere to the wave field	12
$\tau_w^{\min}$	lower bound of the momentum transfer from the atmosphere to the wave field	49
$\varphi_j, \varphi'_j$	functional, linear functional, derivative of $\varphi_j$	54
$\Omega$	dispersion relation	72
$\omega$	circular frequency in fixed coordinate system	72
$\omega'$	frequency in a reference system moving with the current $U(x, t)$	72

## References

- Backus, G. E., 1962: The effect of the earth's rotation on the propagation of ocean waves over long distances. *Deep-Sea Res.* **9**, 185.
- Baer, L., 1963: An experiment in numerical forecasting of deep water ocean waves. Sunnyvale: Lockheed Missile Space Co., LMSC-801296.
- Barber, N. F. and F. Ursell, 1948: The generation and propagation of ocean waves and swell. 1. *Philos. Trans. r. Soc. (A)* **240**, 527.
- Barnett, T. P., 1968: On the generation, dissipation, and prediction of wind waves. *J. geophys. Res.* **73**, 513.
- Barnett, T. P., 1970: Wind waves and swell in the North Sea. *Eos, Wash.* **51**, 544.
- Barnett, T. P. and A. J. Sutherland, 1968: A note on an over-shoot effect in wind-generated waves. *J. geophys. Res.* **73**, 6879.
- Barnett, T. P. and J. C. Wilkerson, 1967: On the generation of ocean wind waves as inferred from airborne radar measurements of fetch-limited spectra. *J. mar. Res.* **25**, 292.
- Becker, G., K. P. Koltermann, G. Prahm und W. Zenk [in prep.]: Die hydrographische Situation in der nördlichen Deutschen Bucht im Juli 1969 (JONSWAP). *Dt. hydrogr. Z.*
- Bretherton, F. P. and C. J. R. Garrett, 1968: Wave trains in inhomogeneous moving media. *Proc. R. Soc. (A)* **302**, 539.
- Bretschneider, C. L. and R. O. Reid, 1954: Changes in wave height due to bottom friction, percolation, and refraction. *Techn. Mem. US Army Eros. Bd.* No 45, 36 pp.
- Brocks, K. and L. Krügermeyer, 1970: The hydrodynamic roughness of the sea surface. *Ber. Inst. Radiomet., Hamburg.* No. 14. (Also in: *Studies in physical oceanography*. Ed. by A. L. Gordon. New York. **1**, 75.)
- Cartwright, D. E., 1971: Tides and waves in the vicinity of Saint Helena. *Philos. Trans. r. Soc. (A)* **270**, 603.
- Cartwright, D. E. and N. D. Smith, 1964: Buoy techniques for obtaining directional wave spectra. *Buoy Technology*. Washington: Marine Technology Society.
- Chernov, L. A., 1960: Wave propagation in a random medium. New York: McGraw-Hill.
- Darbyshire, J., 1963: The one dimensional wave spectrum in the Atlantic Ocean and in coastal waters. In: *Ocean wave spectra*. Prentice Hall. Page 27.
- Davis, R. E., 1969: On the high Reynolds number flow over a wavy boundary. *J. Fluid Mech.* **36**, 337.
- Davis, R. E., 1970: On the turbulent flow over a wavy boundary. *J. Fluid Mech.* **42**, 721.
- DeLeonibus, P. S., 1971: Momentum flux and wave spectra observations from an ocean tower. *J. geophys. Res.* **76**, 6506.
- Dobson, F. W., 1971: Measurements of atmospheric pressure on wind-generated sea waves. *J. Fluid Mech.* **48**, 91.
- Dorrestein, R., 1960: Simplified method of determining refraction coefficients for sea waves. *J. geophys. Res.* **65**, 637.
- Elliott, J., 1972: Microscale pressure fluctuations near waves being generated by the wind. *J. Fluid Mech.* **54**, 427.
- Enke, K., 1973: Turbulenzmessungen über See bei begrenztem Fetch. Diplomarbeit, Inst. Geophys., Univ. Hamburg.
- Ewing, J. A., 1971: A numerical wave prediction method for the North Atlantic Ocean. *Dt. hydrogr. Z.* **24**, 241.
- Hasse, L., 1968: On the determination of the vertical transports of momentum and heat in the atmospheric boundary layer at sea. *Hamburger Geophys. Einzelschr.* Nr. 11. (Also: *Techn. Rep. Dep. Oceanogr., Ore. St. Univ.* No. 188, Ref. No. 70-20. 1970.)
- Hasselmann, D. E., 1971: Wave generation by resonant casemode interactions in a turbulent wind. *Trans. Amer. geophys. Un.* [in prep.].
- Hasselmann, K., 1962: On the non-linear energy transfer in a gravity-wave spectrum. 1: General theory. *J. Fluid Mech.* **12**, 481.
- Hasselmann, K., 1963a: On the non-linear energy transfer in a gravity-wave spectrum. 2: Conservation theorems, wave-particle correspondence, irreversibility. *J. Fluid Mech.* **15**, 273.
- Hasselmann, K., 1963b: On the non-linear energy transfer in a gravity-wave spectrum. 3: Computation of the energy flux and swell-sea interaction for a Neumann spectrum. *J. Fluid Mech.* **15**, 385.
- Hasselmann, K., 1966: Feynman diagrams and interaction rules of wave-wave scattering processes. *Rev. Geophys.* **4**, 1.
- Hasselmann, K., 1967: Nonlinear interactions treated by the methods of theoretical physics (with application to the generation of waves by wind). *Proc. R. Soc. (A)* **299**, 77.
- Hasselmann, K., 1968: Weak-interaction theory of ocean waves. In: *Basic developments in fluid dynamics* (Ed. M. Holt). New York. **2**, 117.
- Hasselmann, K., 1971: On the mass and momentum transfer between short gravity waves and larger-scale motions. *J. Fluid Mech.* **50**, 189.
- Hasselmann, K., 1972: The energy balance of wind waves and the remote sensing problem. *Conf. Sea Surface Topography*, Miami, October, 1971 [in press].
- Hasselmann, K. and J. I. Collins, 1968: Spectral dissipation of finite-depth gravity waves due to turbulent bottom friction. *J. mar. Res.* **26**, 1.
- Iwagaki, Y., Y. Tsuchiya and M. Sakai, 1965: Basic studies on wave damping due to bottom friction. 2: On the measurement of bottom shearing stress. *Bull. Disast. Prev. Res. Inst. Kyoto Univ.* **14**, 45.



- Jeffreys, J., 1924: On the formation of waves by wind. *Proc. R. Soc. (A)* **107**, 189.
- Jonsson, I. G., 1965: Friction factor diagrams for oscillatory boundary layers. *Basic Res. Progr. Rep. coast. Engng Lab. Techn. Univ. Denmark*, No. 10, 10.
- Kajiura, K., 1964: On the bottom friction in an oscillatory current. *Bull. Earthq. Res. Inst.* **42**, 147.
- Kitaigorodskii, S. A., 1962: Applications of the theory of similarity to the analysis of wind-generated wave motion as a stochastic process. *Bull. Acad. Sci. USSR Geophys. Ser.* No. 1, 73.
- Korvin-Kroukovsky, B. V., 1967: Further reflections on properties of sea waves developing along a fetch. *Dt. hydrogr. Z.* **20**, 7.
- Liu, P. C., 1971: Normalized and equilibrium spectra of wind waves in Lake Michigan. *J. phys. Oceanogr.* **1**, 249.
- Long, R., 1971: On generation of ocean waves by a turbulent wind. Ph. D. Thesis, Univ. Miami.
- Long, R., 1972: Scattering of surface waves by bottom irregularities. (subm. to *J. geophys. Res.*)
- Longuet-Higgins, M. S., D. E. Cartwright and N. D. Smith, 1963: Observations of the directional spectrum of sea waves using the motions of a floating buoy. In: *Ocean wave spectra*. Prentice Hall. Page 111.
- Longuet-Higgins, M. S. and R. W. Stewart, 1964: Radiation stress in water waves, a physical discussion with applications. *Deep-Sea Res.* **11**, 529.
- Miles, J. W., 1957: On the generation of surface waves by shear flows. *J. Fluid Mech.* **3**, 185.
- Mitsuyasu, H., 1968a: On the growth of the spectrum of wind-generated waves. 1. *Rep. Res. Inst. Appl. Mech., Kyushu Univ.* **16**, 459.
- Mitsuyasu, H., 1968b: A note on the non-linear energy transfer in the spectrum of wind-generated waves. *Rep. Res. Inst. Appl. Mech., Kyushu Univ.* **16**, 251.
- Mitsuyasu, H., 1969: On the growth of the spectrum of wind-generated waves. 2. *Rep. Res. Inst. Appl. Mech., Kyushu Univ.* **17**, 235.
- Mitsuyasu, H., R. Nakayama and T. Komori, 1971: Observations of the wind and waves in Hakata Bay. *Rep. Res. Inst. Appl. Mech., Kyushu Univ.* **19**, 37.
- Munk, W. H., G. R. Miller, F. E. Snodgrass and N. F. Barber, 1963: Directional recording of swell from distant storms. *Philos. Trans. r. Soc. (A)* **255**, 505.
- Munk, W. H. and F. E. Snodgrass, 1957: Measurements of southern swell at Guadalupe Island. *Deep-Sea Res.* **4**, 272.
- Phillips, O. M., 1958: The equilibrium range in the spectrum of wind-generated ocean waves. *J. Fluid Mech.* **4**, 426.
- Phillips, O. M., 1963: On the attenuation of long gravity waves by short breaking waves. *J. Fluid Mech.* **16**, 321.
- Phillips, O. M., 1966: *The dynamics of the upper ocean*. Cambridge: University Press.
- Pierson, W. J., Jr. and L. Moskowitz, 1964: A proposed spectral form for fully developed wind seas based on the similarity theory of S. A. Kitaigorodskii. *J. geophys. Res.* **69**, 5181.
- Pierson, W. J., Jr. and R. A. Stacy, 1973: On the elevation, slope and curvature spectra of a wind roughened sea [in press].
- Pierson, W. J., Jr., L. J. Tick and L. Baer, 1966: Computer based procedure for preparing global wave forecasts and wind field analysis capable of using wave data obtained by a space craft. 6th Symp. Naval Hydrogr., Washington, Office of Naval Research.
- Pond, S., G. T. Phelps, J. E. Paquin, G. McBean and R. W. Stewart, 1971: Measurements of the turbulent fluxes of momentum, moisture, and sensible heat over the ocean. *J. atmos. Sci.* **28**, 901.
- Putnam, J. A. and J. W. Johnson, 1949: The dissipation of wave energy by bottom friction. *Trans. Amer. geophys. Un.* **30**, 67.
- Ross, D. B., V. J. Cardone and J. W. Conaway, 1970: Laser and micro-wave observations of sea-surface conditions for fetch-limited 17- to 25-m/s winds. *IEEE Trans., Geosci. Electronics GE-8*, 326.
- Savage, R. P., 1953: Laboratory study of wave energy by bottom friction and percolation. *Techn. Mem. U.S. Army Eros. Bd.*, No. 31, 25 pp.
- Schule, J. J., L. S. Simpson and P. S. DeLeonibus, 1971: A study of fetch-limited wave spectra with an airborne laser. *J. geophys. Res.* **76**, 4160.
- Sell, W. and K. Hasselmann, 1972: Computations of nonlinear energy transfer for JONSWAP and empirical wind wave spectra. [Rep.] *Inst. Geophys., Univ. Hamburg*.
- Smith, S. D., 1967: Thrust-anemometer measurement of wind-velocity spectra and of Reynolds stress over a coastal inlet. *J. mar. Res.* **25**, 239.
- Smith, S. D., 1970: Thrust-anemometer measurements of wind turbulence, Reynolds stress and drag coefficient over sea. *J. geophys. Res.* **75**, 6758.
- Snodgrass, F. E., G. W. Groves, K. F. Hasselmann, G. R. Miller, W. H. Munk and W. H. Powers, 1966: Propagation of ocean swell across the Pacific. *Philos. Trans. r. Soc. (A)* **259**, 431.
- Snyder, R. L. and C. S. Cox, 1966: A field study of the wind generation of ocean waves. *J. mar. Res.* **24**, 141.
- Sutherland, A. J., 1968: Growth of spectral components in a wind-generated wave train. *J. Fluid Mech.* **33**, 545.
- Tatarski, V. I., 1961: *Wave propagation in a turbulent medium*. New York: McGraw-Hill.
- Walden, H. und H. J. Rubach, 1967: Gleichzeitige Messungen des Seegangs mit nicht-stabilisierten Beschleunigungsschreibern an Orten mit unterschiedlicher Wassertiefe in der Deutschen Bucht. *Dt. hydrogr. Z.* **20**, 157.
- Whitham, G. B., 1967: Variational methods and applications to water waves. *Proc. R. Soc. (A)* **299**, 6.